

# **Nanoparticle impact on membrane properties and embedded ion channels**

By

Isabel Ursula Foreman-Ortiz

A dissertation submitted in partial fulfillment of the requirements for the degree of Doctor of Philosophy (Chemistry) at the University of Wisconsin – Madison

2021

Date of Final Oral Examination: 05/10/2021

The dissertation is approved of by the following members of the Final Oral Committee:

Dr. Joel A. Pedersen, Professor, Soil Science (University of Wisconsin – Madison)

Dr. Robert J. Hamers, Professor, Chemistry (University of Wisconsin – Madison)

Dr. Silvia Cavagnero, Professor, Chemistry (University of Wisconsin – Madison)

Dr. Qiang Cui, Professor, Chemistry (Boston University)

# Nanoparticle impact on membrane properties and embedded ion channels

Isabel Ursula Foreman-Ortiz

Under the Supervision of Professor Joel A. Pedersen

University of Wisconsin – Madison

## **Abstract**

Nanomaterials used in consumer and industrial products are subject to release into the environment. As these nanomaterials enter the environment, they are likely to come into contact with cell surfaces, which consist primarily of a lipid bilayer and many surface and embedded membrane proteins. Thus, it is important to study the impact of nanomaterials on lipid bilayer systems containing membrane proteins as these interactions may play a critical role in cellular function and response. The studies presented here work to understand nanomaterial binding to and functional disruption of model membranes containing the membrane protein and ion channel, gramicidin A (gA), as well as changes in membrane mechanical properties which may alter the function of gA. The transient dimerization of small gA molecules to form a current-passing channel facilitates its use as a functional model ion channel. Moreover, its channel length is smaller than that of the lipid bilayer, making its dimerization sensitive to changes in bilayer mechanical properties which alter the tension placed on channel dimers. Utilizing this model system, variation of nanomaterial and membrane properties ultimately allows for a detailed study on nanomaterial binding and disruption of ion channel function.

The first set of studies sought to investigate the impact of anionic nanoparticles on gA function in suspended lipid bilayers. Voltage clamp electrophysiology measurements on ion channel formation indicated that anionic nanoparticles increased gA channel duration, suggesting

that ion channel function was altered through changes in membrane mechanical properties which alter membrane tension on channels and ultimately dictate channel lifetime. This change in function was observed for two anionic nanoparticle types of varying size and aggregation states. Molecular dynamics simulations were employed to further analyze the role of membrane mechanical properties in altering gA function. Nanoparticles were found not to interact with ion channels directly. Instead, transient interactions between nanoparticles and the lipid bilayer resulted in increased packing of lipids near the nanoparticle-bound area, leading to local softening in extended areas due to weakening of adhesion between neighboring lipids. These results demonstrate that anionic nanoparticle-induced alterations in gA function may be mediated by membrane mechanical properties.

Subsequent studies were performed to determine how the presence of gA alters the binding of anionic nanoparticles. These studies employed a unique combination of nanoparticle tracking analysis (NTA) and statistical mixture distributions to determine the percent of nanoparticle binding in varying ratios to vesicles containing versus lacking gA. Application of statistical mixture distributions involved drawing from measured NTA diffusion coefficients of individual mixture components (nanoparticles and vesicles) and iteratively binding particles until the distribution of diffusion coefficients closely matched that measured for the mixture. Two diffusional models were applied (Stokes-Einstein and Kirkwood-Riseman) to convert particle diffusion coefficients to particle hydrodynamic diameters. Both models predicted that the presence of gA increases the binding of anionic nanoparticles in both attached (1:1 nanoparticle:vesicle) and bridged (1:2 nanoparticle:vesicle) motifs. The Kirkwood-Riseman model was ultimately determined to be the best fitting model via statistical testing, indicating the importance of model choice. These results demonstrate the application of a new combination of

methods (NTA and statistical mixture distributions) to obtain an accurate measure of particle binding and determined that the presence of gA increases the interaction of vesicles with anionic nanoparticles.

Finally, the influence of anionic nanoparticles on membrane mechanical properties were measured using a membrane-segregating dye which is sensitive to changes in membrane packing (Laurdan). It was determined that anionic nanoparticles can increase lipid packing in a phospholipid vesicle system, although the extent of that effect is determined by lipid type, salt concentration, and anionic nanoparticle ligand structure. These results suggest that there is an electrostatic interaction between nanoparticle and lipid vesicle, and that the lipid packing itself dictates the degree of nanoparticle impact. Although this system lacks gA, these results are consistent with those previously obtained using gA ion channels in suspended membranes – anionic nanoparticles exert an effect on membrane mechanical properties which may then result in observable changes to gA ion channel function.

## Acknowledgements

*“We have to continually be jumping off cliffs and developing our wings on the way down.”*

– Kurt Vonnegut

The best part of my PhD has been the lifelong connections, friendship, and mentorship I’ve received along the way. First, I would like to thank my advisor and mentor, Joel Pedersen, for always fostering my creative development as a scientist. You gave me the creative freedom to explore my own ideas while also providing meticulous and thoughtful critiques that molded me into a writer and scientist that I can be proud of. To my committee and the Center for Sustainable Nanotechnology professors who provided wisdom throughout the process – thank you for all the advice and critique that ultimately shaped my thesis.

I would also like to thank the countless graduate students that I have been privileged to meet. Thank you to my fellow Pedersen lab members who served as a constant support and source of intellectual daydreaming throughout the years. To Kyoungtea Kim, thank you for listening to my endless banter and being a supportive enemy when I most needed it. To Nasim Ganji, it was a privilege being your desk neighbor and conversing with you daily. A special highlight of my time in the Pedersen lab was our conference trip to South Korea where I acquired many cherished memories with labmates Kyoungtea Kim, Davied Nielsen-Franco, and Christian Lochbaum. Additionally, thank you to fellow Center for Sustainable Nanotechnology graduate students Arielle Mensch and Liz Laudadio for friendship and endless comedic relief. For Kelly Zhang, our bubble tea outings, movie nights, and whirlwind friendship are some of my favorite memories ever.

I was lucky to have mentored some of the best undergraduates in the world. To Yuanya Zhao, Brenda Gonzales, Christian Freeman, and Jorge Calderin – it was truly a privilege to work with each of you. I am excited to see where your curiosity, drive, and enthusiasm takes you. Thank you for letting me be a part of your growth. To Mike Schwartz – your persistent encouragement pulled me through difficult times. Thank you for your perspective and wisdom.

I would also like to recognize the support of my family. To my parents Carol Foreman and Pedro Ortiz, thank you for a lifetime of noticing and fostering my strengths. To my older sister Eva Foreman-Ortiz, the support of a sister outweighs everything else. Thank you for the conversation, understanding, and love. For my partner Niko – thank you for nearly 3 years of unending company, comedy, and a shoulder to cry on. Each of you were absolutely critical to my success.

Lastly, I would like to thank Flatbread (my cat) for his service as the world’s best companion and source of laughter.

## Table of Contents

<b>Abstract</b> .....	<b>i</b>
<b>Table of Contents</b> .....	<b>v</b>
<b>Chapter 1: Background and Introduction</b> .....	<b>1</b>
1.1 Engineered nanomaterials in the environment .....	1
1.2 Impact of nanomaterials on cellular outcomes .....	1
1.3 Impact of nanomaterials on ion channels—binding and function .....	3
1.4 Nanoparticle impact on membrane mechanical properties.....	3
1.5 Scope of Thesis.....	4
1.6 References.....	6
<b>Chapter 2: Anionic nanoparticle-induced perturbation to phospholipid membranes affects ion channel function</b> .....	<b>10</b>
2.1 Introduction.....	10
2.2 Materials and Methods.....	13
2.2.1 Ligand and gold nanoparticle synthesis .....	13
2.2.2 Characterization of gold nanoparticles.....	15
2.2.3 Nanoparticle ligand density by X-Ray Photoelectron Spectroscopy (XPS) .....	15
2.2.4 Preparation of planar suspended lipid bilayers and Voltage-Clamp electrophysiology .....	16
2.2.5 Preparation and characterization of small unilamellar vesicles (SUVs) .....	19
2.2.6 Attenuated Total Reflectance–Fourier Transform Infrared (ATR-FTIR) Spectroscopy .....	20
2.2.7 Molecular Dynamics (MD) Simulations.....	21
2.3 Results and Discussion .....	23
2.3.1 Anionic AuNPs Impact Ion Channel Function .....	23
2.3.2 Anionic AuNPs Do Not Impact gA Conformation .....	25
2.3.3 MPA-AuNPs Perturb Local Membrane Properties.....	26
2.4 Conclusions and Implications .....	28
2.5 Tables and Figures .....	34
2.6 References.....	46
<b>Chapter 3: Nanoparticle tracking analysis and statistical mixture distribution analysis to quantify nanoparticle–vesicle binding</b> .....	<b>56</b>
3.1 Introduction.....	56
3.2. Materials and methods .....	58
3.2.1 Synthesis of gold nanoparticles capped with 3-mercaptopropionic acid (MPA).....	58
3.2.2. Ultraviolet-visible absorbance spectroscopy.....	58

3.2.3. Transmission electron microscopy (TEM).....	58
3.2.4. Formation and characterization of SUVs.....	58
3.2.5 Fluorescence spectroscopy.....	59
3.2.6. Nanoparticle tracking analysis .....	59
3.2.7. Dynamic light scattering .....	60
3.2.8. Laser Doppler electrophoresis .....	62
3.2.9. Statistical analysis of mixture distributions .....	62
3.3 Results and discussion .....	65
3.3.1. Assessment of nanoparticle binding to vesicles by DLS .....	65
3.3.2. Determination of fraction of AuNPs bound from mixture distributions and NTA.....	66
3.3.3. Stokes–Einstein model.....	67
3.3.4. Kirkwood–Riseman model .....	68
3.4. Conclusion .....	70
3.5 Tables and Figures .....	72
3.6 References.....	78
<b>Chapter 4: Anionic nanoparticles impact lipid packing in vesicles.....</b>	<b>82</b>
4.1 Introduction.....	82
4.2 Materials and Methods.....	85
4.2.1 Materials .....	85
4.2.2 Ligand and gold nanoparticle synthesis .....	86
4.2.3 Characterization of gold nanoparticles.....	87
4.2.4 Preparation and characterization of small unilamellar vesicles .....	87
4.2.5 Laurdan fluorescence generalized polarization (GP) measurements .....	88
4.3 Results and Discussion .....	89
4.3.1 Cholesterol content or Anionic MPA-AuNP Exposure Impact Lipid Packing.....	89
4.3.2 Less rigid vesicles are affected more by NP-induced lipid packing changes .....	90
4.3.3 Aggregation state influences MPA-AuNP impact on lipid membranes .....	91
4.3.4 Anionic NP-induced packing changes may be particle-dependent.....	92
4.4 Conclusions and implications .....	93
4.5 Tables and Figures .....	94
4.6 References.....	102
<b>Chapter 5: Conclusions and Future Directions.....</b>	<b>106</b>

## Chapter 1: Background and Introduction

### 1.1 Engineered nanomaterials in the environment

Nanomaterials, defined as materials having at least one dimension between 1 and 100 nm, have a number of interesting characteristics that make them technologically desirable. These include increased reactivity relative to bulk materials resulting from a high surface area to volume ratio, small size allowing potential cellular interaction and uptake, and interesting photonic properties exploited in displays and imaging.<sup>1,2</sup> Between 2010 and 2019 alone, there was a 24% increase in consumer products reporting the inclusion of nanomaterials, in commercial areas such as cosmetics, sporting goods, clothing, foods, and pharmaceuticals.<sup>3,4</sup> The rise of engineered nanomaterials, designed and used for a specific purpose, leads to increased environmental release and the potential to interact with the cells of organisms found in the environment.<sup>5</sup> Thus it is important to understand how nanomaterials interact with organisms and their cells in the environment in order to prevent negative effects that may ultimately impact the ecosystem.<sup>5</sup> Moreover, biomedical, pharmaceutical, and agricultural applications of nanomaterials necessitate the understanding of nano-bio interactions for safe and intended use.<sup>6</sup>

### 1.2 Impact of nanomaterials on cellular outcomes

Studies on nanomaterial impact on cells show that nanomaterial surface chemistries play a large role in responses such as binding to cells<sup>7-11</sup>, membrane disruption and defect formation<sup>8,11-15</sup>, lipid peroxidation<sup>14,16</sup>, modulation of membrane potential<sup>17,18</sup>, cellular uptake<sup>18,19</sup>, as well as toxicity and cell death<sup>7,8,11,12,14,15</sup>. Cationic nanoparticles have been found to be more cytotoxic than anionic nanoparticles<sup>7,8,12</sup>, although both anionic nanoparticles and sublethal doses of cationic nanoparticles still demonstrate adverse cellular effects including cell

membrane damage and alterations in membrane potential.<sup>13,17,18</sup> Other features of nanomaterials, including the production of reactive oxygen species (ROS)<sup>14,16</sup> and degree of ligand hydrophobicity<sup>12</sup>, dictate cellular response. Nanoparticles capable of inducing ROS production, including TiO<sub>2</sub>, ZnO, and silver, are more likely to cause lipid peroxidation<sup>14,16,20</sup> that can ultimately lead to potential negative cellular outcomes including increased membrane permeability and alterations in gene expression and cell metabolism.<sup>21</sup> Studies on cells also show that hydrophobic ligands may regulate nanoparticle translocation across the membrane due to the affinity of hydrophobic nanomaterials for the membrane interior.<sup>22-24</sup>

In addition to the effects of surface chemistry, nanoparticle size, shape, or aggregation influence the rate and mode of cellular uptake (passive diffusion, phagocytosis, etc.)<sup>25-28</sup> – small nanoparticles are typically found to internalize faster.<sup>25</sup> However, there is a complex interplay between nanoparticle size and surface chemistry, and studies demonstrate that an increase in nanoparticle size does not universally indicate a decrease in amount or rate of cellular uptake.<sup>25,27</sup> While increasing size of zwitterionic and anionic gold nanoparticles was found to decrease uptake, larger cationic nanoparticles demonstrated increased uptake in human cervical carcinoma (HeLa) cells.<sup>27</sup> The variation in uptake of NPs is likely due to differences in cellular uptake mechanisms – which is altered by both size and surface charge of NPs.<sup>27</sup> There is also variability in size-dependent uptake of anionic nanoparticles across multiple cell lines, indicating the importance of cell surface features in uptake.<sup>25</sup>

Nanomaterial impact on cells is thus also dictated by cell surface chemistry. Cell membranes have a variety of species in the distal leaflet that are subject to potential nanomaterial interactions. Some bacteria bear lipopolysaccharide (LPS) molecules of varying length and terminal chemical identity on the outer leaflet of the outer membrane—higher densities<sup>10</sup> and

longer LPS moieties<sup>9</sup> were associated with increased binding of cationic nanoparticles via electrostatic attraction. However, the cell membrane also contains many embedded membrane proteins, which make up about 50% by mass of the cell membrane.<sup>29</sup> Thus, the impact of nanomaterials on membrane proteins is of considerable interest.

### **1.3 Impact of nanomaterials on ion channels—binding and function**

Considerable focus has been placed on understanding the generation of soluble, cytoplasmic protein layers on nanoparticle surfaces, as this protein ‘corona’ may play a role in subsequent interactions with cell surfaces or organelles.<sup>30–35</sup> However, fewer studies have been dedicated towards the interaction of nanomaterials with membrane-embedded proteins. Ion channels are one such class of membrane protein which may be of interest in nanomaterial interactions due to their role in maintaining cellular homeostasis and function via control of membrane potential, transport, nerve impulse conduction, and muscle contraction.<sup>36</sup> Ion channels are transmembrane proteins which ‘gate’, or open and close, in response to external stimuli (e.g., exposure to certain ligands, membrane properties like stiffness or potential) to allow passage of ions. Numerous cellular studies show that nanoparticles can impact ion channel function, as reflected in changes in membrane potential<sup>17,37</sup>, alterations in ion channel gating<sup>38</sup>, or decreases in ion channel function.<sup>39–43</sup> Nanoparticle-induced alterations in ion channel function can lead to impacts on cell function including changes in excitability of neurons.<sup>44</sup>

### **1.4 Nanoparticle impact on membrane mechanical properties**

The mechanism through which nanomaterials can alter ion channel function is often attributed to direct ion channel blockage or binding to extracellular domains which result in protein conformational changes.<sup>39,41–43</sup> However, a number of studies have also proposed, but not

demonstrated, that nanoparticles may indirectly alter ion channel function through changes in membrane mechanical properties.<sup>37,38,40</sup> Ion channel function can be modulated by membrane properties like thickness, stiffness, or curvature, as the channel deformation during the gating process depends on hydrophobic matching with the surrounding lipid bilayer.<sup>45</sup> Charged nanomaterials have been demonstrated to impact lipid packing<sup>46</sup>, suggesting potential to impact membrane properties and ultimately, the function of embedded membrane proteins.

## **1.5 Scope of Thesis**

Nanomaterials released into the environment will inevitably encounter cells and organisms, where a likely first point of contact is the cell membrane. Moreover, use of nanomaterials in biomedical or pharmaceutical applications necessitates an understanding of their interactions with the cell membrane. Model membrane systems composed primarily of lipids have long been used to capture mechanistic insight into nanoparticle-membrane interactions which would otherwise be difficult to capture in cells or organisms. However, such simplistic model systems do not capture functional changes in proteins or other embedded species which may ultimately contribute to cellular outcomes. The scope of this thesis is focused on building up membrane complexity to a combination of lipids and embedded ion channels to study the impact of nanomaterial exposure on binding and membrane mechanical properties and subsequent changes in ion channel function.

Chapter two begins by demonstrating that anionic nanoparticles impact the function of gramicidin A (gA) ion channels embedded in a model lipid membrane. We used computational studies to suggest that this functional change may be due to nanoparticle-lipid membrane binding that alters membrane packing and compressibility, leading to the observed decrease in function

of embedded ion channels. These studies are among the first to demonstrate functional protein changes as a result of nanomaterial-membrane interactions.

Chapter three then uses a novel combination of nanoparticle tracking analysis (NTA) and statistical mixture distributions to quantify binding to model membranes that either contain or lack embedded gA ion channels. These studies demonstrated that anionic nanoparticles bind more frequently and in greater number to membranes containing ion channel than those lacking them. Moreover, a novel statistical analysis is presented and proposed as useful in quantitative assessment of binding in other nano-sized systems.

Chapter four further and more explicitly examines the impact of anionic nanoparticles on membrane properties by utilizing a phase-segregating dye to qualitatively assess lipid packing. One anionic nanomaterial was found to increase lipid packing in systems of varying salt concentration or lipid vesicle rigidity. However, the effect may vary based on anionic ligand type, which modulates the extent of negative charge. These studies provide experimental confirmation for the membrane-mediated mechanism of ion channel functional changes suggested in Chapter two.

Finally, Chapter five presents a larger summary and ties between each Chapter, context within the larger field, and potential future directions motivated by the findings of these studies.

## 1.6 References

- (1) Murphy, C. J.; Sau, T. K.; Gole, A. M.; Orendorff, C. J.; Gao, J.; Gou, L.; Hunyadi, S. E.; Li, T. Anisotropic Metal Nanoparticles: Synthesis, Assembly, and Optical Applications. *J. Phys. Chem. B* **2005**, *109* (29), 13857–13870. <https://doi.org/10.1021/jp0516846>.
- (2) Bera, D.; Qian, L.; Tseng, T. K.; Holloway, P. H. Quantum Dots and Their Multimodal Applications: A Review. *Materials (Basel)*. **2010**, *3* (4), 2260–2345. <https://doi.org/10.3390/ma3042260>.
- (3) Vance, M. E.; Kuiken, T.; Vejerano, E. P.; McGinnis, S. P.; Hochella, M. F.; Hull, D. R. Nanotechnology in the Real World: Redeveloping the Nanomaterial Consumer Products Inventory. *Beilstein J. Nanotechnol.* **2015**, *6* (1), 1769–1780. <https://doi.org/10.3762/bjnano.6.181>.
- (4) Contado, C. Nanomaterials in Consumer Products: A Challenging Analytical Problem. *Front. Chem.* **2015**, *3* (AUG), 1–20. <https://doi.org/10.3389/fchem.2015.00048>.
- (5) Maurer-Jones, M. A.; Gunsolus, I. L.; Murphy, C. J.; Haynes, C. L. Toxicity of Engineered Nanoparticles in the Environment. *Anal. Chem.* **2013**, *85* (6), 3036–3049. <https://doi.org/10.1021/ac303636s>.
- (6) Cheng, L.-C.; Jiang, X.; Wang, J.; Chen, C.; Liu, R.-S. Nano-Bio Effects: Interaction of Nanomaterials with Cells. *Nanoscale* **2013**, *5* (9), 3547–3569. <https://doi.org/10.1039/c3nr34276j>.
- (7) Feng, Z. V.; Gunsolus, I. L.; Qiu, T. A.; Hurley, K. R.; Nyberg, L. H.; Frew, H.; Johnson, K. P.; Vartanian, A. M.; Jacob, L. M.; Lohse, S. E.; Torelli, M. D.; Hamers, R. J.; Murphy, C. J.; Haynes, C. L. Impacts of Gold Nanoparticle Charge and Ligand Type on Surface Binding and Toxicity to Gram-Negative and Gram-Positive Bacteria. *Chem. Sci.* **2015**, *6* (9), 5186–5196. <https://doi.org/10.1039/c5sc00792e>.
- (8) Goodman, C. M.; McCusker, C. D.; Yilmaz, T.; Rotello, V. M. Toxicity of Gold Nanoparticles Functionalized with Cationic and Anionic Side Chains. *Bioconjug. Chem.* **2004**, *15* (4), 897–900. <https://doi.org/10.1021/bc049951i>.
- (9) Buchman, J. T.; Rahnamoun, A.; Landy, K. M.; Zhang, X.; Vartanian, A. M.; Jacob, L. M.; Murphy, C. J.; Hernandez, R.; Haynes, C. L. Using an Environmentally-Relevant Panel of Gram-Negative Bacteria to Assess the Toxicity of Polyallylamine Hydrochloride-Wrapped Gold Nanoparticles. *Environ. Sci. Nano* **2018**, *5* (2), 279–288. <https://doi.org/10.1039/c7en00832e>.
- (10) Jacobson, K. H.; Gunsolus, I. L.; Kuech, T. R.; Troiano, J. M.; Melby, E. S.; Lohse, S. E.; Hu, D.; Chrisler, W. B.; Murphy, C. J.; Orr, G.; Geiger, F. M.; Haynes, C. L.; Pedersen, J. A. Lipopolysaccharide Density and Structure Govern the Extent and Distance of Nanoparticle Interaction with Actual and Model Bacterial Outer Membranes. *Environ. Sci. Technol.* **2015**, *49* (17), 10642–10650. <https://doi.org/10.1021/acs.est.5b01841>.
- (11) Williams, D. N.; Pramanik, S.; Brown, R. P.; Zhi, B.; McIntire, E.; Hudson-Smith, N. V.; Haynes, C. L.; Rosenzweig, Z. Adverse Interactions of Luminescent Semiconductor Quantum Dots with Liposomes and *Shewanella Oneidensis*. *ACS Appl. Nano Mater.* **2018**, *1* (9), 4788–4800. <https://doi.org/10.1021/acsanm.8b01000>.

- (12) Fröhlich, E. The Role of Surface Charge in Cellular Uptake and Cytotoxicity of Medical Nanoparticles. *Int. J. Nanomedicine* **2012**, *7*, 5577–5591. <https://doi.org/10.2147/IJN.S36111>.
- (13) Chen, J.; Hessler, J. A.; Putchakayala, K.; Panama, B. K.; Khan, D. P.; Hong, S.; Mullen, D. G.; DiMaggio, S. C.; Som, A.; Tew, G. N.; Lopatin, A. N.; Baker, J. R.; Holl, M. M. B.; Orr, B. G. Cationic Nanoparticles Induce Nanoscale Disruption in Living Cell Plasma Membranes. *J. Phys. Chem. B* **2009**, *113* (32), 11179–11185. <https://doi.org/10.1021/jp9033936>.
- (14) Zhornik, E. V.; Baranova, L. A.; Drozd, E. S.; Sudas, M. S.; Chau, N. H.; Buu, N. Q.; Dung, T. T. N.; Chizhik, S. A.; Volotovskii, I. D. Silver Nanoparticles Induce Lipid Peroxidation and Morphological Changes in Human Lymphocytes Surface. *Biophys. (Russian Fed.)* **2014**, *59* (3), 380–386. <https://doi.org/10.1134/S0006350914030282>.
- (15) Nazemidashtarjandi, S.; Farnoud, A. M. Membrane Outer Leaflet Is the Primary Regulator of Membrane Damage Induced by Silica Nanoparticles in Vesicles and Erythrocytes. *Environ. Sci. Nano* **2019**, *6* (4), 1219–1232. <https://doi.org/10.1039/c8en01267a>.
- (16) Dutta, R. K.; Nenavathu, B. P.; Gangishetty, M. K.; Reddy, A. V. R. Studies on Antibacterial Activity of ZnO Nanoparticles by ROS Induced Lipid Peroxidation. *Colloids Surfaces B Biointerfaces* **2012**, *94*, 143–150. <https://doi.org/10.1016/j.colsurfb.2012.01.046>.
- (17) Warren, E. A. K.; Payne, C. K. Cellular Binding of Nanoparticles Disrupts the Membrane Potential. *RSC Adv.* **2015**, *5* (18), 13660–13666. <https://doi.org/10.1039/c4ra15727c>.
- (18) Arvizo, R. R.; Miranda, O. R.; Thompson, M. A.; Pabelick, C. M.; Bhattacharya, R.; David Robertson, J.; Rotello, V. M.; Prakash, Y. S.; Mukherjee, P. Effect of Nanoparticle Surface Charge at the Plasma Membrane and Beyond. *Nano Lett.* **2010**, *10* (7), 2543–2548. <https://doi.org/10.1021/nl101140t>.
- (19) Orr, G.; Panther, D. J.; Cassens, K. J.; Phillips, J. L.; Tarasevich, B. J.; Pounds, J. G. Syndecan-1 Mediates the Coupling of Positively Charged Submicrometer Amorphous Silica Particles with Actin Filaments across the Alveolar Epithelial Cell Membrane. *Toxicol. Appl. Pharmacol.* **2009**. <https://doi.org/10.1016/j.taap.2009.01.022>.
- (20) Runa, S.; Lakadamyali, M.; Kemp, M. L.; Payne, C. K. TiO<sub>2</sub> Nanoparticle-Induced Oxidation of the Plasma Membrane: Importance of the Protein Corona. *J. Phys. Chem. B* **2017**, *121* (37), 8619–8625. <https://doi.org/10.1021/acs.jpcc.7b04208>.
- (21) Niki, E.; Yoshida, Y.; Saito, Y.; Noguchi, N. Lipid Peroxidation: Mechanisms, Inhibition, and Biological Effects. *Biochem. Biophys. Res. Commun.* **2005**, *338* (1), 668–676. <https://doi.org/10.1016/j.bbrc.2005.08.072>.
- (22) Hu, G.; Jiao, B.; Shi, X.; Valle, R. P.; Fan, Q.; Zuo, Y. Y. Physicochemical Properties of Nanoparticles Regulate Translocation across Pulmonary Surfactant Monolayer and Formation of Lipoprotein Corona. *ACS Nano* **2013**, *7* (12), 10525–10533. <https://doi.org/10.1021/nn4054683>.
- (23) Sachan, A. K.; Harishchandra, R. K.; Bantz, C.; Maskos, M.; Reichelt, R.; Galla, H. J. High-Resolution Investigation of Nanoparticle Interaction with a Model Pulmonary Surfactant Monolayer. *ACS Nano* **2012**, *6* (2), 1677–1687. <https://doi.org/10.1021/nn204657n>.
- (24) Gao, J.; Zhang, O.; Ren, J.; Wu, C.; Zhao, Y. Aromaticity/Bulkiness of Surface Ligands to Promote the Interaction of Anionic Amphiphilic Gold Nanoparticles with Lipid Bilayers.

*Langmuir* **2016**, *32* (6), 1601–1610. <https://doi.org/10.1021/acs.langmuir.6b00035>.

(25) Dos Santos, T.; Varela, J.; Lynch, I.; Salvati, A.; Dawson, K. A. Quantitative Assessment of the Comparative Nanoparticle-Uptake Efficiency of a Range of Cell Lines. *Small* **2011**, *7* (23), 3341–3349. <https://doi.org/10.1002/sml.201101076>.

(26) Jiang, W.; Kim, B. Y. S.; Rutka, J. T.; Chan, W. C. W. Nanoparticle-Mediated Cellular Response Is Size-Dependent. *Nat. Nanotechnol.* **2008**, *3* (3), 145–150. <https://doi.org/10.1038/nnano.2008.30>.

(27) Jiang, Y.; Huo, S.; Mizuhara, T.; Das, R.; Lee, Y.; Hou, S.; Moyano, D. F.; Duncan, B.; Liang, X.; Rotello, V. M. The Interplay of Size and Surface Functionality on the Cellular Uptake. *ACS Nano* **2015**, *9* (10), 9986–9993. <https://doi.org/10.1021/acsnano.5b03521>.

(28) Kinnear, C.; Moore, T. L.; Rodriguez-Lorenzo, L.; Rothen-Rutishauser, B.; Petri-Fink, A. Form Follows Function: Nanoparticle Shape and Its Implications for Nanomedicine. *Chem. Rev.* **2017**, *117* (17), 11476–11521. <https://doi.org/10.1021/acs.chemrev.7b00194>.

(29) Alberts, B.; Johnson, A.; Lewis, J.; Raff, M.; Roberts, K.; Walter, P. *Molecular Biology of the Cell, Fourth Edition*; 2002. <https://doi.org/citeulike-article-id:691434>.

(30) Pino, P. del; Pelaz, B.; Zhang, Q.; Maffre, P.; Nienhaus, G. U.; Parak, W. J. Protein Corona Formation around Nanoparticles – from the Past to the Future. *Mater. Horiz.* **2014**, *1* (3), 301–313. <https://doi.org/10.1039/C3MH00106G>.

(31) Kelly, P. M.; Åberg, C.; Polo, E.; Connell, A. O.; Cookman, J.; Fallon, J.; Krpeti, Ž.; Dawson, K. A. Mapping Protein Binding Sites on the Biomolecular Corona of Nanoparticles. *Nat. Nanotechnol.* **2015**, *10* (5), 472–479. <https://doi.org/10.1038/nnano.2015.47>.

(32) Vilanova, O.; Mittag, J. J.; Kelly, P. M.; Milani, S.; Dawson, K. A.; Ra, J. O. Understanding the Kinetics of Protein – Nanoparticle Corona Formation. **2016**. <https://doi.org/10.1021/acsnano.6b04858>.

(33) Casals, E.; Pfaller, T.; Duschl, A.; Oostingh, G. J.; Puntès, V. Time Evolution of the Nanoparticle Protein Corona. *ACS Nano* **2010**, *4* (7), 3623–3632. <https://doi.org/10.1021/nn901372t>.

(34) Huang, R.; Lau, B. L. T. Biomolecule-Nanoparticle Interactions: Elucidation of the Thermodynamics by Isothermal Titration Calorimetry. *Biochim. Biophys. Acta - Gen. Subj.* **2016**, *1860* (5), 945–956. <https://doi.org/10.1016/j.bbagen.2016.01.027>.

(35) Bertrand, N.; Grenier, P.; Mahmoudi, M.; Lima, E. M.; Appel, E. A.; Dormont, F.; Lim, J. M.; Karnik, R.; Langer, R.; Farokhzad, O. C. Mechanistic Understanding of in Vivo Protein Corona Formation on Polymeric Nanoparticles and Impact on Pharmacokinetics. *Nat. Commun.* **2017**, *8* (1). <https://doi.org/10.1038/s41467-017-00600-w>.

(36) Gadsby, D. C. Ion Channels versus Ion Pumps: The Principal Difference, in Principle. *Nat. Rev. Mol. Cell Biol.* **2009**, *10* (5), 344–352. <https://doi.org/10.1038/nrm2668>.

(37) Busse, M.; Kraegeloh, A.; Stevens, D.; Cavelius, C.; Rettig, J.; Arzt, E.; Strauss, D. J. Modeling the Effects of Nanoparticles on Neuronal Cells: From Ionic Channels to Network Dynamics. *2010 Annu. Int. Conf. IEEE Eng. Med. Biol. Soc. EMBC'10* **2010**, 3816–3819.

<https://doi.org/10.1109/IEMBS.2010.5627595>.

(38) Piscopo, S.; Brown, E. R. Zinc Oxide Nanoparticles and Voltage-Gated Human Kv11.1 Potassium Channels Interact through a Novel Mechanism. *Small* **2018**, *14* (15), 1–11.

<https://doi.org/10.1002/sml.201703403>.

(39) Leifert, A.; Pan, Y.; Kinkeldey, A.; Schiefer, F.; Setzler, J.; Scheel, O.; Lichtenbeld, H.; Schmid, G.; Wenzel, W.; Jahnen-Dechent, W.; Simon, U. Differential HERG Ion Channel Activity of Ultrasmall Gold Nanoparticles. *Proc. Natl. Acad. Sci. U. S. A.* **2013**, *110* (20), 8004–8009. <https://doi.org/10.1073/pnas.1220143110>.

(40) Monticelli, L.; Barnoud, J.; Orłowski, A.; Vattulainen, I. Interaction of C 70 Fullerene with the Kv1.2 Potassium Channel. *Phys. Chem. Chem. Phys.* **2012**, *14* (36), 12526–12533.

<https://doi.org/10.1039/c2cp41117b>.

(41) Calvaresi, M.; Furini, S.; Domene, C.; Bottoni, A.; Zerbetto, F. Blocking the Passage: C60 Geometrically Clogs K<sup>+</sup> Channels. *ACS Nano* **2015**, *9* (5), 4827–4834.

<https://doi.org/10.1021/nn506164s>.

(42) Gu, Z.; Plant, L. D.; Meng, X. Y.; Perez-Aguilar, J. M.; Wang, Z.; Dong, M.; Logothetis, D. E.; Zhou, R. Exploring the Nanotoxicology of MoS<sub>2</sub>: A Study on the Interaction of MoS<sub>2</sub> Nanoflakes and K<sup>+</sup> Channels. *ACS Nano* **2018**, *12* (1), 705–717.

<https://doi.org/10.1021/acsnano.7b07871>.

(43) Kraszewski, S.; Tarek, M.; Treptow, W.; Ramseyer, C. Affinity of C60 Neat Fullerenes with Membrane Proteins: A Computational Study on Potassium Channels. *ACS Nano* **2010**, *4* (7), 4158–4164. <https://doi.org/10.1021/nn100723r>.

(44) Dante, S.; Petrelli, A.; Petrini, E. M.; Marotta, R.; Maccione, A.; Alabastri, A.; Quarta, A.; De Donato, F.; Ravasenga, T.; Sathya, A.; Cingolani, R.; Proietti Zaccaria, R.; Berdondini, L.; Barberis, A.; Pellegrino, T. Selective Targeting of Neurons with Inorganic Nanoparticles: Revealing the Crucial Role of Nanoparticle Surface Charge. *ACS Nano* **2017**, *11* (7), 6630–6640.

<https://doi.org/10.1021/acsnano.7b00397>.

(45) Phillips, R.; Ursell, T.; Wiggins, P.; Sens, P. Emerging Roles for Lipids in Shaping Membrane-Protein Function. *Nature* **2009**, *459* (7245), 379–385.

<https://doi.org/10.1038/nature08147>.

(46) Wang, B.; Zhang, L.; Sung, C. B.; Granick, S. Nanoparticle-Induced Surface Reconstruction of Phospholipid Membranes. *Proc. Natl. Acad. Sci. U. S. A.* **2008**, *105* (47), 18171–18175.

<https://doi.org/10.1073/pnas.0807296105>.

## **Chapter 2: Anionic nanoparticle-induced perturbation to phospholipid membranes affects ion channel function**

The following chapter is adapted from the article published in Proceedings of the National Academy of Sciences\*, 2020, 117 (45), 27854-27861 (DOI: 10.1073/pnas.2004736117), with the following co-authors: Dongyue Liang, Elizabeth D. Laudadio, Jorge D. Calderin, Meng Wu, Puspam Keshri, Xianzhi Zhang, Michael P. Schwartz, Robert J. Hamers, Vincent M. Rotello, Catherine J. Murphy, Qiang Cui, and Joel A. Pedersen

\*Contributions to this publication include: Conceptualization, methodology, experimental design and data collection, and writing and editing of the manuscript.

### **2.1 Introduction**

Nanoparticles, virus-sized objects that can be composed of organic or inorganic materials, show considerable promise as bioimaging agents, drug delivery vehicles, and even as therapeutic agents themselves<sup>1-3</sup>. Many of these technologies would benefit from a deeper understanding of how nanoparticles interact with biological membranes to enable the design of new nanomaterials with improved efficiencies and to minimize negative biological impacts. Nanoparticle properties such as core composition, size, shape, and surface functionalization can each influence membrane interactions and subsequent biological outcomes, including internalization<sup>4-10</sup>, membrane damage<sup>11-13</sup>, alteration of membrane function<sup>14,15</sup>, and initiation of cellular signaling cascades<sup>16</sup>. Experimental model membrane systems such as lipid vesicles<sup>17-20</sup>, supported lipid bilayers<sup>21-24</sup>, lipid monolayers<sup>25,26</sup>, and planar suspended bilayers<sup>27</sup> have been employed to gain insight into mechanisms of nanoparticle interaction with biological membranes and to inform *in vivo* investigations that correlate nanoparticle properties to cellular outcomes such as toxicity. For example, the binding to and disruption of model membranes by poly(ethyleneglycol)-functionalized quantum dots and polycation-coated diamond nanoparticles

have been correlated to bacterial membrane damage that ultimately reduces cell viability<sup>17,28,29</sup>. Amphiphilic and lipophilic nanoparticles can induce defects in model membranes and cells<sup>30</sup> or embed in lipid bilayers<sup>27,31</sup>. Atomistic and coarse-grained molecular dynamics simulations and analytical modeling have provided important insights into nanoparticle interaction with the lipid bilayer of cellular membranes<sup>13,31–33</sup>. While the majority of prior investigations of nanoparticle interaction with model membrane systems have relied on lipid bilayers composed of single phospholipids or binary mixtures<sup>19,23,24,26,34</sup> recent efforts have begun to investigate the influence of other important membrane components on nanoparticle binding such as cell surface glycans and membrane proteins<sup>35–37</sup> to provide deeper insight into how the chemistry of cell surfaces facilitates nanoparticle binding.

Ion channels comprise a class of embedded membrane proteins that are critical for maintaining cellular homeostasis and other biological functions (e.g., epithelial transport, immune cell activation, conduction of nerve impulses, muscle contraction)<sup>38</sup>. Nanoparticles can disrupt the function of ion channels in membranes<sup>14,39–41</sup>, altering ion channel gating<sup>39</sup> and membrane potentials<sup>14,42</sup>. For example, while anionic nanoparticles are often considered non-toxic<sup>29</sup>, they have been shown to preferentially interact with neuronal membranes (vs. glial cells) and modulate their excitability, whereas such effects were not induced by cationic or neutral nanoparticles<sup>15</sup>. Computational and experimental studies have provided evidence that some nanomaterials can decrease ion channel function by blocking the channel entrance or by altering protein conformation via binding to extracellular domains<sup>40,43–45</sup>. Nanoparticle-induced perturbation to the mechanical properties of phospholipid bilayers has also been invoked as a potential explanation for observed disruption of ion channel function<sup>39,41,42</sup>. The binding of nanoparticles to phospholipid bilayers can alter the mechanical properties of membranes<sup>19</sup>, but

evidence correlating changes in membrane properties to altered ion channel (or other membrane protein) function has hitherto been inconclusive.

Here, we combine experiments and simulations to investigate nanoparticle-membrane interactions and concomitant effects on the function of embedded ion channels. We employed voltage-clamp electrophysiology measurements on planar suspended lipid bilayers to demonstrate that anionic gold nanoparticles (AuNPs), often considered among the most benign nanoparticles<sup>29</sup>, alter the function of embedded mechanosensitive gramicidin A ion channels without disrupting the membrane itself. Assembly of gramicidin A monomers into membrane-spanning, ion-conducting dimers is sensitive to the bilayer deformation energy<sup>46</sup>. We used attenuated total reflectance-Fourier-transform infrared (ATR-FTIR) spectroscopy and molecular dynamics simulations to obtain evidence that anionic AuNPs interactions subtly change membrane mechanical properties without directly altering the structure of embedded gramicidin A dimers. Our results provide insight into an indirect, phospholipid bilayer-mediated mode of nanoparticle-induced modulation of membrane protein function that was previously hypothesized, but not demonstrated to occur<sup>39,41,42</sup>. Indirect effects of nanoparticles mediated by changes in the biophysical properties of the lipid bilayer are expected to influence the function of membrane proteins – both mechanically gated ion channels (for which gramicidin A serves as a model) and others, whose activities exhibit sensitivity to the properties of the bilayer<sup>46,47</sup>. Our study also serves as a proof-of-concept demonstration of modeling a functional membrane system to assess the effects of nanoparticle binding on ion channel function.

## 2.2 Materials and Methods

### 2.2.1 Ligand and gold nanoparticle synthesis

The TCOOH ligand was synthesized according to the scheme in Figure 1. Compound **2** was synthesized following the reported literature <sup>48</sup>. To synthesize compound **3**, 1.56 g (2.76 mmol, 1 eq) of compound **2** was taken in a round bottom flask containing 15 mL of tetrahydrofuran (THF). The flask was cooled to 0 °C in an ice bath. After cooling, NaH (0.33 g, 13.37 mmol, 5 eq) was added to three portions (within 10 min). After stirring this mixture for 30 min at 0 °C, ethyl bromoacetate (0.91 mL, 8.26 mmol, 3 eq) was added to it. The solution was allowed to stir at room temperature for 16 h. The remaining NaH was quenched with methanol (MeOH) followed by EtOAc (Ethyl Acetate) (3 × 30 mL). The organic layer was separated, dried (Na<sub>2</sub>SO<sub>4</sub>) and concentrated at reduced pressure. The crude product was purified by column chromatography over silica gel using hexane/ethyl acetate (1:1) as an eluent. Solvent was removed in vacuum to afford compound **3** as a colorless oil (yield = 1.04 g, 52%). <sup>1</sup>H NMR (400 MHz, CDCl<sub>3</sub>): δ 1.21-1.46 (m, 19H), 1.58 (pent, 2H), 2.15 (t, 2H), 3.45 (t, 2H), 3.60-3.75 (m, 16H), 4.17 (s, 2H), 4.23 (q, 2H), 7.22-7.31 (m, 9H), 7.42-7.44 (m, 6H).

To synthesize compound **4**, compound **3** (1.04 g, 1.44 mmol, 1 eq) was dissolved in THF (15 mL). LiOH. H<sub>2</sub>O (0.18 g, 4.32 mmol, 3 eq) was dissolved in 15 mL of distilled water and then added to the solution of compound **3**. The mixture was allowed to stir at room temperature for 16 h. After 16 h, 1 M HCl was added to the reaction mixture to adjust the pH to 1-2. This was followed by the work up using EtOAc (3 × 30 mL). Afterward, the organic layer was separated, dried (Na<sub>2</sub>SO<sub>4</sub>) and concentrated at reduced pressure. The crude product was purified by column chromatography over silica gel using chloroform/methanol (17:3) as an eluent. Solvent was removed in vacuum to afford compound **4** as a colorless oil (yield 0.87 g, 87 %). <sup>1</sup>H NMR (400 MHz, CDCl<sub>3</sub>): δ 1.16-1.41 (m, 16H), 1.55 (pent, 2H), 2.13 (t, 2H), 3.45 (t, 2H), 3.59-3.75 (m, 14H), 4.15 (s, 2H), 7.20-7.33 (m, 9H), 7.40-7.42 (m, 6H).

Compound **5** (TCOOH) was synthesized from compound **4** as follows. Compound **4** (400 mg) was dissolved in 5 mL of dichloromethane (DCM) and purged with nitrogen for 5 min. 1 mL of TFA was added

to the mixture in nitrogen atmosphere and allowed to stir for 20 min. Afterward, triisopropylsilane (0.4 mL) was added to the mixture and kept stirring at room temperature for 16 h under nitrogen atmosphere. It was then washed with hexane (twice), hexane-DCM (7:3) (twice), hexane-DCM (3:7) (twice), DCM (twice). Solvent was removed in vacuum to afford compound **5** as a colorless oil (yield = 180 mg, 67 %).  $^1\text{H NMR}$  (400 MHz,  $\text{CDCl}_3$ ):  $\delta$  1.26-1.39 (m, 14H), 1.54-1.70 (m, 4H), 2.51 (q, 2H), 3.47 (t, 2H), 3.59-3.78 (m, 16H), 4.16 (s, 2H).

Gold nanoparticles for TCOOH ligand exchange were synthesized by Brust-Schiffrin two-phase method<sup>49,50</sup>. In brief, 1 g of  $\text{HAuCl}_4$  was dissolved in 150 mL water and 150 mL toluene. Tetraoctylammonium bromide (TOAB, 2.1 g) was added with maximum stirring speed. Pentanethiol (0.7 mL) was added dropwise until whole solution turned into white. Sodium borohydride (2.0 g) was dissolved in 8 mL water and added into the white solution immediately. After 5 h of stirring, organic layer was separated and dried under reduced pressure in room temperature. The residue was dissolved in hexanes and washed with acetonitrile 80 times until all TOAB were fully removed.

To perform a ligand exchange, 40 mg of gold core was dissolved in 4 mL of DCM under argon. Ligand (120 mg) in 2 mL DCM and 2 mL MeOH was added to solution dropwise under argon and stirred in room temperature for 72 h. Solvents were removed under reduced pressure, and precipitates were washed three times each with hexanes and hexanes/DCM mixture (1:1 v/v). Then solid was dissolved in ultrapure water ( $>18 \text{ M}\Omega\cdot\text{cm}$ ) and dialyzed for 3 days. The gold nanoparticles had diameters of  $2.1 \pm 0.2 \text{ nm}$ , as measured by transmission electron microscopy (TEM) (Figure 2). Ligand density was determined previously using matrix-assisted laser desorption/ionization mass spectrometry and found to be  $\sim 63 \text{ ligands/NP}$  or  $\sim 5 \text{ ligands}\cdot\text{nm}^{-2}$ <sup>51</sup>.

The 3-mercaptopropionic acid (MPA) AuNPs were synthesized by an adapted existing protocol as follows<sup>52</sup>.  $\text{HAuCl}_4$  (3.53 mL, 0.1 M) was added to 450 mL ultrapure water in an Erlenmeyer flask, and 212  $\mu\text{L}$  of 0.1 M MPA was added to the aqueous solution. The solution pH was adjusted to  $\sim 8.5$  using 1 M NaOH, and stirred for 10 min. Fresh 0.1 M  $\text{NaBH}_4$  solution (6.4 mL) was added to the above reaction mixture. The combined solutions rapidly changed color to a deep red-brown, and the reaction mixture was

stirred for 2 h. The MPA-AuNPs were concentrated by a customized flow reactor with a 30 kDa MWCO membrane to a ~30 mL volume<sup>53</sup>. The concentrated MPA-AuNPs were purified by centrifugation at 13,000g for 55 min twice. For TEM imaging, 5  $\mu$ L of a dilute solution of AuNPs was drop cast onto a TEM grid (Ted Pella), and the AuNPs sample images were taken with a JEOL 2100 cryo TEM.

The UV-vis spectrum of MPA-AuNPs are shown in Figure 2. The diameter of MPA-AuNP were estimated in solution by UV-vis spectroscopy to be around 4.6 nm<sup>54</sup>. TEM image analysis indicated that the core diameter of MPA-AuNPs were  $4.7 \pm 1.3$  nm ( $n > 200$ ). A representative TEM image is shown in Figure 2.

### 2.2.2 Characterization of gold nanoparticles

For transmission electron microscopy (TEM) imaging, 4.5  $\mu$ L of a dilute solution of MPA-AuNPs was drop-cast onto a TEM grid (Ted Pella), and images were acquired with a JEOL 2100 TEM. For TCOOH-AuNPs, 5-10  $\mu$ L of 1  $\mu$ M AuNPs were drop-cast onto 300 Square Mesh, Nickel Grids (EMS FF300-Ni) and images were acquired using a TEM JEOL 2000FX instrument at an acceleration voltage of 200 kV. The UV-vis spectra of the TCOOH- and MPA-AuNP suspensions were acquired on a Molecular Devices Spectramax M2 Plate Reader and a Cary 500 Scanning UV-vis spectrophotometer, respectively. Nanoparticle hydrodynamic diameters and  $\zeta$ -potentials were determined in 0.150 M KCl buffered to pH 7.4 with 0.01 M HEPES by dynamic light scattering (DLS) and laser Doppler electrophoresis (Malvern Zetasizer Nano ZS). Reported hydrodynamic diameters and  $\zeta$ -potentials represent the means of 10 and 12 replicates, respectively (Table 1).

### 2.2.3 Nanoparticle ligand density by X-Ray Photoelectron Spectroscopy (XPS)

We quantified the number of MPA ligands on the AuNPs by XPS using a previously established approach<sup>55</sup> to determine the concentration of malonic acid to use as a ligand surrogate in electrophysiology control experiments. Two sets of samples were prepared for XPS analysis: stock and washed MPA-AuNPs. The washed samples in ultrapure water ( $>18$  M $\Omega$ ·cm)

were prepared by isolating MPA-AuNPs from free ligand in solution via centrifugation of 50  $\mu\text{L}$  MPA-AuNP stock for 8 min at 14100g. Both sets of samples were drop-cast (2 or 1  $\mu\text{L}$ , respectively) onto planar Si substrates (previously sonicated in isopropyl alcohol for 10 min and dried under a stream of nitrogen gas), and the droplet was allowed to dry. XPS spectra were collected using a custom-built, ultrahigh-vacuum Phi XPS system with a base pressure of  $10^{-9}$  torr. X-rays were provided by an Al  $k\alpha$  source (1486.6 eV photon energy) with a quartz-crystal monochromator and a hemispherical electron energy analyzer. Measurements were taken with pass energies of 58.7 eV. An electron collection angle of  $45^\circ$  with respect to the surface normal was used for all experiments. The XPS spectra were fit using CasaXPS software 2.3.16 ([www.casaxps.com](http://www.casaxps.com)). Experimental XPS data were compared with computed results using a previously reported model<sup>55</sup>. The computed C:Au ratio from the model was compared with that calculated from the experimental data to obtain an organic layer thickness. Layer thickness was converted to molecular density using the density of the MPA ligand, and the surface area of the particle was used to approximate the concentration of MPA ligand on a single MPA-AuNP. Data were analyzed using CasaXPS, software version 2.3.16. Ligand coverages calculated for each set of samples were within 84% of one another when measured in triplicate. Ligand density determined by this XPS method was  $\sim 23$  ligands $\cdot\text{nm}^{-2}$ .

#### **2.2.4 Preparation of planar suspended lipid bilayers and Voltage-Clamp electrophysiology**

We prepared planar suspended phospholipid bilayers by painting<sup>56</sup> *n*-decane solutions of DPhPC containing gA across 150  $\mu\text{m}$  apertures in Delrin cups (Warner Instruments, Camden, CT). We used DPhPC because of its high stability when used to construct suspended bilayers<sup>57</sup>. The experimental set-up is depicted in Figure 3. Briefly, we combined 0.5 mg of DPhPC from 25  $\text{g}\cdot\text{L}^{-1}$  chloroform stock with 2 to 10  $\mu\text{g}$  gA in 2,2,2-trifluoroethanol. The mixture was then placed

under vacuum for at least 1 h to remove the solvents. We dissolved the resultant lipid film in 20  $\mu\text{L}$  of *n*-decane and allowed the solution to sit for 10-15 min before use. The aperture was pre-coated with the DPhPC solution containing gA and allowed to dry. The cup was placed into the sample holder of the planar lipid bilayer workstation (Warner Instruments, Camden, CT), and the cup and chamber were filled with 1 mL of 0.15 M KCl buffered to pH 7 with 0.010 M HEPES. Bilayers were formed by swirling an elbow-shaped glass tube in the lipid solution and briefly occluding one side of the aperture until a highly capacitive ( $>40$  pF) structure indicative of a planar bilayer membrane was formed.

In voltage-clamp electrophysiology a constant transmembrane potential is applied across a phospholipid bilayer and current passage through the membrane is monitored. Electrophysiology experiments were conducted using a planar bilayer membrane workstation (Warner Instruments) shown schematically in Figure 3. These experiments employed planar suspended DPhPC bilayer membranes exhibiting capacitances  $>40$  pF, higher than the intrinsic 25 pF capacitance of a bubble occluding the Delrin aperture<sup>58</sup>, yet lower than the maximum bilayer capacitance at 100-200 pF<sup>59</sup>. Capacitance was determined by the application of a  $\pm 1$  V sawtooth potential waveform<sup>60</sup>. Gramicidin A-containing planar suspended lipid bilayer membranes used in electrophysiology experiments displayed consistent ion channel activity (similar number of active channels present) for 10-15 min under +50 mV transmembrane DC potential prior to nanoparticle addition. After monitoring bilayer-incorporated gA activity for 10-15 min in 0.15 M KCl buffered to pH 7 with 0.010 M HEPES, TCOOH- or MPA-AuNPs were sequentially added to final concentrations of 1, 3, and 5 nM (particle number concentration) to either the *cis* (ground) or *trans* (input) wells, or to both. In the majority of experiments, AuNPs were added to both sides of the planar suspended bilayer membrane to avoid electrophoretic effects arising from sidedness<sup>46,61-66</sup>, and membrane

conductance was measured under +50 mV applied transmembrane DC potential for 10-15 min after each addition of AuNPs. Experiments in which AuNPs were added to only one side of the membrane were conducted to verify that results were consistent regardless of whether nanoparticles were added to both or to only one side of the bilayer. In experiments in which AuNPs were added to only one side of the bilayer, a negative transmembrane potential was achieved by imposing a negative -50 mV bias on input electrode (*trans*) and adding nanoparticles to the solution corresponding to the ground electrode (*cis*). This orientation is analogous to addition of nanoparticles to the outside of a cell, which usually bears a negative transmembrane potential inside relative to outside. A subset of experiments were conducted to examine the effect of malonic acid (as a surrogate for MPA) on gA activity in the planar suspended bilayer membranes.

Electrophysiology experiments were performed in triplicate at  $25 (\pm 0.2)$  °C. Each replicate represents a unique bilayer, and data were averaged over 3.0-6.5 min time frames per replicate depending on channel activity. The desired number of channels prior to addition of AuNPs or malonic acid was >500 per analysis frame (3.0 to 6.5 min). A high channel density is required for statistical analysis of channel lifetimes, and the analysis frame was chosen accordingly. Values for numbers of channels ( $N$ ), channel lifetimes ( $\tau$ ), and single-channel currents ( $g$ ) depend sensitively on the amount of *n*-decane trapped between acyl chains of the lipids in the bilayer, a factor that is not easily controllable in bilayer lipid membranes formed using the painting method. Thus, each replicate (representing a unique bilayer) is normalized to its starting value for each figure of merit, which is then averaged across three replicates to assess the degree to which each is altered by exposure to AuNPs.

Electrophysiology traces were analyzed over selected analysis frames for single-channel activity using the single channel search feature of Clampfit 10.6 (Molecular Devices). Single-

channel currents were determined by dividing each current by the corresponding number of channels and averaging the resulting values. A representative single-channel current trace for a DPhPC bilayer containing grA is shown in Figure 2B. The trace depicts changes in the number of gA channel formation events, as measured by quantized current levels, where a single gA channel passes  $1.00 \pm 0.14$  pA.

To determine channel lifetimes ( $\tau$ ), raw lifetime data from the single channel search feature was binned according to Sturge's Rule <sup>67</sup>:

$$k = 1 + 3.222(\log_{10}(n)) \quad (1)$$

where bin size ( $k$ ) is determined from the number of data points ( $n$ ). Average single-channel lifetimes were then determined by applying a statistical function on the binned lifetime data based on previous studies <sup>68,69</sup>:

$$\ln\left(\frac{N(t)}{N(0)}\right) = t \cdot \left(-\frac{1}{\tau}\right) \quad (2)$$

where  $N(t)$  is the number of channels in each bin,  $N(0)$  is the total number of channels,  $t$  is the binned time, and  $\tau$  is the average lifetime. Plotting  $\ln(N(0)/N(t))$  vs.  $t$  allows  $\tau$  to be determined from the slope.

For channel lifetimes, error was determined as that solely between replicates, as the original quantification does not contain measurable error. Error in lifetimes and single channel currents were determined by propagation of error for each replicate followed by propagation among averaging between replicates.

## 2.2.5 Preparation and characterization of small unilamellar vesicles (SUVs)

Small unilamellar vesicles for use in attenuated total reflectance-Fourier transform infrared spectroscopy studies (*vide infra*) were prepared by the extrusion method. Briefly, DPhPC lipids (0.846 mg) in a  $25 \text{ mg}\cdot\text{mL}^{-1}$  chloroform stock mixed with 0.05 mg gA dissolved in 2,2-

trifluoroethanol. The solvents were under a stream of ultrapure N<sub>2</sub> gas, and the lipid film was rehydrated in 0.150 M KCl buffered to pH 7.4 using 0.01 M HEPES. After sonication for 30 min, the solution was extruded 11 times through a 0.05 μm polycarbonate filter (Whatman) using an extrusion kit (Avanti Polar Lipids). Vesicles suspensions (1 mM in DPhPC and 0.0265 mM in gA) were stored at 4 °C and used within 1 week of extrusion. Hydrodynamic diameters and ζ-potentials of the vesicles in 0.150 M KCl buffered to pH 7.4 with 0.01 M HEPES were determined by DLS and laser Doppler electrophoresis as described above. These data are reported below.

### **2.2.6 Attenuated Total Reflectance–Fourier Transform Infrared (ATR-FTIR) Spectroscopy**

We used ATR-FTIR spectroscopy to probe the changes in the vibrational spectra of supported layers of DPhPC vesicles containing gA upon interaction with TCOOH- and MPA-AuNPs. Small unilamellar vesicles had a number average diameter of  $82 \pm 2.4$  nm (Z-average diameter of  $117 \pm 1.4$  nm, PDI of  $0.14 \pm 0.04$ ) and a ζ-potential of  $-4.4 \pm 1.2$  mV. These small unilamellar vesicles (1 mM) were drop-cast via pipette onto a single-bounce monolithic diamond internal reflection element (GladiATR, Pike Technologies) mounted in a Bruker Vertex 70 instrument with a LN-MCT (liquid nitrogen-cooled HgCdTe) detector. The diamond surface was cleaned with ethanol and water in between experiments. All data were acquired in triplicate. For both background and sample spectra, 300 scans were averaged at a  $2 \text{ cm}^{-1}$  resolution. A Blackman-Harris 3-term apodization function, Mentz phase correction mode, and zero-filling factor of two were used in all cases. Single channel spectra were collected and converted to absorbance spectra using Igor Pro version 6.3.7.2 ([www.wavemetrics.com](http://www.wavemetrics.com)).

### 2.2.7 Molecular Dynamics (MD) Simulations

We applied MD simulations to explore the interaction between nanoparticles, the gA dimer and lipid membrane at the microscopic level. In addition to the DPhPC bilayer studied experimentally, we also studied the case of DMPC (1,2-dimyristoyl-sn-glycero-3-phosphocholine) to evaluate the generality of the observed trends. For each type of lipid, we embedded a gA dimer in a pure lipid bilayer; for comparison, simulations were also carried out without the embedded gA dimer. The initial structure of the gA dimer was taken from PDB:1JNO<sup>70</sup>. For all the MD simulations, the CHARMM36<sup>71-74</sup> force field was used for nanoparticle ligands, lipids, proteins, ions and water. The membrane builder module of CHARMM-GUI<sup>75-77</sup> input generator was used for system assembly, and the dimensionality of the simulated system was approximately  $10 \times 10 \times 8 \text{ nm}^3$ , and the  $z$  dimension (membrane normal) was extended to 13 nm when the AuNP (and additional water and ions) was introduced into the system. The NaCl salt concentration of 0.15M was applied in all the simulations. Each lipid bilayer-gA system was first equilibrated for 375 ps<sup>76,77</sup> during which harmonic restraints were applied to protein backbones, sidechains and lipid. After equilibration, each system was assembled with pre-equilibrated MPA-AuNP, including the water molecules and ions within the first shell; to mimic the situation when MPA-AuNP approaches the gA channel, the initial location of the MPA-AuNP was set to be on top of the gA channel with a distance of  $\sim 15 \text{ \AA}$  (see Figure 7). The MPA-AuNP model consisted of a 2-nm-diameter AuNP functionalized with 72 MPA ligands (with a surface ligand density  $\sim 5.7 \text{ nm}^{-2}$ ), which are randomly distributed on the surface; we explored two titration states for the MPA ligands, where all or approximately half<sup>78,79</sup> MPA ligands were charged. The INTERFACE force field<sup>80</sup> was used for the gold atoms, which was shown to be reliable in our previous work<sup>81</sup>. Replicas of production runs were performed with the assembled systems for 100 ns each.

For comparison, simulations have also been conducted for a single TCOOH-AuNP and four MPA-AuNP aggregated together interacting with a DPhPC bilayer. For the TCOOH-AuNP, three independent simulations of at least 100 ns each were conducted; for the aggregated MPA-AuNPs system, the simulation is 100 ns in length. In the latter setup, a set of harmonic restraints was applied to the centers of mass for the MPA-AuNPs to maintain their spatial proximity in the  $x$ - $y$  plane and alignment along the  $z$  axis; the force constant for the horizontal restraints is  $50 \text{ kcal}\cdot\text{mol}^{-1}\cdot\text{\AA}^{-2}$ , and that for the vertical ( $z$ ) restraint is  $1000 \text{ kcal}\cdot\text{mol}^{-1}\cdot\text{\AA}^{-2}$ .

All simulations were performed with the NAMD<sup>82</sup> simulation package. Particle-Mesh-Ewald<sup>78</sup> was used to treat electrostatic interactions with a grid spacing of  $1 \text{ \AA}$  and a real-space cutoff of  $12 \text{ \AA}$ . Force switching with a switching distance of  $10 \text{ \AA}$  was applied for van der Waals interactions. The SHAKE<sup>83</sup> algorithm was applied to all bonds involving hydrogens, allowing an integration time step of  $2 \text{ fs}$ . Langevin dynamics with a damping coefficient of  $1.0 \text{ ps}^{-1}$  was applied for temperature control, and the Nosé-Hoover Langevin piston<sup>84,85</sup> was applied for constant pressure control. The temperature of the simulations was set to  $303.15\text{K}$ , and the pressure was set to  $1 \text{ atm}$  with the  $x$ - $y$  ratio of the box fixed at  $1$ . CHARMM<sup>86</sup>, VMD<sup>87</sup> and the MDAnalysis<sup>88,89</sup> tool were applied for analysis and visualization.

## 2.3 Results and Discussion

### 2.3.1 Anionic AuNPs Impact Ion Channel Function

Electrophysiology was employed to measure the impact of anionic gold nanoparticles (AuNPs) on the function of gramicidin A (gA) ion channels embedded in 1,2-diphytanoyl-*sn*-glycero-3-phosphocholine (DPhPC) bilayers (see Methods). Bilayers composed of DPhPC are frequently used in studies of ion conductivity because they exhibit characteristics desirable for electrophysiology studies including high mechanical and chemical stability, high electrical resistance, and low ion and water permeability, and they remain in the biologically relevant liquid crystalline (i.e., fluid) phase over a broad temperature range ( $-120$  to  $120$  °C)<sup>90</sup>. Gramicidin A is a well-studied bacterial mechanosensitive peptidic ion channel<sup>91-94</sup> that shares several features with larger ion channels, including the dependence of its ion gating on bilayer deformation<sup>46,95</sup> and the presence of tryptophan residues at the bilayer-solution interface<sup>96</sup>. Gramicidin A-containing lipid bilayers provide a convenient and robust platform to investigate membrane-mediated impacts on ion channel function.

AuNPs were functionalized with either short (mercaptopropionic acid, MPA) or long (mercaptodecanoic-tetraethyleneglycol-carboxylate, TCOOH) anionic ligands to probe the presentation of carboxyl groups on interactions with gA-containing membranes (Table 1). The MPA-AuNPs exhibited  $\zeta$ -potentials of  $-29.4 \pm 0.99$  mV and underwent considerable aggregation in the buffer used for electrophysiology experiments. Specifically, while MPA-AuNPs possessed a core diameter of  $5.4 \pm 1.6$  nm based on TEM measurements, the hydrodynamic diameter measured in electrophysiology buffer was  $360 \pm 61$  nm (Table 1). TCOOH-AuNPs in electrophysiology buffer had a  $\zeta$ -potential of  $-8.9 \pm 0.40$  mV and aggregated to a smaller extent than MPA-AuNPs (core diameter =  $2.1 \pm 0.2$  nm, hydrodynamic diameter =  $20 \pm 15$  nm; Table 1).

The MPA-AuNPs and TCOOH-AuNPs thus had distinct sizes, aggregation states, and  $\zeta$ -potentials in the buffer used here.

Ion channel function was first measured for gA-containing membranes by adding anionic AuNPs to both sides of the membrane to minimize any electrophoretic effects or membrane pressure changes that might complicate interpretation of changes in ion channel function. Ion channel function was quantified for embedded gA-ion channels by measuring the number ( $N(t)$ ), lifetime ( $\tau$ ), and single-channel current ( $g$ ) via voltage-clamp electrophysiology (Fig. 1A and B). Exposure of gA-containing membranes to a gradient of either TCOOH- or MPA-AuNPs reduced gA ion channel activity (number of channels per unit time;  $p < 0.05$ ) and extended single-channel lifetimes ( $p < 0.001$ ) in a dose-dependent manner, but did not alter single-channel current (Fig. 2, Fig. 3).

Similar trends were observed for changes in ion channel function when 1 nM MPA-AuNPs was introduced to only the side of the membrane corresponding to the exterior (extracellular side) of a biological cell (Fig. 3-4). We note that although the terminal carboxylate groups of ligands decorating the AuNPs may bind potassium cations, the number of ions sequestered at the nanoparticle concentration used would be insufficient to appreciably change the  $K^+$  concentration of the solution. Using the determined ligand densities and assuming that every ligand is deprotonated and binds one  $K^+$  cation, we find that 5 nM MPA- and TCOOH-AuNPs (the highest concentrations used) would decrease the  $K^+$  ion concentrations by  $< 0.01\%$ . This change in  $K^+$  concentration is too small to appreciably alter channel conductance. Indeed, single-channel current is unaltered by exposure to the anionic AuNPs over the concentration range used (Fig. 2 G & H).

The observed changes in the number of gA channels and their lifetimes is instead largely consistent with a change in membrane mechanical properties, although activity and lifetime do not

change in parallel as they do for molecular species<sup>66</sup>. We note that dosing with free malonate (chosen as a free ligand control) at a concentration equivalent to total ligand on 1 nM MPA-AuNPs (Fig. 3) did not significantly alter channel activity or single-channel current ( $p > 0.05$ ), but *reduced* channel lifetimes relative to control ( $p < 0.05$ , Fig. 3), in contrast to the *increase* in lifetime observed for both MPA- and TCOOH-AuNPs. Taken together, our results indicate that anionic AuNPs alter gA function similarly despite differences in carboxyl-bearing ligands (MPA vs. TCOOH), aggregation state (approx. 360 vs. 20 nm hydrodynamic diameter), and  $\zeta$ -potential (approximately  $-9$  vs.  $-29$  mV), but that the effect of the nanoparticles differs mechanistically from that of free ligand in solution.

### 2.3.2 Anionic AuNPs Do Not Impact gA Conformation

We used ATR-FTIR spectroscopy to probe perturbations of gA embedded in DPhPC vesicles induced by interactions with MPA- or TCOOH-AuNPs (Fig. 6). We focused our analysis on the Amide I (dominated by backbone C=O stretching vibrations) and Amide II (dominated by N-H stretching vibrations) regions of the vibrational spectra. The Amide I band is particularly sensitive to secondary structure of the peptide backbone<sup>97</sup>. The FTIR spectra of gA-containing vesicles exposed to MPA- or TCOOH- AuNPs were first referenced to gA-free vesicles to assess gA-related peaks in the Amide I and II regions (Fig. 6A). The Amide I peaks at Amide peaks at  $1630\text{ cm}^{-1}$ , and  $\sim 1668\text{ cm}^{-1}$  (shoulder) and the Amide II peak at  $1548\text{ cm}^{-1}$  for gA-containing vesicles are consistent with previously reported vibrational spectra for gA ion channels embedded in lipid vesicles<sup>98-100</sup>. Exposure to MPA- or TCOOH-AuNPs (Fig. 6A) resulted in a reduction in peak intensities relative to gA-containing vesicles alone, but peak positions remained unchanged.

We also referenced spectra for gA-containing vesicles exposed to AuNPs to gA-containing vesicles alone to isolate peak intensity changes specific to nanoparticle exposure (Fig. 6B). Amide

I and II absorbances decreased for gA-containing vesicles exposed to MPA- or TCOOH-AuNPs compared to gA-containing vesicles alone (Fig. 6B), resulting in inverted peaks (compared to spectra in Fig. 6A). However, Amide I and II peak ratios were similar for gA-containing vesicles exposed to MPA- or TCOOH-AuNPs (Fig. 6B), consistent with interactions being similar for both AuNP types. We note that peak shapes in the Amide I and II regions for gA-containing vesicles exposed to AuNPs (referenced to gA-containing vesicles) were similar to gA-containing vesicles alone (referenced to DPhPC vesicles). Thus, the primary effect of exposing gA-containing vesicles to AuNPs was a uniform decrease in overall peak intensity across the Amide I and II region without changing relative peak positions or peak shapes. Based on these combined results, we conclude that any perturbation in gA conformation due to interaction with anionic AuNPs was minimal.

### 2.3.3 MPA-AuNPs Perturb Local Membrane Properties

To obtain further mechanistic insight into the interaction of anionic AuNP interaction with gA ion channels embedded in lipid bilayers, we performed molecular dynamics (MD) simulations on a single MPA-AuNP in proximity to a single gA ion channel embedded in a DPhPC bilayer. We note that MPA- and TCOOH-AuNPs differ in several relevant properties (Table 1), but experimental results are consistent with similar interactions with gA-containing bilayers. We therefore also conducted simulations for a TCOOH-AuNP as well as four MPA-AuNPs aggregated together. Both show qualitatively similar behaviors as the single MPA-AuNP; thus our analysis has focused on the MPA-AuNP system. We found that regardless of the titration state (fully or half deprotonated) of the MPA ligands, the MPA-AuNP remains on the lipid bilayers for the majority of the 100-ns simulations with a distance of  $\sim 2.5$  to  $5 \text{ \AA}$  (Fig. 7), indicating stable adsorption. The nanoparticle, however, did not consistently exhibit attraction to the gA dimer; it remained close to the gA dimer in some trajectories, but drifted away in others (Fig. 7B).

We computed the root mean square difference (RMSD) of the gA backbone with respect to the crystal structure (Fig. 8) and the number of backbone hydrogen bonds formed within the gA dimer (Fig. 9) from the MD trajectories. In general, the results indicate that the presence of MPA-AuNP leads to very little perturbation on the gA structure, in agreement with FTIR results. To test the generality of the observed trends, we also conducted simulations for MPA-AuNP with a gA embedded in a 1,2-dimyristoyl-*sn*-glycero-3-phosphocholine (DMPC) bilayer. The mode of interaction between MPA-AuNP and gA was found to be similar for both DPhPC and DMPC bilayers.

Since little direct impact on the gA channel from the MPA-AuNP is observed, we hypothesized that the effect on the gA channel lifetime stems from a change in local lipid properties upon MPA-AuNP adsorption. As discussed below and shown by Andersen and coworkers<sup>101</sup>, local bilayer thickness (i.e., hydrophobic mismatch) and mechanical properties play an important role in determining the gA channel lifetime. To focus on the effect of MPA-AuNP on lipid properties, we measured the hydrophobic thickness and area compressibility modulus of the bilayer in MD simulations of MPA-AuNP assembled with a lipid bilayer without the gA dimer. The hydrophobic thickness of the bilayer is commonly defined as the average thickness given by C2 carbon atoms of the acyl tail of lipids in opposing leaflets<sup>94</sup>, and the area compressibility modulus ( $K_A$ ) is related to the mean square fluctuation in lipid area ( $A$ )<sup>102</sup>:

$$K_A = \frac{k_B T \langle A \rangle}{\langle \delta A^2 \rangle}$$

where  $k_B$  is the Boltzmann constant and  $T$  is absolute temperature.

The impact of MPA-AuNP adsorption on local lipid properties was evaluated for a DPhPC bilayer with several independent 100-ns trajectories in the presence of an MPA-AuNP in either titration state. Since the DPhPC bilayer is rather stiff due to the packing of additional methyl

groups along the acyl chains, adsorption of the MPA-AuNP did not lead to significant local thinning of the bilayer, as shown in Figure 10 ; that is, the mean hydrophobic thickness is comparable in the presence and absence of the nanoparticle when the magnitude of thermal fluctuations is considered. By comparing the area compressibility moduli for different segments of the MD trajectory, we observe that the segment where AuNP is adsorbed on DPhPC consistently exhibits lower compressibility modulus relative to the segment without AuNP adsorption from multiple independent trajectories. This suggests that MPA-AuNP adsorption likely leads to local softening of the bilayer. Analysis of headgroup orientation and lipid tail order parameters (Fig. 11) indicates that AuNP binding perturbs mainly the headgroup orientation while having a minimal impact on the tails. The headgroups near the MPA-AuNP are better aligned with the membrane normal compared to those further away; this leads to overall more repulsion between the neighboring headgroups, weakening the adhesion between neighboring lipids, which in turn leads to larger area fluctuations and thus a lower area compressibility modulus. On the other hand, a quantitative characterization of the area compressibility remains challenging even with microsecond MD trajectories; the statistical uncertainty associated with the computed area compressibility is about 12%, which is comparable to the difference between cases with and without the AuNP bound to the membrane. The subtle effect of AuNP binding on the membrane mechanical properties is not unexpected, since the DPhPC bilayer is stiff and the interaction between AuNP and the zwitterionic headgroup is relatively weak.

## **2.4 Conclusions and Implications**

Model membranes provide useful platforms to gain quantitative insight into interactions with nanoparticles such binding, changes in lipid bilayer structure, and alterations to mechanical properties. While membrane modeling strategies are becoming increasingly sophisticated and

computational modeling approaches have begun to complement experimental results, most studies investigating interactions with nanomaterials have been limited to single-component or mixed phospholipid bilayers, with only relatively few reports of models that incorporate other relevant membrane biomolecules<sup>35,36</sup>. The combined experimental and computational strategy taken in the present study allowed us to investigate the influence of nanoparticles binding on membrane properties and *function*.

The mechanosensitivity of gramicidin A ion channels arises from the dependence of gA dimerization on bilayer compressibility, meaning that its ion channel formation and the lifetime of channels depends on the ability of surrounding phospholipids to deform<sup>103</sup>. Gramicidin A channels are smaller than the thickness of the phospholipid bilayer<sup>46,93,104</sup>. Thus, gA dimerization and channel formation depends on the ability of the bilayer to compress to match the hydrophobic length ( $l = 2.6$  nm)<sup>105</sup> of the channel (hydrophobic matching)<sup>46,66</sup>, a property important for larger ion channels<sup>92,106</sup> and other membrane proteins<sup>47</sup>.

Prior reports speculated that nanoparticles can indirectly alter ion channel function through interactions with the surrounding membrane<sup>39,42,107</sup>, but experimental support for this has been inconclusive. For example, the reduction in sodium channel current amplitudes in neuroendocrine cells induced by exposure to silver nanoparticles was proposed to be mediated by changes in membrane mechanical properties<sup>42</sup>. In another study, ZnO nanoparticles increased steady-state current amplitude, decreased the channel inactivation rate during steady-state depolarization, and had no effect on the current activation rate for HEK 239 cells. The mechanism was proposed to involve nanoparticle-induced alterations to channel gating (opening/closing) rather than channel blockage, but whether the effects observed were due to direct interaction of ZnO with the ion channel or indirect interactions with the lipid bilayer remained unresolved<sup>39</sup>. The inconclusiveness

of these studies reflects the challenges associated with measuring nanoparticle-induced alterations to the biophysical properties of the membranes of living cells.

Our results provide evidence that nanoparticles can indirectly disrupt the function of gA ion channels by altering mechanical properties of the surrounding lipid bilayer. Although similar results have not been reported for nanoparticles, several studies have investigated such effects using amphiphiles or drug molecules. For example, amphiphiles have been shown to change membrane properties such as compressibility and thickness, which alters channel function by modulating the energetic penalty for membrane deformation associated with the mismatch in hydrophobic thickness between the bilayer and embedded ion channel<sup>68,95,108</sup>. The dependence of gA channel activity on bilayer hydrophobic matching has also been exploited to study the impact of drug molecules on bilayer stiffness by using gA as a “molecular force probe” to assess changes in bilayer properties such as bilayer compressibility<sup>46,94</sup>. The partitioning into or adsorption onto the membrane of these drug molecules alters bilayer stiffness, and in turn the bilayer disjoining force ( $F_{\text{dis}}$ ) acting on gA channels, by changing the bilayer compression and bending moduli and intrinsic bilayer curvature<sup>46</sup>. A decrease in bilayer stiffness and therefore in  $F_{\text{dis}}$  results in increases in  $N(t)$  and  $\tau$ , and an increase in bilayer stiffness has the opposite effect.

In our study, the malonate molecule chosen as our ligand control induced a decrease in channel lifetime, while differences in channel activity were not statistically significant. In contrast, anionic TCOOH- and MPA-AuNPs interact with the model membrane system containing gA in a manner that reduces the number of ion channels and extends the lifetime of remaining channels without changing conductance. Thus, whereas the effects of amphiphiles, peptides, and solvents result in coordinated changes in  $N(t)$  and  $\tau$  (i.e., both properties change in the same direction), anionic AuNPs interacting with gA-containing bilayers cause  $N(t)$  and  $\tau$  to change in opposite

directions. This finding suggests more complex modulation of gA monomer–dimer kinetics in the case of interaction with anionic nanoparticles relative to partitioning or adsorption of molecular species. We note that the trends observed for small molecules may not extend to larger, flexible species like anionic polymers, which were previously reported to not exert an effect on gA <sup>109</sup>.

Complementary evidence from our experimental and computational experiments also indicate that anionic AuNPs do not induce measurable changes in gA dimer structure or conformation within the lipid bilayer. First, FTIR characterization of Amide I and II absorbances did not identify measurable changes that would indicate altered ion channel structure or conformation for gA-containing vesicles exposed to anionic AuNPs <sup>98,110,111</sup>. Our FTIR results are also similar to previously reported effects for changes in amide absorbance for gA-vesicles exposed to silver nanoparticles <sup>99</sup>. Furthermore, molecular dynamics simulations demonstrate that anionic TCOOH- and MPA-AuNPs do not interact strongly with gA ion channels or induce significant conformational changes to gA dimers. Rather, our computational results suggest that AuNP adsorption to the lipid bilayer surface induces local perturbation of the membrane and likely a concomitantly decreased compressibility modulus, which is consistent with the extended lifetimes of gA channels observed experimentally. Based on our combined results, we conclude that anionic AuNPs disrupt ion channel function by modulating local membrane properties rather than by direct NP-ion channel interactions.

Previous studies have reported that gA dimer configuration must stretch to a transition state before dissociating into monomers <sup>112,113</sup>. The thickness of the annular lipids is unable to match both dimer and the transition state, thus hydrophobic mismatch is expected to affect the dissociation rate of the dimer. Since DPhPC and gA dimers exhibit significant hydrophobic mismatch, the formation of a gA dimer induces local lipid compression, and the degree of

compression is less in the transition state. Decrease in compressibility modulus (thus bending modulus according to a polymer brush model for lipid mechanics) leads to a lower free energy penalty for lipid deformation and an increased barrier from dimer to the transition state <sup>114</sup>; the latter is consistent with the lifetime increase of the gA dimer observed experimentally. Similar effect on the gA dimer lifetime was reported for a series of amphiphiles by Andersen et al. <sup>95</sup>, who explained the increase of gA dimer lifetime in terms of reduced bilayer spring constant by the amphiphiles. Prior studies have reported that channel lifetimes and channel activity change in a concerted fashion with changes in bilayer mechanical properties. In contrast, anionic AuNPs induce changes in channel lifetime and activity that are inversely correlated, which to the best of our knowledge has not been previously described. Thus, the mechanisms of anionic AuNP modulation of gA ion channel activity cannot be described based solely on current understanding of the influence of membrane mechanics on channel activity. While further study will be required to understand the inverse correlation between lifetime and activity, our results point to the importance of developing more sophisticated modeling approaches to understand such effects.

Our combined experimental and computational results demonstrate that anionic AuNPs can indirectly alter gramicidin A ion channel function by changing local mechanical properties of the surrounding lipid bilayer. These findings also provide insight into the potential for nanoparticles to indirectly alter ion channel function in cells <sup>39,42,107</sup>. Due to the complexity of such systems, determination of underlying mechanisms of interaction can be difficult, and attribution of ion channel disruption by nanoparticles to changes in membrane properties has been largely speculative in those system. For example, a role for changes in membrane mechanical properties has been proposed for the impact of silver nanoparticles on sodium channel function <sup>42</sup>, and for the effect of ZnO nanoparticles on membrane potentials for HEK 239 cells <sup>39</sup>. However, these

studies could not distinguish between direct interactions with ion channels from indirect interactions with the surrounding lipid bilayer using available techniques<sup>39,42</sup>. While further investigation would be necessary to definitively correlate our results to biological outcomes, our combined approach establishes a connection between NP-induced modulation of membrane mechanical properties and impact on ion channel function and offers molecular-level insight into a possible underlying mechanism.

The ability of interactions with nanoparticles to impact the bilayer mechanical properties with concomitant effects on the hydrophobic matching of mechanosensitive ion channels have implications far beyond the present study. The activities of numerous membrane proteins are modulated by the coupling between hydrophobic protein domains and the bilayer core including those of ion channels, transporters, receptors, and enzymes<sup>47,106</sup>. Our results indicate that nanoparticle effects on protein function do not require direct interaction; effects may also be mediated by changes in the biophysical properties of the lipid bilayer. Such indirect effects warrant investigation in evaluating the safety of engineered nanomaterials and suggest potential applications in modulating cellular function.

## 2.5 Tables and Figures

**Table 1.** Diameters and Zeta-Potentials of Anionic Gold Nanoparticles

Ligand	Core Diameter <sup>a</sup> (nm)	Hydrodynamic Diameter <sup>b</sup> (nm)			$\zeta$ -potential <sup>b</sup> (mV)
		Number-Average	Z-Average	PDI	
MPA	5.4 ± 1.6	360 ± 61	480 ± 94	0.28 ± 0.03	-29.4 ± 0.99
TCOOH	2.1 ± 0.2	20 ± 15	500 ± 130	0.53 ± 0.08	-8.9 ± 0.40

<sup>a</sup> Core diameters represent mean values ± one standard deviation and are based on analysis of TEM images ( $n = 150-700$ ). PDI is the polydispersity index.

<sup>b</sup> Hydrodynamic diameters ( $n = 5$ ) and  $\zeta$ -potentials ( $n = 5$ ) were determined in 0.15 M KCl buffered to pH 7 with 0.01 M HEPES.

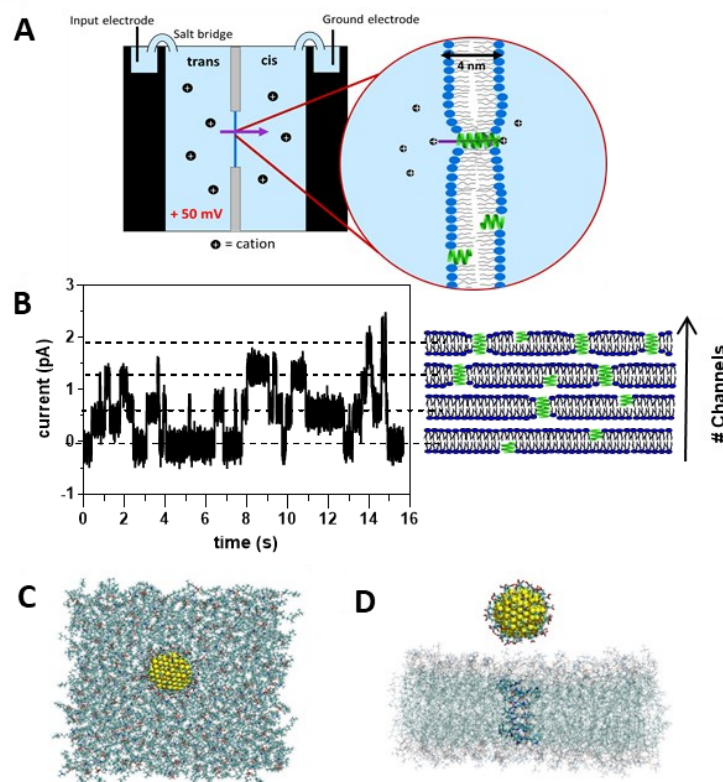


**Figure 1.** Primary experimental and computational approaches. (A) Schematic of the voltage-clamp electrophysiology setup used to study ion channels embedded in suspended bilayers. Cis and trans refer to sides of the membrane with respect to the position of the viewing window (i.e., from the vantage point of the user). (B) Electrical current trace for gramicidin A embedded in a DPhPC bilayer bathed in symmetric solutions of 0.15 M KCl buffered to pH 7 with 0.01 M HEPES. A +50 mV transmembrane potential was applied to the trans well such that cations flow to the cis well through open gramicidin A channels. Each current step on the electrophysiology traces of current versus time on the left corresponds to the number of conducting channels in the individual bilayers depicted in the right. (C, D) Illustration of the initial configuration of the molecular dynamics system after assembly. The system shown here includes an MPA-AuNP assembled with a gramicidin A dimer embedded in a DPhPC lipid bilayer. For clarity, water and ions are not shown, (C) provides top-down view (D) depicts a side view.

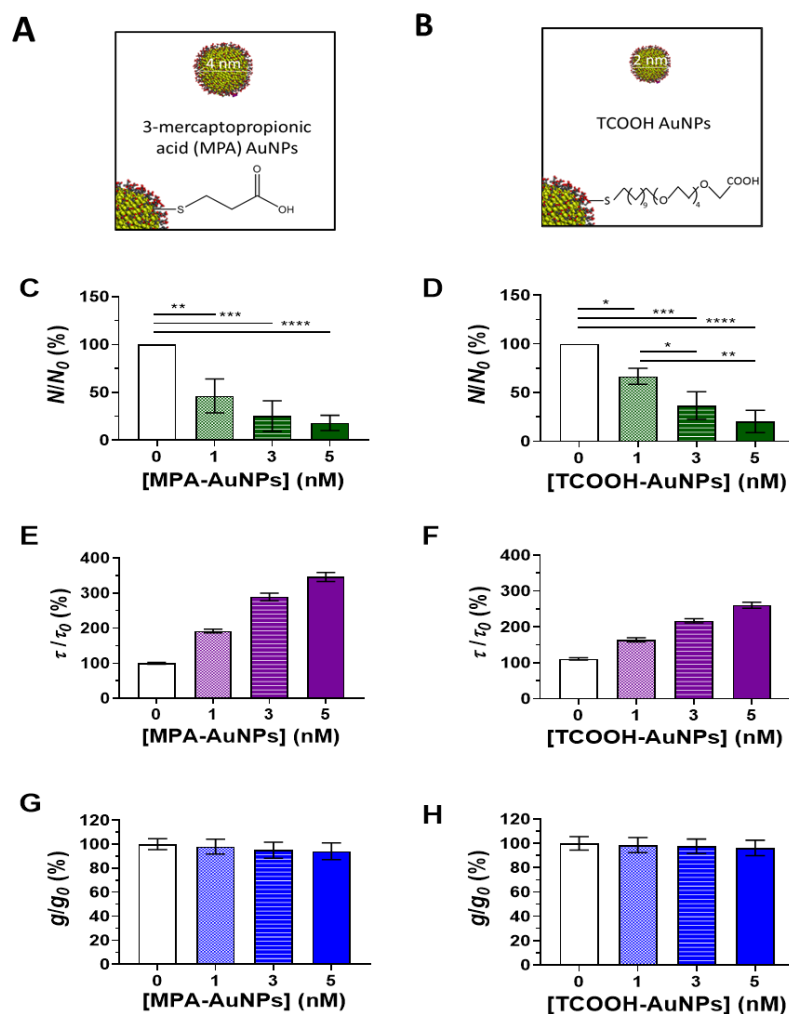


**Figure 2.** (A, B) Anionic gold nanoparticles (C, D) reduced normalized channel activity, (E, F) increased channel lifetimes ( $\tau$ ), and (G, H) had no effect on single-channel current at the nanoparticle concentrations used (1 – 5 nM, number concentration) of MPA- or TCOOH-AuNPs. Changes in normalized channel activity ( $N/N_0$ ), lifetime ( $\tau/\tau_0$ ), and single-channel current ( $g/g_0$ ) are shown for each nanoparticle type where the 0 subscript indicates the value prior to introduction of nanoparticles. Nanoparticles were added to both sides of the planar suspended bilayer lipid membrane with a +50 mV potential applied through the *trans* electrode. Channels were sampled in MPA- and TCOOH-AuNP experiments over 6.5 and 3.0 min, respectively. In (C) and (D), statistical significance is denoted by asterisks:  $p < 0.05$  (\*),  $p < 0.01$  (\*\*),  $p < 0.001$  (\*\*\*),  $p < 0.0001$  (\*\*\*\*). In (E) and (F), all differences are significant ( $p < 0.05$ ). The normalized single-channel currents in (G) and (H) do not differ ( $p > 0.05$ ). Plots display the results of triplicate experiments; error bars represent one standard deviation.

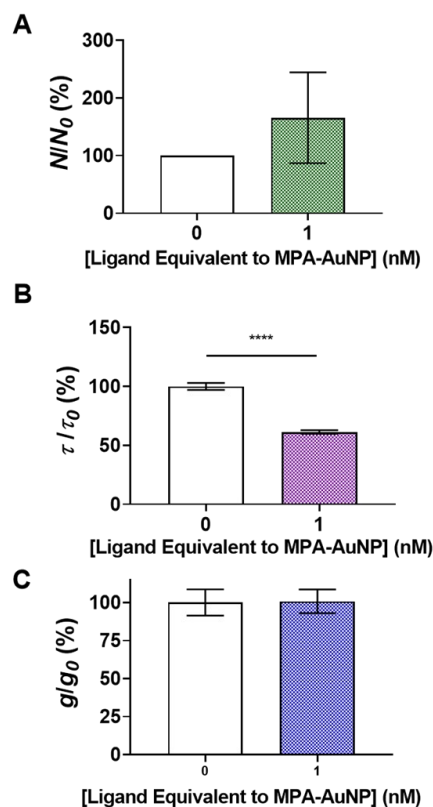


**Figure 3.** Malonate, used to probe the effects of the MPA ligand, produced (A) no changes in channel activity ( $N/N_0$ ), (B) reduced channel lifetime ( $\tau/\tau_0$ ), and (C) left single-channel current ( $g/g_0$ ) unaffected. Malonate was added to both sides of the suspended bilayer lipid membrane at a concentration equivalent to the amount of ligand present on 1 nM MPA-AuNPs with a +50 mV potential applied through the trans electrode. Plots display the results of triplicate experiments. Channels were sampled over 6.5 min. Statistical significance is designated by asterisks:  $p < 0.0001$  (\*\*\*\*).

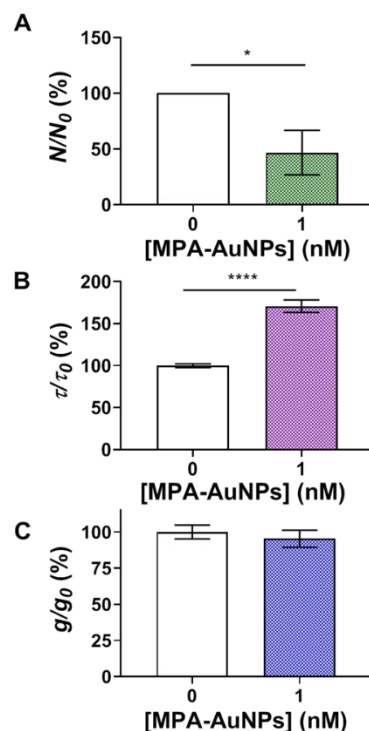


**Figure 4.** Anionic mercaptopropionic acid (MPA)-gold nanoparticles (1 nM), when added to only one side of the bilayer, (A) reduced normalized channel activity ( $N/N_0$ ), (B) increased normalized single-channel lifetimes ( $\tau/\tau_0$ ), and (C) had no effect on normalized single-channel current ( $g/g_0$ ). The subscripted 0 denotes the value prior to introduction of nanoparticles. Nanoparticles were added to the trans side of the planar suspended bilayer lipid membrane with a  $-50$  mV transmembrane potential applied through the cis electrode. Channels were sampled over 3.0 min. Statistical significance is denoted by asterisks:  $p < 0.05$  (\*),  $p < 0.001$  (\*\*\*). Plots display the results of triplicate experiments.

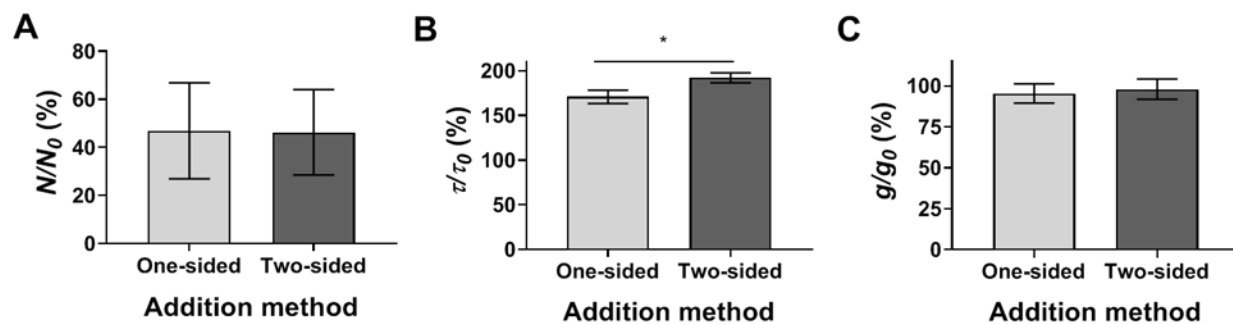


**Figure 5.** Comparison of changes in normalized (A) channel activities ( $N/N_0$ ), (B) single-channel lifetimes ( $\tau/\tau_0$ ), and (C) single-channel currents ( $g/g_0$ ) for experiments in which 1 nM MPA-AuNPs were added to either one or both sides of the planar suspended bilayer lipid membrane. Data are replotted from previous figures. Channels were sampled over 3.0 and 6.5 minutes for one- and two-sided exposures, respectively. Bars show mean values; error bars indicate one standard deviation. Statistical significance ( $p < 0.05$ , \*) is denoted.

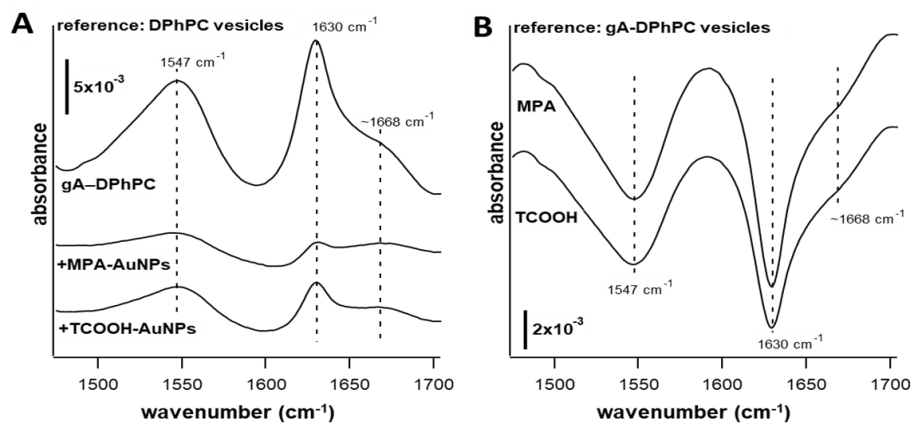


**Figure 6.** Amide I and II region in the infrared absorbance spectra of gA-containing DPhPC vesicles before and after exposure to 100 nM of the indicated nanoparticle. Spectra were referenced against (A) DPhPC vesicles lacking gA and (B) DPhPC vesicles containing gA. Abbreviations: DPhPC, 1,2-diphytanoyl-*sn*-glycero-3-phosphocholine; gA, gramicidin A; MPA, mercaptopropionic acid; TCOOH, mercaptodecanoic-tetraethyleneglycol-carboxylate

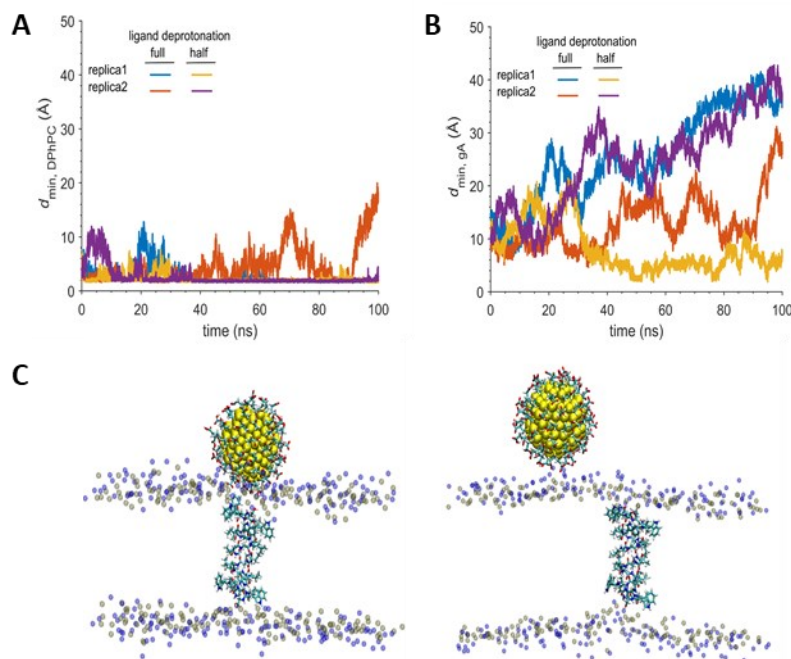


**Figure 7.** (A) Distance between MPA-AuNP and DPhPC bilayer over a 100 ns timeframe and (B) distance between MPA-AuNP and gA dimer embedded in a DPhPC bilayer; both two replicates each for half deprotonated and fully deprotonated MPA-AuNP. Panel (C) depicts snapshots from MD simulations illustrating that the MPA-AuNP interact directly with lipid molecules regardless whether it is near or far from the gA dimer. The snapshots are from simulations of the half-deprotonated MPA-AuNP (i.e., 35 out of 72 MPA ligands are charged) assembled with a gA dimer embedded in a DPhPC lipid bilayer. For clarity, water and ions are not shown, and only phosphorus (tan) and nitrogen (blue) atoms in phospholipid head groups are shown for lipids.

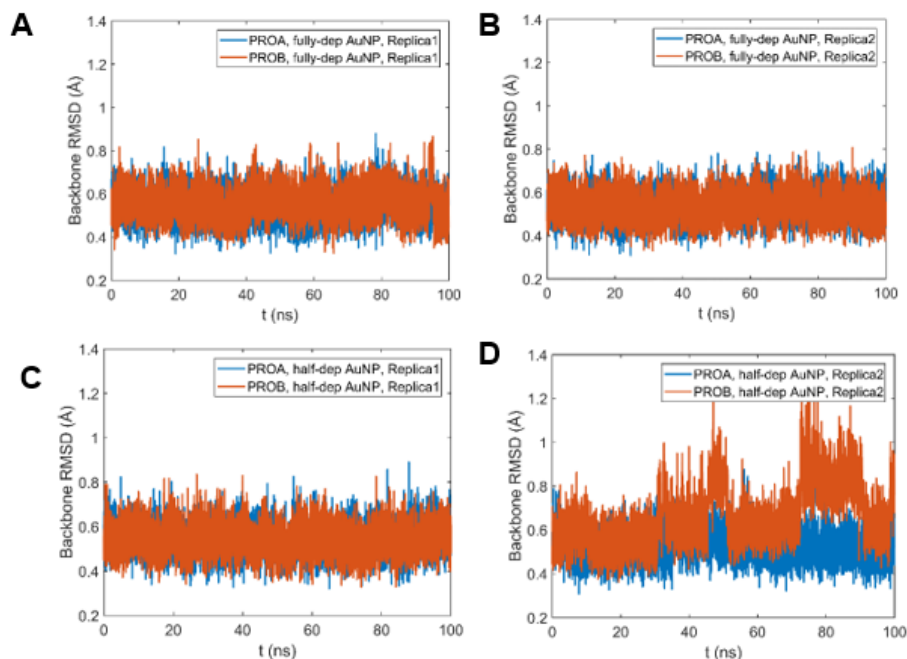


**Figure 8.** Time evolution of backbone RMSD of a gA dimer with respect to the crystal structure (PDB: 1JNO) from 100 ns MD simulations of a fully/half-deprotonated MPA-AuNP assembled with a gA dimer embedded in a DPhPC lipid bilayer. Panels *A* and *B* are for two independent replicas of the system with fully deprotonated MPA-AuNP (i.e., 72 deprotonated MPA ligands), and panels *C* and *D* are for two replicas of the system with half deprotonated MPA-AuNP (i.e., 35 out of 72 MPA ligands are deprotonated). In each panel, PROA and PROB represent the two gA monomers; MPA-AuNP is positioned on the side of PROB. In one trajectory depicted in panel *D*, the half deprotonated MPA-AuNP system has a higher backbone RMSD values in the range of 1.2 Å (vs. the typical values of 0.4 to 0.7 Å); however, no direct contact between MPA-AuNP and gA was observed for those segments of the trajectory, suggesting that the larger structural deviations were stochastic and not caused by interaction with the nanoparticle.

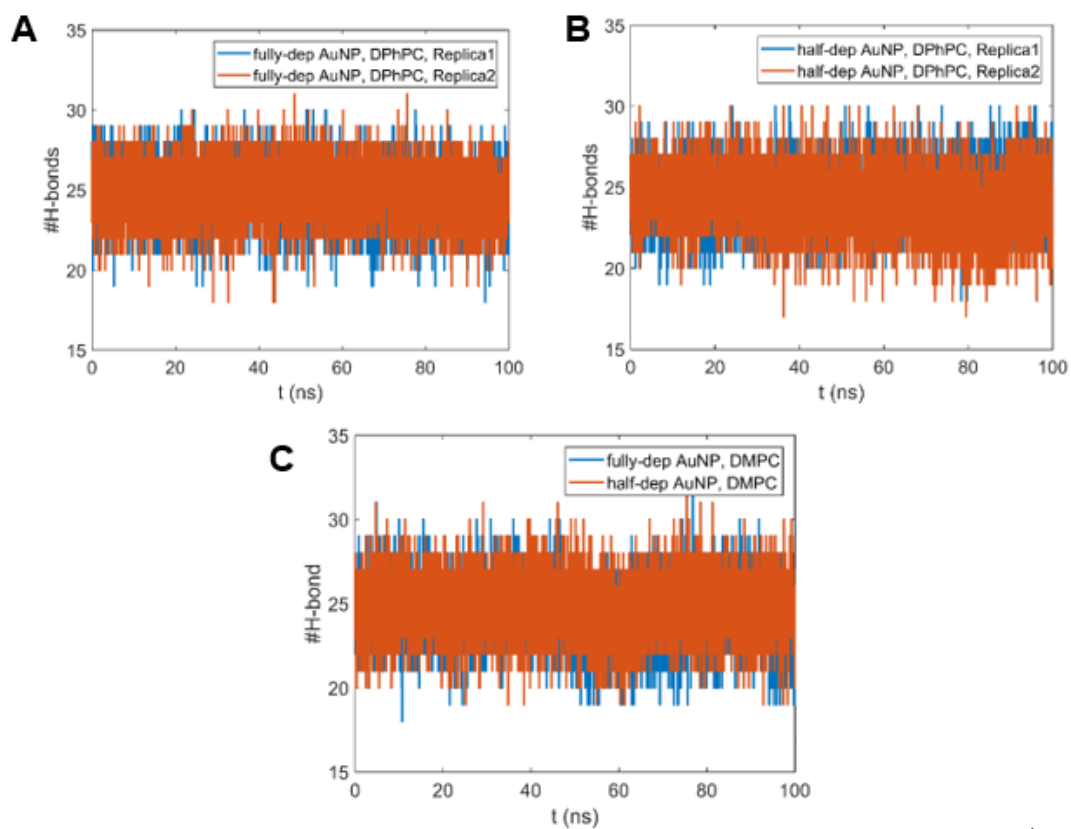


**Figure 9.** Time evolution of the total number of backbone hydrogen bonds formed within a gA dimer from 100 ns MD simulations of a fully/half-deprotonated MPA-AuNP assembled with a gA dimer embedded in a (A, B) DPhPC (two replicas of 100 ns trajectories shown in each panel) or (C) DMPC bilayer.

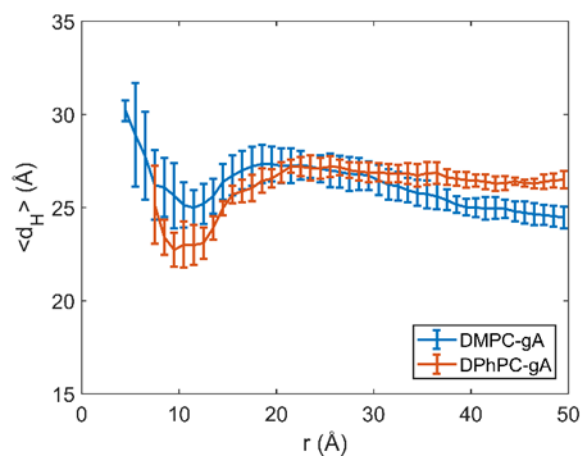


**Figure 10.** Hydrophobic thickness profile of PC lipids as a function of radial distance from the center of a gA dimer embedded in a DPhPC or DMPC lipid bilayer based on 100 ns of MD simulations without the nanoparticle. The hydrophobic thickness is defined as the average distance between the C2 carbon atoms of the lipid acyl tails.

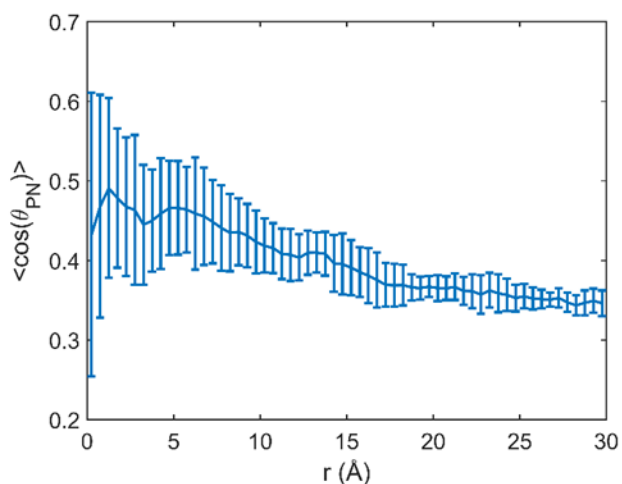


**Figure 11.** P–N vector orientation profile of DPhPC lipids as a function of projected radial distance between the center of mass of MPA-AuNP and choline nitrogen from 10 replicas of 100-ns MD simulations of a DPhPC bilayer assembled with one fully deprotonated MPA-AuNP.  $\theta_{PN}$  is defined as the angle between the phosphorus – nitrogen vector and the membrane normal. Only lipid molecules in the monolayer in contact with the MPA-AuNP are selected for analysis.

## 2.6 References

- (1) Tanzid, M.; Sobhani, A.; DeSantis, C. J.; Cui, Y.; Hogan, N. J.; Samaniego, A.; Veeraraghavan, A.; Halas, N. J. Imaging through Plasmonic Nanoparticles. *Proc. Natl. Acad. Sci. U. S. A.* **2016**, *113* (20), 5558–5563. <https://doi.org/10.1073/pnas.1603536113>.
- (2) Rastinehad, A. R.; Anastos, H.; Wajswol, E.; Winoker, J. S.; Sfakianos, J. P.; Doppalapudi, S. K.; Carrick, M. R.; Knauer, C. J.; Taouli, B.; Lewis, S. C.; Tewari, A. K.; Schwartz, J. A.; Canfield, S. E.; George, A. K.; West, J. L.; Halas, N. J. Gold Nanoshell-Localized Photothermal Ablation of Prostate Tumors in a Clinical Pilot Device Study. *Proc. Natl. Acad. Sci. U. S. A.* **2019**, *116* (37), 18590–18596. <https://doi.org/10.1073/pnas.1906929116>.
- (3) Murphy, E. A.; Majeti, B. K.; Barnes, L. A.; Makale, M.; Weis, S. M.; Lutu-Fuga, K.; Wrasidlo, W.; Cheresch, D. A. Nanoparticle-Mediated Drug Delivery to Tumor Vasculature Suppresses Metastasis. *Proc. Natl. Acad. Sci. U. S. A.* **2008**, *105* (27), 9343–9348. <https://doi.org/10.1073/pnas.0803728105>.
- (4) Rejman, J.; Oberle, V.; Zuhorn, I. S.; Hoekstra, D. Size-Dependent Internalization of Particles via the Pathways of Clathrin-and Caveolae-Mediated Endocytosis. *Biochem. J.* **2004**, *377* (1), 159–169. <https://doi.org/10.1042/BJ20031253>.
- (5) Jiang, W.; Kim, B. Y. S.; Rutka, J. T.; Chan, W. C. W. Nanoparticle-Mediated Cellular Response Is Size-Dependent. *Nat. Nanotechnol.* **2008**, *3* (3), 145–150. <https://doi.org/10.1038/nnano.2008.30>.
- (6) Dos Santos, T.; Varela, J.; Lynch, I.; Salvati, A.; Dawson, K. A. Quantitative Assessment of the Comparative Nanoparticle-Uptake Efficiency of a Range of Cell Lines. *Small* **2011**, *7* (23), 3341–3349. <https://doi.org/10.1002/sml.201101076>.
- (7) Cho, E. C.; Xie, J.; Wurm, P. A.; Xia, Y. Understanding the Role of Surface Charges in Cellular Adsorption versus Internalization by Selectively Removing Gold Nanoparticles on the Cell Surface with a I 2/KI Etchant. *Nano Lett.* **2009**, *9* (3), 1080–1084. <https://doi.org/10.1021/nl803487r>.
- (8) Shapero, K.; Fenaroli, F.; Lynch, I.; Cottell, D. C.; Salvati, A.; Dawson, K. A. Time and Space Resolved Uptake Study of Silica Nanoparticles by Human Cells. *Mol. Biosyst.* **2011**, *7* (2), 371–378. <https://doi.org/10.1039/c0mb00109k>.
- (9) Lesniak, A.; Salvati, A.; Santos-Martinez, M. J.; Radomski, M. W.; Dawson, K. A.; Åberg, C. Nanoparticle Adhesion to the Cell Membrane and Its Effect on Nanoparticle Uptake Efficiency. *J. Am. Chem. Soc.* **2013**, *135* (4), 1438–1444. <https://doi.org/10.1021/ja309812z>.
- (10) Feng, Z. V.; Gunsolus, I. L.; Qiu, T. A.; Hurley, K. R.; Nyberg, L. H.; Frew, H.; Johnson, K. P.; Vartanian, A. M.; Jacob, L. M.; Lohse, S. E.; Torelli, M. D.; Hamers, R. J.; Murphy, C. J.; Haynes, C. L. Impacts of Gold Nanoparticle Charge and Ligand Type on Surface Binding and Toxicity to Gram-Negative and Gram-Positive Bacteria. *Chem. Sci.* **2015**, *6* (9), 5186–5196. <https://doi.org/10.1039/c5sc00792e>.
- (11) Nazemidashtarjandi, S.; Farnoud, A. M. Membrane Outer Leaflet Is the Primary Regulator of Membrane Damage Induced by Silica Nanoparticles in Vesicles and Erythrocytes.

*Environ. Sci. Nano* **2019**, *6* (4), 1219–1232. <https://doi.org/10.1039/c8en01267a>.

(12) Chen, J.; Hessler, J. A.; Putchakayala, K.; Panama, B. K.; Khan, D. P.; Hong, S.; Mullen, D. G.; DiMaggio, S. C.; Som, A.; Tew, G. N.; Lopatin, A. N.; Baker, J. R.; Holl, M. M. B.; Orr, B. G. Cationic Nanoparticles Induce Nanoscale Disruption in Living Cell Plasma Membranes. *J. Phys. Chem. B* **2009**, *113* (32), 11179–11185. <https://doi.org/10.1021/jp9033936>.

(13) Zhu, W.; Von Dem Busschec, A.; Xin, Y.; Qiu, Y.; Wang, Z.; Weston, P.; Hurt, R. H.; Kane, A. B.; Gao, H. Nanomechanical Mechanism for Lipid Bilayer Damage Induced by Carbon Nanotubes Confined in Intracellular Vesicles. *Proc. Natl. Acad. Sci. U. S. A.* **2016**, *113* (44), 12374–12379. <https://doi.org/10.1073/pnas.1605030113>.

(14) Warren, E. A. K.; Payne, C. K. Cellular Binding of Nanoparticles Disrupts the Membrane Potential. *RSC Adv.* **2015**, *5* (18), 13660–13666. <https://doi.org/10.1039/c4ra15727c>.

(15) Dante, S.; Petrelli, A.; Petrini, E. M.; Marotta, R.; Maccione, A.; Alabastri, A.; Quarta, A.; De Donato, F.; Ravasenga, T.; Sathya, A.; Cingolani, R.; Proietti Zaccaria, R.; Berdondini, L.; Barberis, A.; Pellegrino, T. Selective Targeting of Neurons with Inorganic Nanoparticles: Revealing the Crucial Role of Nanoparticle Surface Charge. *ACS Nano* **2017**, *11* (7), 6630–6640. <https://doi.org/10.1021/acsnano.7b00397>.

(16) Hussain, S.; Garantziotis, S.; Rodrigues-Lima, F.; Dupret, J.; Baeza-Squiban, A.; Boland, S. Intracellular Signal Modulation by Nanomaterials. In *Nanomaterial Impacts on Cell Biology and Medicine*; 2014; pp 111–134.

(17) Williams, D. N.; Pramanik, S.; Brown, R. P.; Zhi, B.; McIntire, E.; Hudson-Smith, N. V.; Haynes, C. L.; Rosenzweig, Z. Adverse Interactions of Luminescent Semiconductor Quantum Dots with Liposomes and *Shewanella Oneidensis*. *ACS Appl. Nano Mater.* **2018**, *1* (9), 4788–4800. <https://doi.org/10.1021/acsanm.8b01000>.

(18) Moghadam, B. Y.; Hou, W.-C.; Corredor, C.; Westerhoff, P.; Posner, J. D. The Role of Nanoparticle Surface Functionality in the Disruption of Model Cell Membranes. *Langmuir* **2012**, *28* (47), 16318–16326. <https://doi.org/10.1038/jid.2014.371>.

(19) Wang, B.; Zhang, L.; Sung, C. B.; Granick, S. Nanoparticle-Induced Surface Reconstruction of Phospholipid Membranes. *Proc. Natl. Acad. Sci. U. S. A.* **2008**, *105* (47), 18171–18175. <https://doi.org/10.1073/pnas.0807296105>.

(20) Laurencin, M.; Georgelin, T.; Malezieux, B.; Siaugue, J. M.; Ménager, C. Interactions between Giant Unilamellar Vesicles and Charged Core-Shell Magnetic Nanoparticles. *Langmuir* **2010**, *26* (20), 16025–16030. <https://doi.org/10.1021/la1023746>.

(21) Bailey, C. M.; Kamaloo, E.; Waterman, K. L.; Wang, K. F.; Nagarajan, R.; Camesano, T. A. Size Dependence of Gold Nanoparticle Interactions with a Supported Lipid Bilayer: A QCM-D Study. *Biophys. Chem.* **2015**, *203–204*, 51–61. <https://doi.org/10.1016/j.bpc.2015.05.006>.

(22) Mensch, A. C.; Buchman, J. T.; Haynes, C. L.; Pedersen, J. A.; Hamers, R. J. Quaternary Amine-Terminated Quantum Dots Induce Structural Changes to Supported Lipid Bilayers. *Langmuir* **2018**, *34* (41), 12369–12378. <https://doi.org/10.1021/acs.langmuir.8b02047>.

(23) Troiano, J. M.; Olenick, L. L.; Kuech, T. R.; Melby, E. S.; Hu, D.; Lohse, S. E.; Mensch, A. C.; Dogangun, M.; Vartanian, A. M.; Torelli, M. D.; Ehimighe, E.; Walter, S. R.; Fu, L.;

- Anderton, C. R.; Zhu, Z.; Wang, H.; Orr, G.; Murphy, C. J.; Hamers, R. J.; Pedersen, J. A.; Geiger, F. M. Direct Probes of 4 Nm Diameter Gold Nanoparticles Interacting with Supported Lipid Bilayers. *J. Phys. Chem. C* **2015**, *119* (1), 534–546. <https://doi.org/10.1021/jp512107z>.
- (24) Leroueil, P. R.; Berry, S. A.; Duthie, K.; Han, G.; Rotello, V. M.; McNerny, D. Q.; Baker, J. R.; Orr, B. G.; Holl, M. M. B. Wide Varieties of Cationic Nanoparticles Induce Defects in Supported Lipid Bilayers. *Nano Lett.* **2008**, *8* (2), 420–424. <https://doi.org/10.1021/nl0722929>.
- (25) Harishchandra, R. K.; Saleem, M.; Galla, H.-J. Nanoparticle Interaction with Model Lung Surfactant Monolayers. *J. R. Soc. Interface* **2009**, *7* (S1), S15–S26.
- (26) Bothun, G. D.; Ganji, N.; Khan, I. A.; Xi, A.; Bobba, C. Anionic and Cationic Silver Nanoparticle Binding Restructures Net-Anionic PC/PG Monolayers with Saturated or Unsaturated Lipids. *Langmuir* **2017**, *33* (1), 353–360. <https://doi.org/10.1021/acs.langmuir.6b02003>.
- (27) Carney, R. P.; Astier, Y.; Carney, T. M.; Voitchovsky, K.; Jacob Silva, P. H.; Stellacci, F. Electrical Method to Quantify Nanoparticle Interaction with Lipid Bilayers. *ACS Nano* **2013**, *7* (2), 932–942. <https://doi.org/10.1021/nn3036304>.
- (28) Mensch, A. C.; Hernandez, R. T.; Kuether, J. E.; Torelli, M. D.; Feng, Z. V.; Hamers, R. J.; Pedersen, J. A. Natural Organic Matter Concentration Impacts the Interaction of Functionalized Diamond Nanoparticles with Model and Actual Bacterial Membranes. *Environ. Sci. Technol.* **2017**, *51* (19), 11075–11084. <https://doi.org/10.1021/acs.est.7b02823>.
- (29) Goodman, C. M.; McCusker, C. D.; Yilmaz, T.; Rotello, V. M. Toxicity of Gold Nanoparticles Functionalized with Cationic and Anionic Side Chains. *Bioconjug. Chem.* **2004**, *15* (4), 897–900. <https://doi.org/10.1021/bc049951i>.
- (30) Gao, J.; Zhang, O.; Ren, J.; Wu, C.; Zhao, Y. Aromaticity/Bulkiness of Surface Ligands to Promote the Interaction of Anionic Amphiphilic Gold Nanoparticles with Lipid Bilayers. *Langmuir* **2016**, *32* (6), 1601–1610. <https://doi.org/10.1021/acs.langmuir.6b00035>.
- (31) Van Lehn, R. C.; Ricci, M.; Silva, P. H. J.; Andreozzi, P.; Reguera, J.; Voitchovsky, K.; Stellacci, F.; Alexander-Katz, A. Lipid Tail Protrusions Mediate the Insertion of Nanoparticles into Model Cell Membranes. *Nat. Commun.* **2014**, *5*. <https://doi.org/10.1038/ncomms5482>.
- (32) Das, M.; Dahal, U.; Mesele, O.; Liang, D.; Cui, Q. Molecular Dynamics Simulation of Interaction between Functionalized Nanoparticles with Lipid Membranes: Analysis of Coarse-Grained Models. *J. Phys. Chem. B* **2019**, *123* (49), 10547–10561. <https://doi.org/10.1021/acs.jpcc.9b08259>.
- (33) Li, Y.; Yuan, H.; Von Dem Bussche, A.; Creighton, M.; Hurt, R. H.; Kane, A. B.; Gao, H. Graphene Microsheets Enter Cells through Spontaneous Membrane Penetration at Edge Asperities and Corner Sites. *Proc. Natl. Acad. Sci. U. S. A.* **2013**, *110* (30), 12295–12300. <https://doi.org/10.1073/pnas.1222276110>.
- (34) Salis, B.; Pugliese, G.; Pellegrino, T.; Diaspro, A.; Dante, S. Polymer Coating and Lipid Phases Regulate Semiconductor Nanorods' Interaction with Neuronal Membranes: A Modeling Approach. *ACS Chem. Neurosci.* **2019**, *10* (1), 618–627. <https://doi.org/10.1021/acchemneuro.8b00466>.

- (35) Jacobson, K. H.; Gunsolus, I. L.; Kuech, T. R.; Troiano, J. M.; Melby, E. S.; Lohse, S. E.; Hu, D.; Chrisler, W. B.; Murphy, C. J.; Orr, G.; Geiger, F. M.; Haynes, C. L.; Pedersen, J. A. Lipopolysaccharide Density and Structure Govern the Extent and Distance of Nanoparticle Interaction with Actual and Model Bacterial Outer Membranes. *Environ. Sci. Technol.* **2015**, *49* (17), 10642–10650. <https://doi.org/10.1021/acs.est.5b01841>.
- (36) S. Melby, E.; Allen, C.; U. Foreman-Ortiz, I.; R. Caudill, E.; R. Kuech, T.; M. Vartanian, A.; Zhang, X.; J. Murphy, C.; Hernandez, R.; A. Pedersen, J. Peripheral Membrane Proteins Facilitate Nanoparticle Binding at Lipid Bilayer Interfaces. *Langmuir* **2018**, *34* (36), 10793–10805. <https://doi.org/10.1021/acs.langmuir.8b02060>.
- (37) Buchman, J. T.; Rahnamoun, A.; Landy, K. M.; Zhang, X.; Vartanian, A. M.; Jacob, L. M.; Murphy, C. J.; Hernandez, R.; Haynes, C. L. Using an Environmentally-Relevant Panel of Gram-Negative Bacteria to Assess the Toxicity of Polyallylamine Hydrochloride-Wrapped Gold Nanoparticles. *Environ. Sci. Nano* **2018**, *5* (2), 279–288. <https://doi.org/10.1039/c7en00832e>.
- (38) Gadsby, D. C. Ion Channels versus Ion Pumps: The Principal Difference, in Principle. *Nat. Rev. Mol. Cell Biol.* **2009**, *10* (5), 344–352. <https://doi.org/10.1038/nrm2668>.
- (39) Piscopo, S.; Brown, E. R. Zinc Oxide Nanoparticles and Voltage-Gated Human Kv11.1 Potassium Channels Interact through a Novel Mechanism. *Small* **2018**, *14* (15), 1–11. <https://doi.org/10.1002/sml.201703403>.
- (40) Leifert, A.; Pan, Y.; Kinkeldey, A.; Schiefer, F.; Setzler, J.; Scheel, O.; Lichtenbeld, H.; Schmid, G.; Wenzel, W.; Jahnen-Dechent, W.; Simon, U. Differential HERG Ion Channel Activity of Ultrasmall Gold Nanoparticles. *Proc. Natl. Acad. Sci. U. S. A.* **2013**, *110* (20), 8004–8009. <https://doi.org/10.1073/pnas.1220143110>.
- (41) Monticelli, L.; Barnoud, J.; Orłowski, A.; Vattulainen, I. Interaction of C 70 Fullerene with the Kv1.2 Potassium Channel. *Phys. Chem. Chem. Phys.* **2012**, *14* (36), 12526–12533. <https://doi.org/10.1039/c2cp41117b>.
- (42) Busse, M.; Kraegeloh, A.; Stevens, D.; Cavelius, C.; Rettig, J.; Arzt, E.; Strauss, D. J. Modeling the Effects of Nanoparticles on Neuronal Cells: From Ionic Channels to Network Dynamics. *2010 Annu. Int. Conf. IEEE Eng. Med. Biol. Soc. EMBC'10* **2010**, 3816–3819. <https://doi.org/10.1109/IEMBS.2010.5627595>.
- (43) Calvaresi, M.; Furini, S.; Domene, C.; Bottoni, A.; Zerbetto, F. Blocking the Passage: C60 Geometrically Clogs K<sup>+</sup> Channels. *ACS Nano* **2015**, *9* (5), 4827–4834. <https://doi.org/10.1021/nn506164s>.
- (44) Gu, Z.; Plant, L. D.; Meng, X. Y.; Perez-Aguilar, J. M.; Wang, Z.; Dong, M.; Logothetis, D. E.; Zhou, R. Exploring the Nanotoxicology of MoS<sub>2</sub>: A Study on the Interaction of MoS<sub>2</sub> Nanoflakes and K<sup>+</sup> Channels. *ACS Nano* **2018**, *12* (1), 705–717. <https://doi.org/10.1021/acsnano.7b07871>.
- (45) Kraszewski, S.; Tarek, M.; Treptow, W.; Ramseyer, C. Affinity of C60 Neat Fullerenes with Membrane Proteins: A Computational Study on Potassium Channels. *ACS Nano* **2010**, *4* (7), 4158–4164. <https://doi.org/10.1021/nn100723r>.
- (46) Lundbaek, J. A.; Collingwood, S. A.; Ingólfsson, H. I.; Kapoor, R.; Andersen, O. S. Lipid

Bilayer Regulation of Membrane Protein Function: Gramicidin Channels as Molecular Force Probes. *J. R. Soc. Interface* **2010**, *7* (44), 373–395. <https://doi.org/10.1098/rsif.2009.0443>.

(47) Brown, M. F. Soft Matter in Lipid – Protein Interactions. *Annu. Rev. Biophys.* **2017**, *46*, 379–410.

(48) Miranda, O. R.; Chen, H. T.; You, C. C.; Mortenson, D. E.; Yang, X. C.; Bunz, U. H. F.; Rotello, V. M. Enzyme-Amplified Array Sensing of Proteins in Solution and in Biofluids. *J. Am. Chem. Soc.* **2010**, *132* (14), 5285–5289. <https://doi.org/10.1021/ja1006756>.

(49) Kanaras, A. G.; Kamounah, F. S.; Schaumburg, K.; Kiely, C. J.; Brust, M. Thioalkylated Tetraethylene Glycol: A New Ligand for Water Soluble Monolayer Protected Gold Clusters. *Chem. Commun. (Camb)*. **2002**, No. 20, 2294–2295. <https://doi.org/10.1039/b207838b>.

(50) Brust, M.; Walker, M.; Bethell, D.; Schiffrin, D. J.; Whyman, R. Synthesis of Thiol-Derivatised Gold Nanoparticles in a Two-Phase Liquid–Liquid System. *J. Chem. Soc., Chem. Commun.* **1994**, *0* (7), 801–802. <https://doi.org/10.1039/C39940000801>.

(51) Jiang, Y.; Huo, S.; Mizuhara, T.; Das, R.; Lee, Y.; Hou, S.; Moyano, D. F.; Duncan, B.; Liang, X.; Rotello, V. M. The Interplay of Size and Surface Functionality on the Cellular Uptake. *ACS Nano* **2015**, *9* (10), 9986–9993. <https://doi.org/10.1021/acsnano.5b03521>.

(52) Bozich, J. S.; Lohse, S. E.; Torelli, M. D.; Murphy, C. J.; Hamers, R. J.; Klaper, R. D. Surface Chemistry, Charge and Ligand Type Impact the Toxicity of Gold Nanoparticles to *Daphnia Magna*. *Environ. Sci. Nano* **2014**, *1* (3), 260–270. <https://doi.org/10.1039/C4EN00006D>.

(53) Lohse, S. E.; Eller, J. R.; Sivapalan, S. T.; Plews, M. R.; Murphy, C. J. A Simple Millifluidic Benchtop Reactor System for the High-Throughput Synthesis and Functionalization of Gold Nanoparticles with Different Sizes and Shapes. *ACS Nano* **2013**, *7* (5), 4135–4150. <https://doi.org/10.1021/nn4005022>.

(54) Haiss, W.; Thanh, N. T. K.; Aveyard, J.; Fernig, D. G. Determination of Size and Concentration of Gold Nanoparticles from UV-Vis Spectra. *Anal. Chem.* **2007**, *79* (11), 4215–4221. <https://doi.org/10.1021/ac0702084>.

(55) Torelli, M. D.; Putans, R. A.; Tan, Y.; Lohse, S. E.; Murphy, C. J.; Hamers, R. J. Quantitative Determination of Ligand Densities on Nanomaterials by X-Ray Photoelectron Spectroscopy. *ACS Appl. Mater. Interfaces* **2015**, *7* (3), 1720–1725. <https://doi.org/10.1021/am507300x>.

(56) Montal, M.; Mueller, P. Formation of Bimolecular Membranes from Lipid Monolayers and a Study of Their Electrical Properties. *Proc. Natl. Acad. Sci. U. S. A.* **1972**, *69* (12), 3561–3566. <https://doi.org/10.1073/pnas.69.12.3561>.

(57) Baba, T.; Toshima, Y.; Minamikawa, H.; Hato, M.; Suzuki, K.; Namo, N. Formation and Characterization of Planar Lipid Bilayer Membranes from Synthetic Phytanyl-Chained Glycolipids. *Biochim. Biophys. Acta - Biomembr.* **1999**, *1421* (1), 91–102.

(58) Ries, R. S.; Choi, H.; Blunck, R.; Bezanilla, F.; Heath, J. R. Black Lipid Membranes: Visualizing the Structure, Dynamics, and Substrate Dependence of Membranes. *J. Phys. Chem. B* **2004**, *108* (41), 16040–16049. <https://doi.org/10.1021/jp048098h>.

- (59) Zakharian, E. Ion Channels. **2013**, *998* (mV), 1–9. <https://doi.org/10.1007/978-1-62703-351-0>.
- (60) Ingolfsson, H. I.; Koeppe, R. E.; Andersen, O. S. Curcumin Is a Modulator of Bilayer Material Properties. *Biochemistry* **2007**, *46* (36), 10384–10391. <https://doi.org/10.1021/bi701013n>.
- (61) Hill, R. J. Electrokinetics of Nanoparticle Gel-Electrophoresis. *Soft Matter* **2016**, *12* (38), 8030–8048. <https://doi.org/10.1039/C6SM01685E>.
- (62) Liu, Y. W.; Pennathur, S.; Meinhart, C. D. Electrophoretic Mobility of a Spherical Nanoparticle in a Nanochannel. *Phys. Fluids* **2014**, *26* (11). <https://doi.org/10.1063/1.4901330>.
- (63) Sandblom, J.; Eisenman, G.; Neher, E. Ionic Selectivity, Saturation and Block in Gramicidin A Channels: II. Saturation Behavior of Single Channel Conductances and Evidence for Existence of Multiple Binding Sites in the Channel. *J. Membr. Biol.* **2013**, *31* (1), 383–417. <https://doi.org/10.1007/BF01869414>.
- (64) Lee, H.; Kim, S. M.; Jeon, T. J. Effects of Imidazolium-Based Ionic Liquids on the Stability and Dynamics of Gramicidin A and Lipid Bilayers at Different Salt Concentrations. *J. Mol. Graph. Model.* **2015**, *61*, 53–60. <https://doi.org/10.1016/j.jmgm.2015.06.016>.
- (65) Lundbæk, J. A.; Andersen, O. S. Spring Constants for Channel-Induced Lipid Bilayer Deformations: Estimates Using Gramicidin Channels. *Biophys. J.* **1999**, *76* (2), 889–895. [https://doi.org/10.1016/S0006-3495\(99\)77252-8](https://doi.org/10.1016/S0006-3495(99)77252-8).
- (66) Lundbæk, J. A.; Birn, P.; Girshman, J.; Hansen, A. J.; Andersen, O. S. Membrane Stiffness and Channel Function. *Biochemistry* **1996**, *35* (12), 3825–3830. <https://doi.org/10.1021/bi952250b>.
- (67) Sturges, H. A. The Choice of a Class Interval. *J. Am. Stat. Assoc.* **1926**, *21* (153), 65–66.
- (68) Lundbaek, J. A.; Birn, P.; Tape, S. E.; Toombes, G. E. S.; Søgaard, R.; Koeppe, R. E.; Gruner, S. M.; Hansen, A. J.; Andersen, O. S. Capsaicin Regulates Voltage-Dependent Sodium Channels by Altering Lipid Bilayer Elasticity. *Mol. Pharmacol.* **2005**, *68* (3), 680–689. <https://doi.org/10.1124/mol.105.013573>.
- (69) Hall, P.; Selinger, B. Better Estimates of Exponential Decay Parameters. *J. Phys. Chem.* **1981**, *85* (20), 2941–2946. <https://doi.org/10.1021/j150620a019>.
- (70) Townsley, L. E.; Tucker, W. A.; Sham, S.; Hinton, J. F. Structures of Gramicidins A, B, and C Incorporated into Sodium Dodecyl Sulfate Micelles. *Biochem.* **2001**, *40* (39), 11676–11686.
- (71) MacKerell, A. D.; Bashford, D.; Bellott, M.; Dunbrack, R. L.; Evanseck, J. D.; Field, M. J.; Fischer, S.; Gao, J.; Guo, H.; S. Ha et al. All-Atom Empirical Potential for Molecular Modeling and Dynamics Studies of Proteins. *J. Phys. Chem. B* **1998**, *102* (18), 3586–3616.
- (72) Huang, J.; A. D. MacKerell Jr. CHARMM36 All-Atom Additive Protein Force Field: Validation Based on Comparison to NMR Data. *J. Comput. Chem.* **2013**, *34* (25), 2135–2145. <https://doi.org/10.1002/jcc.23354>.

- (73) Klauda, J. B.; Venable, R. M.; Freites, J. A.; O'Connor, J. W.; Tobias, D. J.; Mondragon-Ramirez, C.; Vorobyov, I.; MacKerell Jr, A. D.; Pastor, R. W. Update of the CHARMM All-Atom Additive Force Field for Lipids: Validation on Six Lipid Types. *J. Phys. Chem. B* **2010**, *114* (23), 7830–7843.
- (74) Lim, J. B.; Klauda, J. B. Lipid Chain Branching at the Iso-and Anteiso-Positions in Complex Chlamydia Membranes: A Molecular Dynamics Study. *Biochim. Biophys. Acta-Biomembranes* **2011**, *1808* (1), 323–331.
- (75) Jo, S.; Kim, T.; Iyer, V. G.; Im, W. CHARMM-GUI: A Web-Based Graphical User Interface for CHARMM. *J. Comput. Chem.* **2008**, *29* (11), 1859–1865.
- (76) Lee, J.; Cheng, X.; Swails, J. M.; Yeom, M. S.; Eastman, P. K.; Lemkul, J. A.; Wei, S.; Buckner, J.; Jeong, J. C.; Qi, Y.; others. CHARMM-GUI Input Generator for NAMD, GROMACS, AMBER, OpenMM, and CHARMM/OpenMM Simulations Using the CHARMM36 Additive Force Field. *J. Chem. Theory Comput.* **2015**, *12* (1), 405–413.
- (77) Wu, E. L.; Cheng, X.; Jo, S.; Rui, H.; Song, K. C.; Dávila-Contreras, E. M.; Qi, Y.; Lee, J.; Monje-Galvan, V.; Venable, R. M.; others. CHARMM-GUI Membrane Builder toward Realistic Biological Membrane Simulations. *J. Comput. Chem.* **2014**, *35* (27), 1997–2004.
- (78) Darden, T.; York, D.; Pedersen, L. Particle Mesh Ewald: An  $N \cdot \log(N)$  Method for Ewald Sums in Large Systems. *J. Chem. Phys.* **1993**, *98* (12), 10089–10092.
- (79) Hong, J.; Hamers, R. J.; Pedersen, J. A.; Cui, Q. A Hybrid Molecular Dynamics/Multiconformer Continuum Electrostatics (MD/MCCE) Approach for the Determination of Surface Charge of Nanomaterials. *J. Phys. Chem. C* **2017**, *121* (6), 3584–3596.
- (80) Heinz, H.; Lin, T.-J.; Kishore Mishra, R.; Emami, F. S. Thermodynamically Consistent Force Fields for the Assembly of Inorganic, Organic, and Biological Nanostructures: The INTERFACE Force Field. *Langmuir* **2013**, *29* (6), 1754–1765.
- (81) Liang, D.; Hong, J.; Fang, D.; Bennett, J. W.; Mason, S. E.; Hamers, R. J.; Cui, Q. Analysis of the Conformational Properties of Amine Ligands at the Gold/Water Interface with QM, MM and QM/MM Simulations. *Phys. Chem. Chem. Phys.* **2018**, *20* (5), 3349–3362.
- (82) Phillips, J. C.; Braun, R.; Wang, W.; Gumbart, J.; Tajkhorshid, E.; Villa, E.; Chipot, C.; Skeel, R. D.; Kale, L.; Schulten, K. Scalable Molecular Dynamics with NAMD. *J. Comput. Chem.* **2005**, *26* (16), 1781–1802.
- (83) Ryckaert, J.-P.; Ciccotti, G.; Berendsen, H. J. C. Numerical Integration of the Cartesian Equations of Motion of a System with Constraints: Molecular Dynamics of n-Alkanes. *J. Comput. Phys.* **1977**, *23* (3), 327–341.
- (84) Feller, S. E.; Zhang, Y.; Pastor, R. W.; Brooks, B. R. Constant Pressure Molecular Dynamics Simulation: The Langevin Piston Method. *J. Chem. Phys.* **1995**, *103* (11), 4613–4621.
- (85) Martyna, G. J.; Tobias, D. J.; Klein, M. L. Constant Pressure Molecular Dynamics Algorithms. *J. Chem. Phys.* **1994**, *101* (5), 4177–4189.
- (86) Brooks, B. R.; Brooks III, C. L.; Mackerell Jr, A. D.; Nilsson, L.; Petrella, R. J.; Roux, B.; Won, Y.; Archontis, G.; Bartels, C.; Boresch, S.; others. CHARMM: The Biomolecular

Simulation Program. *J. Comput. Chem.* **2009**, *30* (10), 1545–1614.

- (87) Humphrey, W.; Dalke, A.; Schulten, K. VMD: Visual Molecular Dynamics. *J. Mol. Graph.* **1996**, *14* (1), 33–38.
- (88) Gowers, R. J.; Linke, M.; Barnoud, J.; Reddy, T. J. E.; Melo, M. N.; Seyler, S. L.; Domański, J.; Dotson, D. L.; Buchoux, S.; Kenney, I. M.; others. MDAnalysis: A Python Package for the Rapid Analysis of Molecular Dynamics Simulations. In *Proceedings of the 15th Python in Science Conference*; 2016; Vol. 98.
- (89) Michaud-Agrawal, N.; Denning, E. J.; Woolf, T. B.; Beckstein, O. MDAnalysis: A Toolkit for the Analysis of Molecular Dynamics Simulations. *J. Comput. Chem.* **2011**, *32* (10), 2319–2327.
- (90) Kara, S.; Afonin, S.; Babii, O.; Tkachenko, A. N.; Komarov, I. V.; Ulrich, A. S. Diphytanoyl Lipids as Model Systems for Studying Membrane-Active Peptides. *BBA - Biomembr.* **2017**, *1859* (10), 1828–1837. <https://doi.org/10.1016/j.bbamem.2017.06.003>.
- (91) Yoo, J.; Cui, Q. Three-Dimensional Stress Field around a Membrane Protein: Atomistic and Coarse-Grained Simulation Analysis of Gramicidin A. *Biophys. J.* **2013**, *104* (1), 117–127. <https://doi.org/10.1016/j.bpj.2012.11.3812>.
- (92) Lundbæk, J. A.; Andersen, O. S. Spring Constants for Channel-Induced Lipid Bilayer Deformations: Estimates Using Gramicidin Channels. *Biophys. J.* **1999**, *76* (2), 889–895. [https://doi.org/10.1016/S0006-3495\(99\)77252-8](https://doi.org/10.1016/S0006-3495(99)77252-8).
- (93) Quist, P. O. <sup>13</sup>C Solid-State NMR of Gramicidin A in a Lipid Membrane. *Biophys. J.* **1998**, *75* (5), 2478–2488. [https://doi.org/10.1016/S0006-3495\(98\)77692-1](https://doi.org/10.1016/S0006-3495(98)77692-1).
- (94) Kim, T.; Lee, K. Il; Morris, P.; Pastor, R. W.; Andersen, O. S.; Im, W. Influence of Hydrophobic Mismatch on Structures and Dynamics of Gramicidin A and Lipid Bilayers. *Biophys. J.* **2012**, *102* (7), 1551–1560. <https://doi.org/10.1016/j.bpj.2012.03.014>.
- (95) Lundbaek, J. A.; Koeppe, R. E.; Andersen, O. S. Amphiphile Regulation of Ion Channel Function by Changes in the Bilayer Spring Constant. *Proc. Natl. Acad. Sci. U. S. A.* **2010**, *107* (35), 15427–15430. <https://doi.org/10.1073/pnas.1007455107>.
- (96) Rasmussen, A.; Rasmussen, T.; Edwards, M. D.; Schauer, D.; Schumann, U.; Miller, S.; Booth, I. R. The Role of Tryptophan Residues in the Function and Stability of the Mechanosensitive Channel MscS from Escherichia Coli. *Biochemistry* **2007**, *46* (38), 10899–10908. <https://doi.org/10.1021/bi701056k>.
- (97) Barth, A.; Zscherp, C. What Vibrations Tell Us about Proteins. *Q. Rev. Biophys.* **2002**, *35* (4), 369–430.
- (98) Sychev, S. V.; Barsukov, L. I.; Ivanov, V. T. The Double  $\Pi\pi$ 5.6 Helix of Gramicidin A Predominates in Unsaturated Lipid Membranes. *Eur. Biophys. J.* **1993**, *22* (4), 279–288. <https://doi.org/10.1007/BF00180262>.
- (99) Gambucci, M.; Gentili, P. L.; Sassi, P.; Latterini, L. A Multi-Spectroscopic Approach to Investigate the Interactions between Gramicidin A and Silver Nanoparticles. *Soft Matter* **2019**, *15* (32), 6571–6580. <https://doi.org/10.1039/c9sm01110b>.

- (100) Urry, D. W.; Shaw, R. G.; Trapane, T. L.; Prasad, K. U. Infrared Spectra of the Gramicidin A Transmembrane Channel: The Single-Stranded-B<sub>6</sub>-Helix. *Biochem. Biophys. Res. Commun.* **1983**, No. 1, 373–379. <https://doi.org/10.1017/CBO9781107415324.004>.
- (101) Hwang, T. C.; Koeppe, R. E.; Andersen, O. S. Genistein Can Modulate Channel Function by a Phosphorylation-Independent Mechanism: Importance of Hydrophobic Mismatch and Bilayer Mechanics. *Biochemistry* **2003**, *42* (46), 13646–13658. <https://doi.org/10.1021/bi034887y>.
- (102) Feller, S. E.; Pastor, R. W. Constant Surface Tension Simulations of Lipid Bilayers: The Sensitivity of Surface Areas and Compressibilities. *J. Chem. Phys.* **1999**, *111* (3), 1281–1287.
- (103) Sukharev, S.; Anishkin, A. Mechanosensitive Channels: What Can We Learn from “simple” Model Systems? *Trends Neurosci.* **2004**, *27* (6), 345–351. <https://doi.org/10.1016/j.tins.2004.04.006>.
- (104) Wallace, B. A. Structure of Gramicidin A. *Biophys. J.* **1986**, *49* (1), 295–306. [https://doi.org/10.1016/S0006-3495\(86\)83642-6](https://doi.org/10.1016/S0006-3495(86)83642-6).
- (105) Kelkar, D. A.; Chattopadhyay, A. The Gramicidin Ion Channel: A Model Membrane Protein. *Biochim. Biophys. Acta - Biomembr.* **2007**, *1768* (9), 2011–2025. <https://doi.org/10.1016/j.bbamem.2007.05.011>.
- (106) Andersen, O. S.; Koeppe, R. E. Bilayer Thickness and Membrane Protein Function: An Energetic Perspective. *Annu. Rev. Biophys. Biomol. Struct.* **2007**, *36*, 107–130. <https://doi.org/10.1146/annurev.biophys.36.040306.132643>.
- (107) Yin, S.; Liu, J.; Kang, Y.; Lin, Y.; Li, D.; Shao, L. Interactions of Nanomaterials with Ion Channels and Related Mechanisms. *Br. J. Pharmacol.* **2019**, *176* (19), 3754–3774. <https://doi.org/10.1111/bph.14792>.
- (108) Lundbaek, J. A.; Collingwood, S. A.; Ingolfsson, H. I.; Kapoor, R.; Andersen, O. S. Lipid Bilayer Regulation of Membrane Protein Function: Gramicidin Channels as Molecular Force Probes. *J. R. Soc. Interface* **2010**, *7* (44), 373–395. <https://doi.org/10.1098/rsif.2009.0443>.
- (109) Antonenko, Y. N.; Borisenko, V.; Melik-Nubarov, N. S.; Kotova, E. A.; Woolley, G. A. Polyanions Decelerate the Kinetics of Positively Charged Gramicidin Channels as Shown by Sensitized Photoinactivation. *Biophys. J.* **2002**, *82* (3), 1308–1318. [https://doi.org/10.1016/S0006-3495\(02\)75486-6](https://doi.org/10.1016/S0006-3495(02)75486-6).
- (110) Stevenson, P.; Tokmakoff, A. Distinguishing Gramicidin D Conformers through Two-Dimensional Infrared Spectroscopy of Vibrational Excitons. *J. Chem. Phys.* **2015**, *142* (21). <https://doi.org/10.1063/1.4917321>.
- (111) Sychev, S. V.; Nevskaya, N. A.; Jordanov, S.; Shepel, E. N.; Miroshnikov, A. I.; Ivanov, V. T. The Solution Conformations of Gramicidin A and Its Analogs. *Bioorg. Chem.* **1980**, *9* (1), 121–151. [https://doi.org/10.1016/0045-2068\(80\)90035-8](https://doi.org/10.1016/0045-2068(80)90035-8).
- (112) Brannigan, G.; Brown, F. L. H. A Consistent Model for Thermal Fluctuations and Protein-Induced Deformations in Lipid Bilayers. *Biophys. J.* **2006**, *90* (5), 1501–1520.
- (113) Huang, H. W. Deformation Free Energy of Bilayer Membrane and Its Effect on

Gramicidin Channel Lifetime. *Biophys. J.* **1986**, *50* (6), 1061–1070.  
[https://doi.org/10.1016/S0006-3495\(86\)83550-0](https://doi.org/10.1016/S0006-3495(86)83550-0).

(114) Venable, R. M.; Brown, F. L. H.; Pastor, R. W. Mechanical Properties of Lipid Bilayers from Molecular Dynamics Simulation. *Chem. Phys. Lipids* **2015**, *192*, 60–74.  
<https://doi.org/10.1016/j.chemphyslip.2015.07.014>.

### **Chapter 3: Nanoparticle tracking analysis and statistical mixture distribution analysis to quantify nanoparticle–vesicle binding**

The following chapter is adapted from an article in submission to JCIS with the following co-authors: Ting Fung Ma, Brandon M. Hoover, Meng Wu, Catherine J. Murphy, Regina Murphy, and Joel A. Pedersen

\*Contributions to this publication include: Conceptualization, methodology, experimental design and data collection, and writing and editing of the manuscript.

#### **3.1 Introduction**

Nanoparticle tracking analysis (NTA) is a single-particle tracking technique that allows high-resolution determination of particle size distributions for polydisperse samples<sup>1</sup>. In NTA, the Brownian motion of individual particles diffusing in solution is tracked via the light they scatter or emit (in the case of fluorescent particles) under laser illumination using a microscope equipped with a video camera<sup>1</sup>. The mean squared displacement in the  $x$ - $y$  plane is used to calculate translational diffusion coefficients ( $D_T$ ) for individual particles, yielding a number distribution of diffusivities, from which hydrodynamic diameters ( $d_h$ ) can be derived by the Stokes–Einstein or other diffusional models<sup>1,2</sup>. The determination of a true number distribution of diffusion coefficients represents a distinct advantage over ensemble techniques such as dynamic light scattering (DLS)<sup>1</sup>. The upper bound for the size of particles amenable to tracking by NTA is  $\sim 1000$  nm due to their slow Brownian motion, whereas the lower size limit depends on particle refractive index, laser wavelength and power, and sensitivity of the camera, and can range from  $\sim 10$  to  $\sim 50$  nm<sup>3-5</sup>.

Nanoparticle tracking analysis has been used to characterize the hydrodynamic properties of nanoscale particles (e.g., engineered nanoparticles, liposomes, extracellular vesicles, viruses, protein aggregates) in mixtures<sup>3-8</sup> and to monitor protein aggregation<sup>9</sup>. Nanoparticle tracking analysis has been used to monitor the bioconjugation of gold nanoparticles (AuNPs) by protein A and subsequent interaction of immunoglobulin G (IgG) with the conjugated particles by measuring the change in mean hydrodynamic diameter as a function of protein A or IgG concentration, respectively<sup>1,3,7</sup>. As a single-particle tracking

technique, NTA allows more accurate determination of particle size distribution in polydisperse samples<sup>3-5</sup>. In polydisperse mixtures in which particles may bind to one another, determining the proportion of particles in each binding state (e.g., unbound, pairs, triplets) is a more complicated task than comparison of mean particle sizes. Approaches need to be developed to analyze NTA data from the highly polydisperse samples that result from mixtures containing both unbound and (multiply) bound populations. This challenge can be met by application of statistical mixture distribution analysis to histograms of particle diffusivities, or hydrodynamic diameters, determined by NTA. Mixture distribution analysis can also provide an estimate of binding ratios between particle types present in a mixture.

The objective of this study was to evaluate the application of statistical mixture distribution analysis to NTA data for the purpose of estimating bound populations in a polydisperse mixture. The experimental system investigated consisted of small unilamellar vesicles (SUVs) and anionic gold nanoparticles (AuNPs). Small unilamellar vesicles are commonly used to investigate the interaction of nanoparticles with phospholipid bilayers as simple models for cell membranes<sup>10-13</sup>. Understanding of nanoparticle interaction with cell membranes can aid the design of nanoparticles for biomedical applications<sup>14-16</sup> and inform the assessment of potential adverse outcomes of exposures to nanoparticles due to their release into the environment<sup>13,14,17-20</sup>. In the present study, we employed vesicles composed of zwitterionic lipids and compared AuNP binding to vesicles that either lacked or contained the model ion channel gramicidin A (gA). Prior work has demonstrated that anionic AuNP binding to zwitterionic lipid bilayers can modulate gA activity<sup>21</sup>. In the mixture distribution analysis we evaluated two diffusion models (Stokes–Einstein and Kirkwood–Riseman) using the statistical fitness of each model to determine model suitability. We demonstrate that the combination of NTA and mixture distribution analysis can be used to discriminate nanoparticle binding to different vesicle types – here, either lacking or containing gA. Thus, the approach developed can be used to investigate the influence of individual membrane components on nanoparticle binding. Overall, this method provides a quantitative improvement over DLS measurements for assessment of particle–particle interactions that arise in complex colloidal systems such as nanoparticle–vesicle mixtures.

## 3.2. Materials and methods

### 3.2.1 Synthesis of gold nanoparticles capped with 3-mercaptopropionic acid (MPA)

We synthesized MPA-AuNPs following a published protocol with modifications<sup>22</sup>. Briefly, we added HAuCl<sub>4</sub> (3 mL, 0.1 M) to 700 mL ultrapure water in an Erlenmeyer flask. Subsequently, 333  $\mu$ L of 0.1 M MPA followed by 1.4 mL of 1.0 M NaOH solution was added to the aqueous solution under gentle stirring. Fresh 0.1 M NaBH<sub>4</sub> solution (10 mL) was quickly added to the above reaction mixture under rigorous stirring. The combined solutions rapidly changed color to a deep red-brown, and the reaction mixture was stirred gently for 2 h. The MPA-AuNPs were purified by centrifugation (55 min, 13,000g, twice) and redispersed in 1 mM NaOH after the first centrifugation and ultrapure water ( $\geq 18$  M $\Omega$ ·cm) after the second centrifugation.

### 3.2.2. Ultraviolet-visible absorbance spectroscopy

The UV-vis spectra of MPA-AuNP suspensions were acquired on a Cary 5000 UV-vis spectrophotometer. The diameter of MPA-AuNP was estimated in solution by UV-vis spectroscopy to be around 3.3 nm<sup>23</sup>. TEM image analysis indicated that the core diameter of MPA-AuNPs were  $3.3 \pm 0.6$  nm ( $n > 200$ ).

### 3.2.3. Transmission electron microscopy (TEM)

For TEM imaging, 5  $\mu$ L of a dilute solution of MPA-AuNPs was drop-cast onto a copper TEM grid with 400 mesh ultrathin carbon film on lacey carbon support film (Ted Pella), and images were acquired with a JEOL 2100 cryo TEM. The TEM sizing analysis was performed by ImageJ.

### 3.2.4. Formation and characterization of SUVs.

Small unilamellar vesicles for analysis by DLS and NTA were formed using the extrusion method<sup>24,25</sup>. We chose to construct vesicles from the zwitterionic phospholipid DPhPC to allow comparison to previous studies where gA ion channels were embedded in suspended planar DPhPC membranes<sup>21</sup>. Briefly, DPhPC lipids purchased in chloroform and gA diluted in 2,2,2-trifluoroethanol were combined to a

DPhPC:gA molar ratio of about 27.8:1. The mixture was then completely dried under ultrapure N<sub>2</sub> gas, followed by rehydration to a lipid concentration of 2.5 mM in 0.150 M KCl buffered to pH 7.5 using 0.01 M HEPES by sonication for 30 min. The salt concentration was chosen for both physiological relevance in terms of ionic strength, and direct comparison to a previous study indicating that MPA-AuNPs can alter the function of gA<sup>21</sup>. The resulting solution of lipid and gA is then extruded 11 times through a 0.05 μm polycarbonate filter (Whatman). Vesicles lacking gA were formed in a similar manner with DPhPC lipid only. All vesicle solutions were used within 1 week of extrusion and were stored at 4 °C. Vesicle hydrodynamic diameters are reported in Table 1. The vesicle sizes are larger than the 50 nm pore size as commonly observed for vesicles extruded through filter sizes <100 nm<sup>24,26</sup>.

### 3.2.5 Fluorescence spectroscopy

Fluorescence spectroscopy was used to confirm the presence of gA in vesicles by observation of an emission maximum at 328 nm when referenced to vesicles lacking gA<sup>27,28</sup>. This peak indicates the presence of gA in its ion channel conformation, which occurs only when embedded in the lipid membrane<sup>27,28</sup>. Fluorescence spectra were measured using an ISS K2 spectrofluorimeter set to 1.0 mm slit width and equipped with a neutral density filter of 1.0 optical density. An excitation wavelength of 280 nm was used, and emission was collected from 300 to 400 nm. The presence of a maxima at 328 nm indicated the presence of gA in vesicles.

### 3.2.6. Nanoparticle tracking analysis

Binding of gold nanoparticles to vesicles consisting of DPhPC with and without gA peptide were monitored by NTA. Briefly, particles in the sample scatter light from a 405 nm laser, and the scattered light is tracked using a high-sensitivity camera. By measuring the trajectory of the diffusing particle over a tracking time  $t$ , the translational diffusion coefficient  $D_T$  is calculated and  $d_{h,n}$  is estimated<sup>4,29</sup>:

$$\overline{(x, y)^2} = 4D_T t = \frac{4k_B T t}{3\pi d_{h,n} \eta} \quad (1)$$

where  $k_B$  is the Boltzmann constant,  $T$  is temperature, and  $\eta$  is dynamic viscosity. Given a particle shape and dimensions,  $d_h$  can be calculated from well-established equations.

All NTA measurements were performed with a Nanosight LM10 (Nanosight) using a 405 nm laser at room temperature. Vesicle samples were diluted to a concentration range optimal for tracking ( $10^8$ - $10^9$  particles·mL<sup>-1</sup>)<sup>30</sup>. Samples were then injected directly into the sample chamber using Luer Lok syringes (BD). Analysis of the number distribution of particle sizes was conducted using NTA 3.0 software using a detection threshold of 4. The detection threshold establishes the minimum pixel brightness by the software for particle tracking, and settings were adjusted according to manufacturer recommendation to eliminate tracking background noise. The camera level determines the amount of scattered light entering the camera (i.e., the brightness of particles) and a setting of 13 was selected such that all particles could be clearly detected with no more than 20% of particles reaching pixel saturation.

Nanoparticle tracking analysis requires extremely dilute solutions ( $10^7$ - $10^9$  particles·mL<sup>-1</sup>) to track individual particles by light scattering. To achieve a particle concentration in this range, 0.05  $\mu$ L of 2.5 mM vesicles were combined with 0.05  $\mu$ L of 487.3 nM MPA-AuNPs and diluted to 10 mL with 0.150 M KCl buffered to pH 7.4 with 0.01 M HEPES. Nanoparticle tracking analysis was performed on 1 mL aliquots of this solution. Similar measurements were performed on individual samples of vesicles and MPA-AuNPs. Assuming only two-body collisions, the aggregation rate scales as the product of the concentrations of the two colliding species<sup>31</sup>. We therefore expect the aggregation rate to be lower in the NTA experiments (due to lower particle concentration) than in the DLS experiments. We therefore avoid a direct, quantitative comparison between NTA and DLS, which were collected on similar time scales.

### **3.2.7. Dynamic light scattering**

Dynamic light scattering measures the intensity of laser light passed through a liquid sample, recording intensity fluctuations that occur over time due to occlusion of laser light by particles diffusing via Brownian motion. Small particles diffuse more rapidly than large particles and therefore produce faster

intensity fluctuations. Intensity fluctuations are converted to translational diffusion coefficients via the autocorrelation function,  $G(t)$ , which involves assessing destructive interference of intensity fluctuations by mathematical comparison of originally measured fluctuation signal and that signal shifted by some time delay. Smaller particles produce higher frequency fluctuations than larger particles, so they require a smaller time shift for destructive interference. An exponential function is used to model this time-shifted autocorrelation function, the decay of which occurs faster for smaller particles due to the smaller time delay required to reach destructive interference. Cumulants analysis (a moments expansion) represents a simple approach to model the autocorrelation function <sup>32</sup>:

$$G(t) = A[1 + B\exp(-2D_T q^2 \tau + \mu_2 \tau^2)] \quad (2)$$

where  $A$  is the  $y$ -intercept of the correlation function,  $B$  is the baseline,  $D_T$  is the translational diffusion coefficient,  $q$  is the scattering vector,  $\tau$  is the time delay, and  $\mu_2$  is the second moment of the cumulants expansion. The hydrodynamic diameter based on the translational diffusion coefficient obtained from the single exponential fit to the autocorrelation function is termed the  $Z$ -average hydrodynamic diameter ( $d_{h,Z}$ ). The  $d_{h,Z}$  is an intensity-weighted mean hydrodynamic diameter and is thus highly sensitive to increases in particle size and biased towards the presence of even small concentrations of highly aggregated particles <sup>32</sup>. The polydispersity index (PDI), a measure of the width of distribution of hydrodynamic diameters, is derived from the second moment <sup>32</sup>. Thus,  $Z$ -average and PDI are the values most directly derived from the autocorrelation function. The number distribution of hydrodynamic diameters can be derived from the intensity distribution using Mie scattering theory, which carries the assumption that all particles are homogeneous and spherical. The conversion to the number-average hydrodynamic diameter removes intensity weighting, such that resulting diameter is primarily dictated by the most abundant particle size <sup>32</sup>. Due to lack of intensity weighting, number-average is less sensitive to small increases in particle size.

Hydrodynamic diameters and PDI values of 5 nM MPA-AuNPs, 1 mM vesicles, and a combination of 5 nM MPA-AuNPs and 1 mM vesicles were determined using DLS (Malvern Zetasizer Nano ZS). A 173° backscattering angle was used during data collection, with a 633 nm He-Ne laser and temperature held

at 25.0 °C. Each sample was placed in a solution of 0.150 M KCl buffered to pH 7.4 with 0.01 M HEPES. Nanoparticle concentrations corresponded to ~1:27 AuNP:vesicle ratio, the same as that used for later NTA measurements. The Z-average hydrodynamic diameter and PDI were derived from cumulants analysis of the autocorrelation function. Hydrodynamic diameters represent the average of three replicates of a single sample, and these data are reported in Table 1. We note that the hydrodynamic diameters determined in the 0.150 M KCl solution exceeded that determined by TEM and reflect aggregation induced by charge screening, consistent with numerous other studies demonstrating aggregation of colloidal gold nanomaterials in saline media <sup>21,33</sup>.

### 3.2.8. Laser Doppler electrophoresis

Laser doppler electrophoresis was used to determine the electrophoretic mobilities of the MPA-AuNPs, the vesicles, and the vesicles mixed with MPA-AuNPs, all in 0.150 M KCl buffered to pH 7.4 with 0.01 M HEPES at 25.0 °C (Malvern Zetasizer Nano ZS). The MPA-AuNP concentration was 5 nM and that of the vesicles was 1 mM. These concentrations correspond to ~1:27 AuNP:vesicle ratio. The Smoluchowski equation was used to calculate  $\zeta$ -potentials from the electrophoretic mobilities. Measured  $\zeta$ -potentials represent the average of five replicates of a single sample, and these data are reported in Table 1. As expected, zwitterionic DPhPC vesicles exhibited  $\zeta$ -potentials near 0. Addition of gA did not alter vesicle  $\zeta$ -potential. The MPA-AuNPs exhibited negative  $\zeta$ -potentials as expected.

### 3.2.9. Statistical analysis of mixture distributions

We used a simulation-based finite mixture approach to estimate the proportion of particle bound at different AuNP:vesicle ratios when mixed. The distributions of nanoparticle (MPA-AuNPs) and vesicle (DPhPC or DPhPC + gA) diameters were each obtained from experimental data and binned in 10 nm intervals for subsequent analysis. Smoothing was then applied to the average sampling distribution among three replicates <sup>34</sup>. To apply a finite mixture approach, each particle in the mixture is assumed to belong to only one of the following particle types: nanoparticle alone, vesicle alone, or bound species (in varying

AuNP:vesicle ratios). Because the total number of particle types are known, a finite mixture scenario<sup>35</sup> can be applied to determine the proportion of each particle type from an observed distribution of particle sizes. Application of the finite mixture approach first involves employing a probability mass function (pmf) to describe the proportion of a particle type in the mixture where  $X_1, \dots, X_n$  represent random samples from this finite mixture. In the implementation of mixture analysis here,  $X_i$  is the observed diameter of the  $i^{\text{th}}$  particle. We note that pmfs are used in the case that the variable can take a finite number of values. The approach can be extended to cases with continuous random variables by using a probability mass function, replacing the summation with an integration.

$$\Pr_{mix}(X_i = x) = \phi_{mix}(x) = \sum_{j=1}^m \lambda_j \phi_j(x) \quad (3)$$

In this approach,  $m$  is the number of particle types,  $x$  is the bin center diameter,  $\phi_j$  and  $\lambda_j$  are the pmf and corresponding proportion in the mixture of the  $j$ -th particle type. The primary goals are to estimate and construct confidence intervals of the  $\lambda_j$  values and compare observed (experimental) and estimated (statistically modeled) pmfs in terms of fitness.

Mathematically, the complete data are  $C_i = (X_i, Z_i)$ , where  $Z_i = (Z_{i1}, \dots, Z_{im})$  is a single trial multinomial random variable ( $m$ -dimensional vector) and  $Z_{ij} \in \{0,1\}$  is the random variable indicating the  $i$ -th particle comes from component  $j$ . Note, we use upper case to denote a random quantity and lower case to signify a fixed or realization of the random quantity (i.e., observed data). Since each particle in the mixture belongs to only one particle type, we define

$$\Pr(Z_{ij} = 1) = \lambda_j, \Pr(X_i = x_i | Z_{ij} = 1) = \phi_j(x_i), j = 1, \dots, m \quad (4)$$

such that

$$\sum_{j=1}^m \Pr(Z_{ij} = 1) = \sum_{j=1}^m \lambda_j = 1 \quad (5)$$

The complete-data likelihood (assuming the  $\phi_j$  are known) is then given by

$$\ell_{complete}(\lambda; C) = \prod_i^n \sum_{j=1}^m Z_{ij} \lambda_j \phi_j(X_i), \quad (6)$$

where  $\lambda = (\lambda_1, \dots, \lambda_m)$  and  $C = \{C_i\}^n$ . When the  $\phi_j$  are known, the  $\lambda_j$  values can be estimated by an expectation-maximization (EM) algorithm<sup>35</sup>. The EM algorithm iteratively maximizes the expectation of observed log-likelihood:

$$Q(\lambda|\lambda^{(t)}) = E[\log \ell_{complete}(\lambda; C) | x, \lambda^{(t)}], \quad (7)$$

where  $\lambda^{(t)}$  is the (estimated) proportion at iteration  $t$  and updates the proportion estimate by

$$\lambda^{(t+1)} = \operatorname{argmax}_\lambda Q(\lambda | \lambda^{(t)}) \quad (8)$$

The expectation and maximization steps can be computed, first by updating the probability that the  $i$ -th data point falls into the  $j$ -th component:

$$p_{ij}^{(t)} := \Pr_{\lambda^{(t)}}(Z_{ij} = 1 | X_i = x_i) = \frac{\lambda_j^{(t)} \phi_j(x_i)}{\sum_{k=1}^m \lambda_k^{(t)} \phi_k(x_i)} = \left[ 1 + \sum_{k \neq j} \frac{\lambda_k^{(t)} \phi_k(x_i)}{\lambda_j^{(t)} \phi_j(x_i)} \right]^{-1} \quad (9)$$

Then by calculating an estimate of  $\lambda$  by

$$\lambda_j^{(t+1)} = \frac{1}{n} \sum_i^n p_{ij}^{(t)}, j = 1, \dots, m. \quad (10)$$

The estimation process is conducted iteratively and terminated when the difference between  $\lambda^{(t+1)}$  and  $\lambda^{(t)}$  is sufficiently small, chosen here to be when  $\sum_{j=1}^m |\lambda^{(t+1)} - \lambda^{(t)}| < 10^{-6}$ , that is, when the change between iterations is precise to the 6<sup>th</sup> decimal place. We used a self-written R code to implement this iterative finite mixture process.

A non-parametric spline<sup>34</sup> was applied to smooth the sample probability mass function ( $\phi_j$ ), which consisted of a set of relative frequencies of particle diameters calculated from diffusion coefficients using one of two diffusional models (viz. the Stokes–Einstein or Kirkwood–Riseman models)<sup>36,37</sup>. A large number of random sampling from the relative frequencies is necessary to simulate a probability mass

function for the mixture ( $\phi_{mix}$ ). We determined that the use of  $10^6$  random samples was sufficient to accurately mimic experimental mixture data. For further statistical inference, the sampling and estimation procedures are repeated 1,000 times. In sum, our approach can be viewed as a form of parametric bootstrapping<sup>38</sup>, which can be used to recover the function of an underlying distribution.

This process can be thought of as a random drawing of particles from distributions of nanoparticle and vesicle diameters to produce an estimated mixture distribution. Particle diameters are obtained from measured diffusion coefficients by application of one of two diffusional models. The fitness of each model is assessed by measuring the statistical distance between estimated and observed mixture distributions using the Cramér–von Mises criterion, which is the sum of squared distances between the estimated and observed distribution<sup>39</sup>. A Wilcoxon rank sum test is used to compare the CVMs based on Stokes–Einstein or Kirkwood–Riseman model. Computations were conducted in R with packages<sup>40</sup>, and the R code is included in the SI for user reference.

### **3.3 Results and discussion**

#### **3.3.1. Assessment of nanoparticle binding to vesicles by DLS**

We used two figures of merit to characterize the binding of nanoparticles to vesicles: the Z-average and number-average hydrodynamic diameters. The Z-average hydrodynamic diameter is an intensity-weighted hydrodynamic diameter. Because Rayleigh scattering is proportional to the sixth power of the particle radius, it is more sensitive to the presence of large particles that scatter light with higher intensity. Thus, Z-average is sensitive to small amounts of binding or aggregation. The number-average hydrodynamic diameter expresses the mean hydrodynamic diameter based on the number of particles of various sizes present in the measured suspension, without intensity weighting. Thus, the number-average hydrodynamic diameter is less sensitive to binding or aggregation than the Z-average hydrodynamic diameter.

Anionic MPA-AuNPs were introduced to suspensions of vesicles that lacked or contained gA to determine if the inclusion of this channel-forming peptide alters nanoparticle binding. Analysis of DLS data (Fig. 1) reveals that the Z-average hydrodynamic diameter vesicles increased upon introduction of MPA-AuNPs regardless of the presence of gA. However, the magnitude of change is larger for gA-containing vesicles, suggesting that the presence of gA increases binding. Moreover, the number-average hydrodynamic diameter shifted for only the AuNP-exposed gA-containing vesicles. Together these results suggest that although binding to both vesicle types occurs (as indicated by changes in the aggregation-sensitive Z-average), the presence of gA in the vesicles increases AuNP-vesicle binding (either by formation of more or larger aggregates). Since the number-average is much less sensitive to the presence of large particles, the increased number-average observed only for gA-containing vesicles may indicate increased binding in comparison to gA-lacking vesicles.

However, assessment of binding by DLS is limited to hypothesizing that AuNPs may bind more to vesicles containing gA relative to those lacking gA based on analysis of ensemble averaged hydrodynamic diameters. Moreover, DLS cannot accurately distinguish between increased hydrodynamic diameter due to many AuNPs binding in a 1:1 AuNP:vesicle ratio versus a few very large AuNP-vesicle clusters. The use of NTA allows us to determine which of these scenarios is occurring.

### 3.3.2. Determination of fraction of AuNPs bound from mixture distributions and NTA

Nanoparticle tracking analysis allows determination of the lateral diffusion coefficients of individual particles based on the analysis of the trajectories of scattering particles captured with a video camera. Histograms of estimated lateral diffusion coefficients are plotted in Fig. 2. Initial comparison of median hydrodynamic diameters derived from raw NTA diffusion coefficient histograms indicates a change upon introduction of MPA-AuNPs to gA-containing vesicles ( $p < 0.001$ ; non-parametric Mann-Whitney  $U$  test), but not to vesicles lacking gA. The general observation that the presence of gA may lead to more binding of MPA-AuNPs is consistent with the interpretation of the DLS results (*vide supra*) and likewise

provides insufficient information to determine specific AuNP:vesicle binding ratios or quantitation of the degree of binding.

Diffusion coefficient histograms (Fig. 2) demonstrate multi-peak character for both SUV and SUV-gA samples which complicates comparison of sample means once MPA-AuNPs are added. cursory visual assessment of the multi-peak histograms suggests that there may be shifts in individual peaks towards smaller diffusion coefficients (larger particle hydrodynamic diameters). However, peak assignments by particle type and attempted quantification of peak shifts are again complicated by multi-peak character and made difficult to assess with certainty. Thus, sample analysis in this manner is not reliable.

To provide a more descriptive and quantitative measure of binding to vesicles lacking or containing gA, we applied statistical mixture distribution to the NTA data <sup>41</sup>. Fig. 3 depicts a schematic of how mixture distributions were employed to the systems of interest in this study. The process involves randomly drawing nanoparticle and vesicle diffusion coefficients from measured NTA histogram data, artificially “binding” them in different AuNP:vesicle ratios by applying a binding model describes the diffusion coefficient of the bound species, and then repeating this process until the new histogram of artificially bound species closely matches ( $\alpha = 0.05$ , 1000 replicates) that which was experimentally collected.

### 3.3.3. Stokes–Einstein model

Application of mixture distributions to NTA data requires that an assumptions be made to relate diffusion coefficients to particle binding. The Stokes–Einstein model is the simplest and most commonly used model relating the translational diffusion coefficient to particle hydrodynamic diameter ( $d_h$ ) <sup>42</sup>:

$$d_h = \frac{k_B T}{3\pi\eta D_T} \quad (11)$$

where  $k_B$ ,  $T$ , and  $\eta$  are defined as above. We applied the Stokes–Einstein model to the experimental data in a simple manner by assuming that two bound spherical particles diffuse such that their diffusion coefficient

equals that of a single larger sphere of encompassing diameter (i.e., the bound pair is modeled as a sphere with diameter equal to the sum of the diameters of the two particles).

Figs. 4 and 5 summarize the results from application of the Stokes–Einstein model and subsequent mixture distribution analysis of NTA data. Results from this model fit all of the experimental data such that they are explained by only four possible components: AuNPs, vesicles, and bound species—either attached (1:1 AuNP:vesicle) or bridged (1:2 AuNP:vesicle). Application of this model predicts that the attached (1:1) and bridged (1:2) populations increase from ~3% to 34% and 0.1% to 0.5%, respectively, upon inclusion of gA in vesicles. This increase in binding to gA-containing vesicles qualitatively agrees with a previous study which found that MPA-AuNPs can bind to gA-containing membranes <sup>21</sup>.

The manner in which the Stokes–Einstein model was applied assumes a spherical nature of bound AuNP–vesicle species, which may instead resemble a linear chain. This spherical assumption estimates that multi-unit objects diffuse slower than they actually do, largely due to the increased friction factor for a large, encompassing sphere relative to a chain of bound particles <sup>42</sup>. Thus, Stokes–Einstein may fail to accurately describe the diffusion of particles that bind to form a linear chain, which may be especially relevant for AuNP–vesicle binding that exceeds the 1:1 (attached) ratio.

#### **3.3.4. Kirkwood–Riseman model**

Analysis of NTA using the Stokes–Einstein model showed that bound populations include a 1:2 ratio of AuNP:vesicle (bridged). Our implementation of the Stokes–Einstein model is not expected to accurately predict the diffusion of multi-component objects<sup>36,43</sup>, as the presence of such chain binding violates the underlying spherical assumption. Thus, we apply a second model that can better account for the presence of multi-component objects as would be the case if several vesicles bind to a single nanoparticle. The Stokes–Einstein relation can be modified by a multiplicative factor to account for multi-unit objects in the form of the Kirkwood–Riseman model <sup>36</sup>. The Kirkwood–Riseman model assumes chain binding and that the size of each subunit is identical <sup>36</sup>. Although the identical size criterion is not met for

our system of nanoparticles and vesicles (Table 1), this model was tested because the accuracy of a chain model may still exceed that of a spherical assumption (as in the implementation of the Stokes–Einstein estimation above) despite some underestimation of the adjustment factor due to unequal sizes.

The Kirkwood–Riseman model allows calculation of an adjustment factor from the ratio of friction factors between chain ( $f$ ) and monomer ( $f_m$ ) is described as <sup>36</sup>

$$\frac{f}{f_m} = N \left[ 1 + \left( \frac{1}{N} \right) \sum_i \sum_{j \neq i} \alpha_{ij}^{-1} \right]^{-1} \quad (12)$$

where  $N$  is the number of subunits in the chain and  $\alpha_{ab}$  denotes the distance between subunits  $a$  and  $b$ . By this equation, the ratio of friction factors for a two subunit chain is 1.33 and that of a three subunit chain is 1.64. The friction factor itself ( $f$ ) <sup>36</sup>:

$$f = 3\pi\eta d_h \quad (13)$$

is proportional to  $d_h$ . Thus, the Kirkwood–Riseman model can be used to correct hydrodynamic diameters resulting from the assumption of additive diameter upon binding. This mathematical adjustment can be made by simple multiplication of the adjustment factor to Stokes–Einstein sizes, as dictated by the number of particles binding in the chain. To apply the Kirkwood–Riseman model, we assumed that the nanoparticle and vesicle hydrodynamic diameters were similar (Table 1), and used the bin center radii from the NTA histogram and adjustment factors (e.g.,  $1.33 \times (\text{vesicle radius})$  for 1:1 AuNP:vesicle bound species) to calculate attached sizes.

To assess AuNP–vesicle binding, we assumed that all binding configurations demonstrate higher vesicle than AuNP concentrations, since vesicles were present in excess by a factor of 10 relative to nanoparticles in our NTA experiments. Moreover, we assume that nanoparticles will not homoaggregate to a larger extent in the presence of vesicles than in their absence. These two assumptions taken together would limit the potential binding configurations to 1:1 AuNP:vesicle (attached) and 1:2 AuNP:vesicle (bridged) populations. Application of the Kirkwood–Riseman model in this manner reveals that attached species (1:1

AuNP:vesicle) increased from ~16% to 41% and bridged species (1:2 AuNP:vesicle) increased from 0.01% to 20% with the inclusion of gA in vesicles. Thus, this model qualitatively agrees with the Stokes–Einstein model; both models predict that inclusion of gA in vesicles leads to more total binding and an increase in both attached (1:1) and bridged (1:2) species. Up to ~2% of the experimentally measured diffusion coefficients cannot be accounted for using the Kirkwood–Riseman model when chain binding is limited to attached (1:1) and bridged (1:2) species according to the criteria we applied. The failure to capture the entire population may be attributed to the presence of a small population of species that have aggregated beyond the assigned 1:1 or 1:2 binding states.

### 3.4. Conclusion

We demonstrate that the unique combination of mixture distributions and NTA used in this work can be used to assess binding in a manner that both qualitatively agrees with ensemble DLS measurements and provides quantitative information on proportion of binding in different configurations (ratios). Employing two different binding models, Stokes–Einstein and Kirkwood–Riseman, demonstrated that, although the trends in binding were similar, the proportion of binding in different ratios is sensitive to model type. The fitness of each model was tested using the Cramér–von Mises criterion, or the sum of squared distances between the estimated and observed distribution resulting from statistical analysis. The Kirkwood–Riseman was determined to be the more favorable of the two models using this method of fitness testing. Moreover, the Kirkwood–Riseman model may serve as a better physical model for the proposed AuNP–vesicle binding scenario, where AuNP–vesicle affinity (heteroaggregation) may exceed that of either nanoparticles for themselves or vesicles for themselves (homoaggregation). The Kirkwood–Riseman analysis also overcomes the additive assumption used in the Stokes–Einstein model. Thus, model choice is an important consideration when applying mixture distributions to NTA data sets, and both the underlying assumptions of each model and model fitness should be carefully considered. In the case of the system studied here, the Kirkwood–Riseman model appears more suitable because the measured bound species does not appear to exceed a 1:2 AuNP:vesicle ratio, beyond which the bound species might depart more

considerably from the underlying linear chain binding assumption of this model. By the Kirkwood–Riseman model, the presence of gA peptide was found to increase total binding by a factor of 3.8 times due to increases in both the attached (1:1 AuNP:Vesicle) and bridged (1:2 AuNP:Vesicle) binding configurations. The application of mixture distributions to NTA analysis can thus provide a quantitative description about proportion bound in varying particle binding configurations, information that is not otherwise possible to obtain via NTA or DLS alone.

### 3.5 Tables and Figures

**Table 1.** Hydrodynamic and electrokinetic properties of the gold nanoparticles (AuNPs) and lipid vesicles.<sup>a</sup>

Sample	Hydrodynamic Diameter (nm)				
	Dynamic Light Scattering			NTA Number- average	$\zeta$ -Potential (mV)
	Z- average	Number- average	PDI <sup>b</sup>		
MPA-AuNPs	90 ± 14	60 ± 17	0.22 ± 0.01	83 ± 1.5	-25.0 ± 1.4
DPhPC	135 ± 0.9	90 ± 10	0.12 ± 0.01	112 ± 1.9	-3.0 ± 0.9
DPhPC + MPA-AuNPs	156 ± 1.0	97 ± 9.4	0.20 ± 0.01	114 ± 5.0	-2.1 ± 0.6
DPhPC + gA	129 ± 1.2	78 ± 8.3	0.17 ± 0.01	120 ± 36	-3.6 ± 0.7
DPhPC + gA + MPA- AuNPs	189 ± 4.9	120 ± 18	0.23 ± 0.01	150 ± 54	-3.3 ± 0.2

<sup>a</sup> Values presented as a mean ± for three replicates of a single sample.

<sup>b</sup> Polydispersity Index (PDI), a measure of heterogeneity in hydrodynamic diameters.

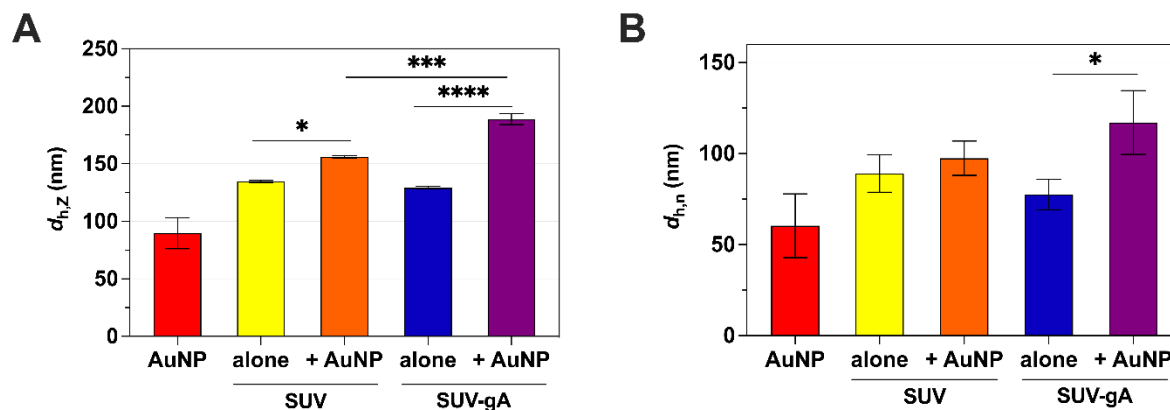


**Figure 1.** Average hydrodynamic diameters ( $d_h$ ) of MPA-AuNPs, DPhPC vesicles (alone or incorporating gramicidin A (gA), and AuNPs interacting with vesicles as determined by dynamic light scattering (DLS). (A) Z-average hydrodynamic diameter ( $d_{h,z}$ ) indicating that anionic MPA-AuNPs bind to vesicles both lacking and containing gA. (B) Number-average diameter ( $d_{h,n}$ ) showing a size change ( $p < 0.05$ ) resulting only from interaction of MPA-AuNPs with gA-containing vesicles

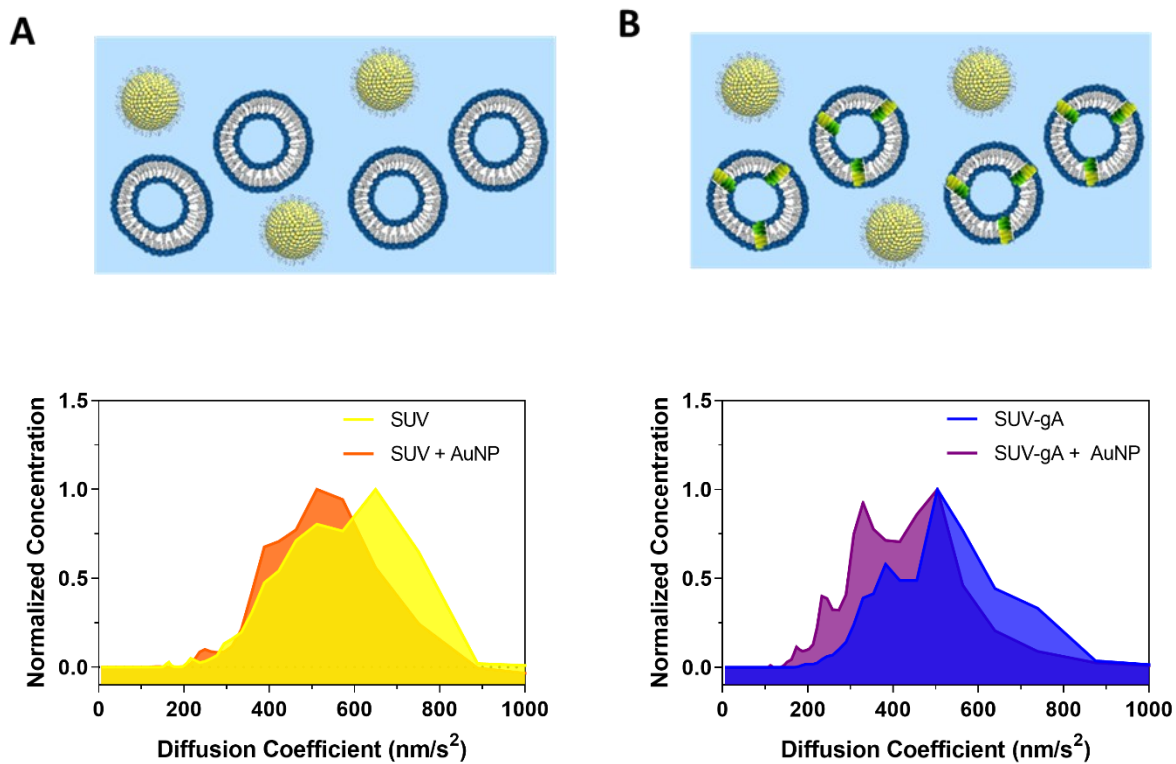


**Figure 2.** Representative histograms of particle diffusion coefficients measured by NTA for a single replicate of each sample, normalized to maximum concentration. (A) DPhPC vesicles with and without addition of MPA-AuNPs and (B) DPhPC + gA vesicles with and without addition of MPA-AuNPs, both showing shifts in diffusion coefficients upon addition of MPA-AuNPs that justify further, more detailed analysis of NTA data.

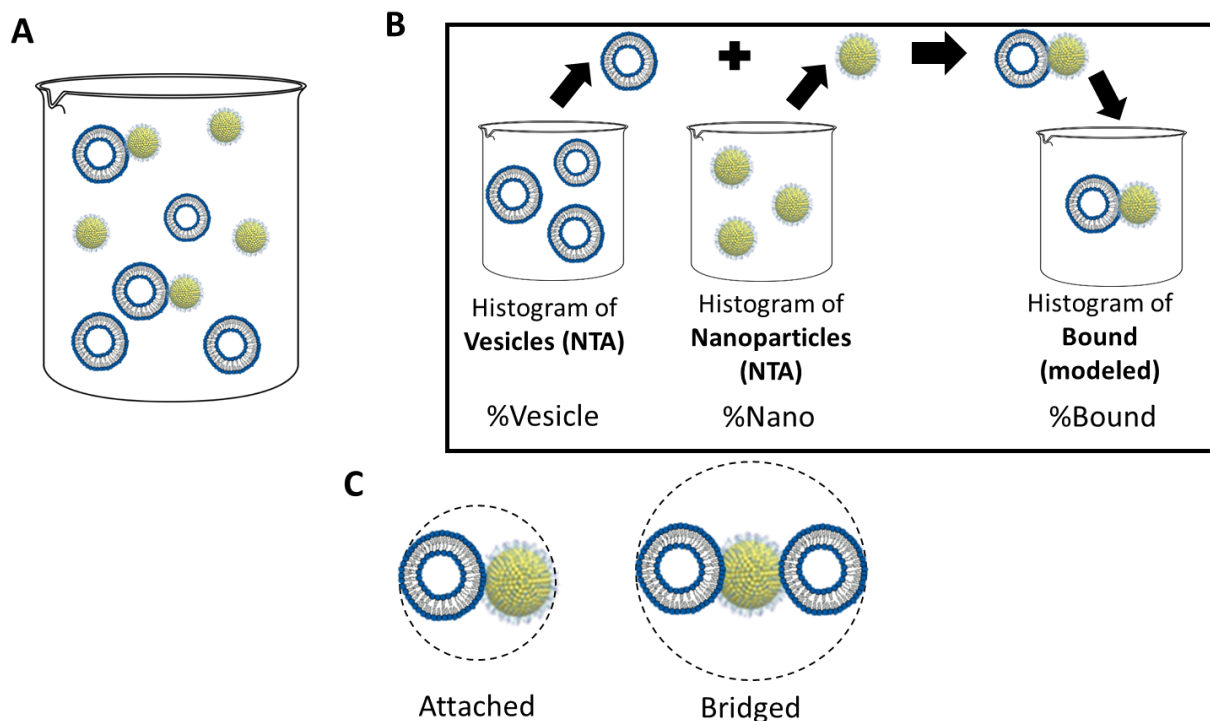


**Figure 3.** Schematic depicting the concept of mixture distributions as applied to a nanoparticle-vesicle system where (A) vesicles, nanoparticles, and bound AuNP–vesicle species all exist in solution and (B) mixture distribution analysis is applied by drawing vesicle and nanoparticle sizes from NTA measurements, and AuNP–vesicle bound species are artificially formed using either the Stokes–Einstein (SE) or Kirkwood–Riseman (KR) models to generate a third modeled histogram of bound species that closely matches the measured histogram for AuNP + vesicle. Two possible binding scenarios and their SE hydration spheres are depicted in (C) a 1:1 AuNP:Vesicle ratio or a 1:2 AuNP:Vesicle ratio based on the excess of vesicles present in solution relative to the AuNP concentration.

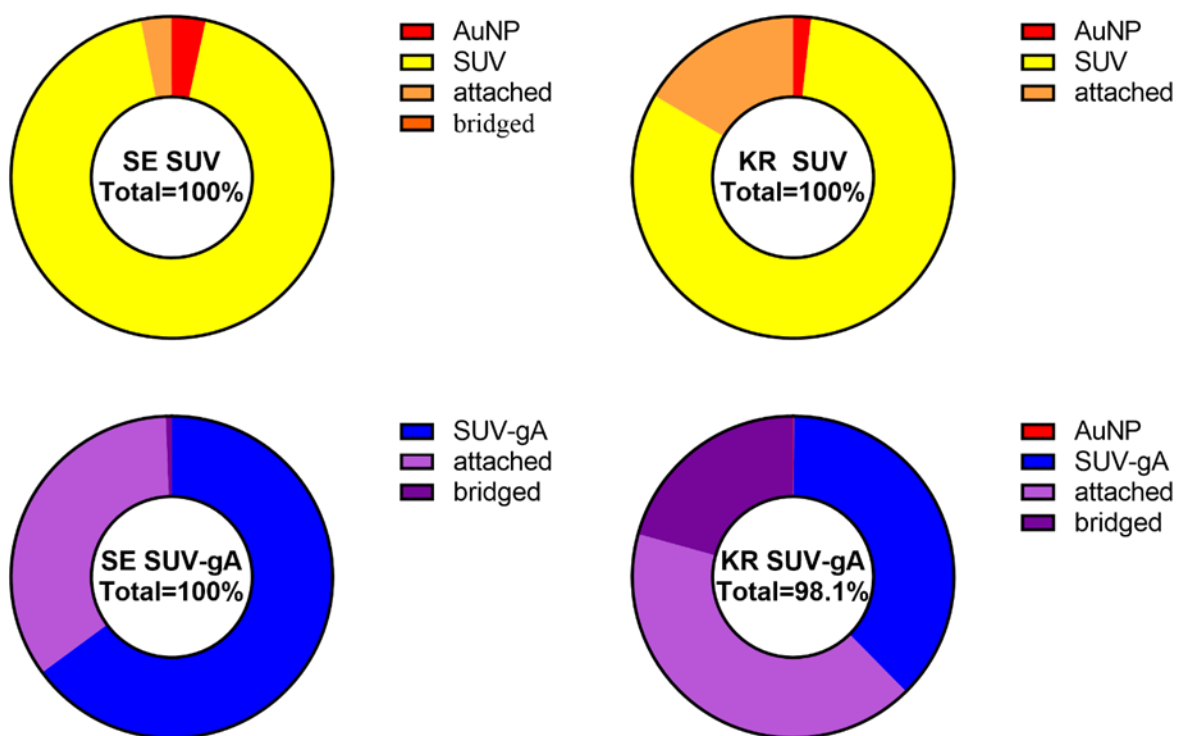


**Figure 4.** Comparison of gold nanoparticle (AuNP)–small unilamellar vesicle (SUV) binding using the (A, C) Stokes–Einstein (SE) and (B, D) Kirkwood–Riseman (KR) models for (A, B) SUVs and (C, D) vesicles containing gramicidin A (SUV-gA), where “attached” indicates 1:1 AuNP:vesicle and “bridged” denotes 1:2 AuNP:vesicle binding ratios. Percentages denoted in the middle of each chart indicate the percent of the measured population explained by each analysis (e.g., KR analysis of SUV-gA population accounts for 98.1% of the measured species).

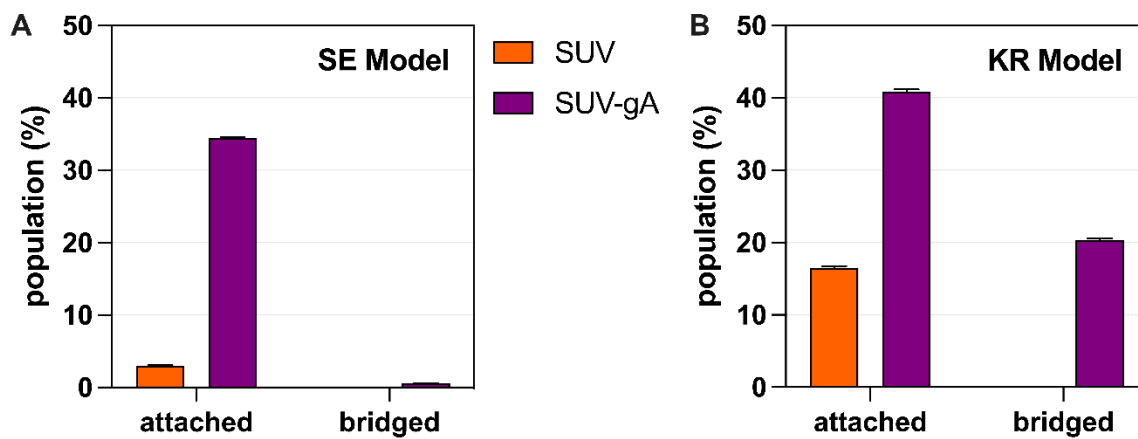


**Figure 5.** Population of attached (1:1 AuNP:vesicle) versus bridged (1:2 AuNP:vesicle) species based on application of the (A) Stokes–Einstein (SE) or (B) Kirkwood–Riseman (KR) model in the statistical mixture distribution analysis of NTA data. Bars represent mean values calculated at the 95% confidence interval; error bars represent upper and lower bounds.

### 3.6 References

- (1) James, A. E.; Driskell, J. D. Monitoring Gold Nanoparticle Conjugation and Analysis of Biomolecular Binding with Nanoparticle Tracking Analysis (NTA) and Dynamic Light Scattering (DLS). *Analyst* **2013**, *138* (4), 1212–1218. <https://doi.org/10.1039/c2an36467k>.
- (2) Kim, A.; Ng, W. B.; Bernt, W.; Cho, N. J. Validation of Size Estimation of Nanoparticle Tracking Analysis on Polydisperse Macromolecule Assembly. *Sci. Rep.* **2019**, *9* (1), 1–14. <https://doi.org/10.1038/s41598-019-38915-x>.
- (3) Yang, D.; Lu, X.; Fan, Y.; Murphy, R. M. Evaluation of Nanoparticle Tracking for Characterization of Fibrillar Protein Aggregates. *AIChE* **2014**, *60* (4), 1236–1244. <https://doi.org/10.1002/aic>.
- (4) Filipe, V.; Hawe, A.; Jiskoot, W. Critical Evaluation of Nanoparticle Tracking Analysis (NTA) by NanoSight for the Measurement of Nanoparticles and Protein Aggregates. *Pharm. Res.* **2010**, *27* (5), 796–810. <https://doi.org/10.1007/s11095-010-0073-2>.
- (5) Dragovic, R. A.; Gardiner, C.; Brooks, A. S.; Tannetta, D. S.; Ferguson, D. J. P.; Hole, P.; Carr, B.; Redman, C. W. G.; Harris, A. L.; Dobson, P. J.; Harrison, P.; Sargent, I. L. Sizing and Phenotyping of Cellular Vesicles Using Nanoparticle Tracking Analysis. *Nanomedicine Nanotechnology, Biol. Med.* **2011**, *7* (6), 780–788. <https://doi.org/10.1016/j.nano.2011.04.003>.
- (6) Bell, N. C.; Minelli, C.; Tompkins, J.; Stevens, M. M.; Shard, A. G. Emerging Techniques for Submicrometer Particle Sizing Applied to Stöber Silica. *Langmuir* **2012**, *28* (29), 10860–10872. <https://doi.org/10.1021/la301351k>.
- (7) Sanchez, N.; Soulet, D.; Bonnet, E.; Guinchard, F.; Marco, S.; Vetter, E.; Nougarede, N. Rabies Vaccine Characterization by Nanoparticle Tracking Analysis. *Sci. Rep.* **2020**, *10* (1), 1–8. <https://doi.org/10.1038/s41598-020-64572-6>.
- (8) Kestens, V.; Bozatzidis, V.; De Temmerman, P. J.; Ramaye, Y.; Roebben, G. Validation of a Particle Tracking Analysis Method for the Size Determination of Nano- and Microparticles. *J. Nanoparticle Res.* **2017**, *19* (8). <https://doi.org/10.1007/s11051-017-3966-8>.
- (9) van der Pol, E.; Coumans, F. A. W.; Grootemaat, A. E.; Gardiner, C.; Sargent, I. L.; Harrison, P.; Sturk, A.; van Leeuwen, T. G.; Nieuwland, R. Particle Size Distribution of Exosomes and Microvesicles Determined by Transmission Electron Microscopy, Flow Cytometry, Nanoparticle Tracking Analysis, and Resistive Pulse Sensing. *J. Thromb. Haemost.* **2014**, *12* (7), 1182–1192. <https://doi.org/10.1111/jth.12602>.
- (10) Wang, B.; Zhang, L.; Sung, C. B.; Granick, S. Nanoparticle-Induced Surface Reconstruction of Phospholipid Membranes. *Proc. Natl. Acad. Sci. U. S. A.* **2008**, *105* (47), 18171–18175. <https://doi.org/10.1073/pnas.0807296105>.
- (11) Moghadam, B. Y.; Hou, W.-C.; Corredor, C.; Westerhoff, P.; Posner, J. D. The Role of Nanoparticle Surface Functionality in the Disruption of Model Cell Membranes. *Langmuir* **2012**, *28* (47), 16318–16326. <https://doi.org/10.1038/jid.2014.371>.

- (12) Akbarzadeh, A.; Rezaei-Sadabady, R.; Davaran, S.; Joo, S. W.; Zarghami, N.; Hanifehpour, Y.; Samiei, M.; Kouhi, M.; Nejati-Koshki, K. Liposome: Classification, Preparation, and Applications. *Nanoscale Res. Lett.* **2013**, *8* (1), 1–8. <https://doi.org/10.1186/1556-276X-8-102>.
- (13) Rideau, E.; Dimova, R.; Schwille, P.; Wurm, F. R.; Landfester, K. Liposomes and Polymersomes: A Comparative Review towards Cell Mimicking. *Chem. Soc. Rev.* **2018**, *47* (23), 8572–8610. <https://doi.org/10.1039/c8cs00162f>.
- (14) Cheng, L.-C.; Jiang, X.; Wang, J.; Chen, C.; Liu, R.-S. Nano-Bio Effects: Interaction of Nanomaterials with Cells. *Nanoscale* **2013**, *5* (9), 3547–3569. <https://doi.org/10.1039/c3nr34276j>.
- (15) Dante, S.; Petrelli, A.; Petrini, E. M.; Marotta, R.; Maccione, A.; Alabastri, A.; Quarta, A.; De Donato, F.; Ravasenga, T.; Sathya, A.; Cingolani, R.; Proietti Zaccaria, R.; Berdondini, L.; Barberis, A.; Pellegrino, T. Selective Targeting of Neurons with Inorganic Nanoparticles: Revealing the Crucial Role of Nanoparticle Surface Charge. *ACS Nano* **2017**, *11* (7), 6630–6640. <https://doi.org/10.1021/acsnano.7b00397>.
- (16) Ventola, C. L.; Bharali, D. J.; Mousa, S. A. The Nanomedicine Revolution: Part 1: Emerging Concepts. Pharmacy and Therapeutics. *Pharmacol. Ther.* **2010**, *128* (9), 512–525. <https://doi.org/10.1016/j.pharmthera.2010.07.007>.
- (17) Jiang, W.; Yang, K.; Vachet, R. W.; Xing, B. Interaction between Oxide Nanoparticles and Biomolecules of the Bacterial Cell Envelope as Examined by Infrared Spectroscopy. *Langmuir* **2010**, *26* (23), 18071–18077. <https://doi.org/10.1021/la103738e>.
- (18) Bozich, J.; Hang, M.; Hamers, R. J.; Klaper, R. Core Chemistry Influences the Toxicity of Multicomponent Metal Oxide Nanomaterials, Lithium Nickel Manganese Cobalt Oxide, and Lithium Cobalt Oxide to *Daphnia Magna*. *Environ. Toxicol. Chem.* **2017**, *36* (9), 2493–2502.
- (19) Maurer-Jones, M. A.; Gunsolus, I. L.; Murphy, C. J.; Haynes, C. L. Toxicity of Engineered Nanoparticles in the Environment. *Anal. Chem.* **2013**, *85* (6), 3036–3049. <https://doi.org/10.1021/ac303636s>.
- (20) Nel, A. E.; Mädler, L.; Velegol, D.; Xia, T.; Hoek, E. M. V.; Somasundaran, P.; Klaessig, F.; Castranova, V.; Thompson, M. Understanding Biophysicochemical Interactions at the Nano-Bio Interface. *Nat. Mater.* **2009**, *8* (7), 543–557. <https://doi.org/10.1038/nmat2442>.
- (21) Foreman-Ortiz, I. U.; Liang, D.; Laudadio, E. D.; Calderin, J. D.; Wu, M.; Keshri, P.; Zhang, X.; Schwartz, M. P.; Hamers, R. J.; Rotello, V. M.; Murphy, C. J.; Cui, Q.; Pedersen, J. A. Anionic Nanoparticle-Induced Perturbation to Phospholipid Membranes Affects Ion Channel Function. *Proc. Natl. Acad. Sci. U. S. A.* **2020**, *117* (45), 27854–27861. <https://doi.org/10.1073/pnas.2004736117>.
- (22) Bozich, J. S.; Lohse, S. E.; Torelli, M. D.; Murphy, C. J.; Hamers, R. J.; Klaper, R. D. Surface Chemistry, Charge and Ligand Type Impact the Toxicity of Gold Nanoparticles to *Daphnia Magna*. *Environ. Sci. Nano* **2014**, *1* (3), 260–270. <https://doi.org/10.1039/C4EN00006D>.

- (23) Haiss, W.; Thanh, N. T. K.; Aveyard, J.; Fernig, D. G. Determination of Size and Concentration of Gold Nanoparticles from UV-Vis Spectra. *Anal. Chem.* **2007**, *79* (11), 4215–4221. <https://doi.org/10.1021/ac0702084>.
- (24) Mayer, L. D.; Hope, M. J.; Cullis, P. R. Vesicles of Variable Sizes Produced by a Rapid Extrusion Procedure. *BBA - Biomembr.* **1986**, *858* (1), 161–168. [https://doi.org/10.1016/0005-2736\(86\)90302-0](https://doi.org/10.1016/0005-2736(86)90302-0).
- (25) S. Melby, E.; Allen, C.; U. Foreman-Ortiz, I.; R. Caudill, E.; R. Kuech, T.; M. Vartanian, A.; Zhang, X.; J. Murphy, C.; Hernandez, R.; A. Pedersen, J. Peripheral Membrane Proteins Facilitate Nanoparticle Binding at Lipid Bilayer Interfaces. *Langmuir* **2018**, *34* (36), 10793–10805. <https://doi.org/10.1021/acs.langmuir.8b02060>.
- (26) Hunter, D. G.; Frisken, B. J. Effect of Extrusion Pressure and Lipid Properties on the Size and Polydispersity of Lipid Vesicles. *Biophys. J.* **1998**, *74* (6), 2996–3002. [https://doi.org/10.1016/S0006-3495\(98\)78006-3](https://doi.org/10.1016/S0006-3495(98)78006-3).
- (27) Chattopadhyay, A.; Rawat, S. S.; Greathouse, D. V.; Kelkar, D. A.; Koeppe, R. E. Role of Tryptophan Residues in Gramicidin Channel Organization and Function. *Biophys. J.* **2008**, *95* (1), 166–175. <https://doi.org/10.1529/biophysj.107.124206>.
- (28) Rawat, S. S.; Kelkar, D. A.; Chattopadhyay, A. Monitoring Gramicidin Conformations in Membranes: A Fluorescence Approach. *Biophys. J.* **2004**, *87* (2), 831–843. <https://doi.org/10.1529/biophysj.104.041715>.
- (29) Gallego-Urrea, J. A.; Tuoriniemi, J.; Hassellöv, M. Applications of Particle-Tracking Analysis to the Determination of Size Distributions and Concentrations of Nanoparticles in Environmental, Biological and Food Samples. *TrAC - Trends Anal. Chem.* **2011**, *30* (3), 473–483. <https://doi.org/10.1016/j.trac.2011.01.005>.
- (30) Hoover, B. M.; Murphy, R. M. Evaluation of Nanoparticle Tracking Analysis for the Detection of Rod-Shaped Particles and Protein Aggregates. *J. Pharm. Sci.* **2019**, *109* (1), 452–463. <https://doi.org/10.1016/j.xphs.2019.10.006>.
- (31) Elimelech, M.; Gregory, J.; Jia, X.; Williams, R. A. *Particle Deposition and Aggregation*; Butterworth-Heinemann: Woburn, MA, 1995. <https://doi.org/https://doi.org/10.1016/B978-0-7506-7024-1.X5000-6>.
- (32) Stetefeld, J.; McKenna, S. A.; Patel, T. R. Dynamic Light Scattering: A Practical Guide and Applications in Biomedical Sciences. *Biophys. Rev.* **2016**, *8* (4), 409–427. <https://doi.org/10.1007/s12551-016-0218-6>.
- (33) Pamies, R.; Cifre, J. G. H.; Espín, V. F.; Collado-González, M.; Baños, F. G. D.; De La Torre, J. G. Aggregation Behaviour of Gold Nanoparticles in Saline Aqueous Media. *J. Nanoparticle Res.* **2014**, *16* (4). <https://doi.org/10.1007/s11051-014-2376-4>.
- (34) Gu, C. Smoothing Spline ANOVA Models: R Package Gss. *J. Stat. Softw.* **2014**, *58* (5), 1–25. <https://doi.org/10.18637/jss.v058.i05>.
- (35) Dempster, A. P.; Laird, N. M.; Rubin, D. B. Maximum Likelihood from Incomplete Data via the EM Algorithm. *J. R. Stat. Soc. Ser. B* **1977**, *39* (1), 1–38.

- (36) Kirkwood, J. G.; Riseman, J. The Intrinsic Viscosities and Diffusion Constants of Flexible Macromolecules in Solution. *J. Chem. Phys.* **1948**, *16* (6), 565–573. <https://doi.org/10.1063/1.1746947>.
- (37) Edward, J. T. Molecular Volumes and the Stokes-Einstein Equation. *J. Chem. Educ.* **1970**, *47* (4), 261–270. <https://doi.org/10.1021/ed047p261>.
- (38) Efron, B.; Tibshirani, R. J. *An Introduction to the Bootstrap*; Chapman and Hall, 1993.
- (39) D'Agostino, R. B.; Stephens, M. A. Goodness-of-Fit-Techniques. In *Chapter 4*; 1986; pp 97–193.
- (40) R Core Team. R: A Language and Environment for Statistical Computing. R Foundation for Statistical Computing: Vienna, Austria 2018.
- (41) Dempster, A. P.; Laird, N. M.; Rubin, D. B. *Maximum Likelihood from Incomplete Data Via the EM Algorithm*; 1977; Vol. 39. <https://doi.org/10.1111/j.2517-6161.1977.tb01600.x>.
- (42) Evans, R.; Dal Poggetto, G.; Nilsson, M.; Morris, G. A. Improving the Interpretation of Small Molecule Diffusion Coefficients. *Anal. Chem.* **2018**, *90* (6), 3987–3994. <https://doi.org/10.1021/acs.analchem.7b05032>.
- (43) Stepto, R. Interpretation of the Effects of Segmental Friction on the Diffusion Coefficients of Polymer Chains. *Die Makromol. Chemie* **1989**, *190* (3), 549–557. <https://doi.org/10.1002/macp.1989.021900311>.

## Chapter 4: Anionic nanoparticles impact lipid packing in vesicles

The following co-authors have contributed to this work: Yuanya Zhao, Brenda Gonzales, Meng Wu, Puspam Keshri, Xianzhi Zhang, Chandler B. Est, Regina Murphy, Vincent M. Rotello, and

Joel A. Pedersen

### 4.1 Introduction

Cell membrane properties such as lipid packing (lateral mobility) and lipid organization are known to impact the structure and function of embedded membrane proteins,<sup>1-5</sup> which can lead to effects on cellular function.<sup>1,2</sup> Lipid packing in membranes is dictated by the structural features of constituent species and interactions with the surrounding environment.<sup>6-9</sup> Longer chain lipids have more surface area to interact with neighboring lipids, resulting in stronger Van der Waals interactions between lipids and tighter lipid packing.<sup>6,7</sup> Unsaturated lipids can form kinks that reduce lipid packing by decreasing Van der Waals interactions between lipids.<sup>6,7</sup> Other membrane constituents like sterols can accumulate in the lipid bilayer leaflet, leading to tighter packing.<sup>8,10</sup> The ionic strength of the surrounding solution can also influence lipid packing through charge screening, which increases electrostatic interaction between lipid headgroups, leading to closer lipid packing.<sup>11,12</sup> Lipid packing dictates the function of the cell membrane through phase separation and membrane protein aggregation<sup>13</sup>, or membrane leakage.<sup>14</sup>

Previous work reported in Chapter 2 has shown that exposure to anionic NPs may induce changes in lipid packing that impact the function of embedded ion channels.<sup>15</sup> Computational assessment within this work suggested that anionic NPs may bind to a zwitterionic lipid bilayer and induce local areas of increased lipid packing that weaken interactions between neighboring lipids and cause softening outside of the direct NP-bound area.<sup>15</sup> Such altered lipid packing and

extended softening would lead to the observed increased lifetime of ion channel dimers due to lowered membrane compressibility.<sup>15</sup>

Membrane-segregating dyes have been employed to gain insight on lipid packing in membranes.<sup>16–18</sup> One such dye is Laurdan, a lipophilic probe which is sensitive to both the polarity of the medium in which the fluorophore resides (environment) and dipolar relaxation of surrounding molecules.<sup>17</sup> The fluorescence of Laurdan arises from charge separation in the headgroup, which aligns with phospholipid headgroups when incorporated into a lipid bilayer, as depicted in Figure 1.<sup>9,19</sup> The Laurdan dipole moment increases with excitation by light, causing reorientation of surrounding solvent molecule dipoles (usually water).<sup>17</sup> The energy required for solvent dipole reorientation then decreases the energy of the Laurdan excited state, leading to a red shift in the Laurdan emission spectrum.<sup>9,19</sup> The penetration of water molecules to the Laurdan headgroup depends on lipid packing – a more “rigid” bilayer will allow less water penetration and demonstrate less of a red shifted emission spectrum than a “fluid”, or more loosely-packed lipid bilayer (Figure 1). Thus, Laurdan is sensitive to lipid packing, often referred to as rigidity, within the membrane.<sup>17</sup>

Due to its sensitivity to lipid packing, Laurdan can be used to detect the presence of gel (packed) versus liquid-crystalline (fluid, less packed) phases within lipid membranes.<sup>19–22</sup> The transition between ordered gel and disordered liquid-crystalline phases is controlled by temperature – above the phase transition temperature characteristic of the constituent lipid, membranes exist in the liquid-crystalline (fluid) phase. Thus, Laurdan can be used to observe phase transitions in single component or mixtures of lipids.<sup>17,19,20,23</sup> Laurdan is also sensitive to changes in the polarity of its environment – exposure to a polar environment causes enhancement of the Laurdan dipole moment, which results in a decreased fluorescence lifetime<sup>9</sup> and a peak

shift in the fluorescence spectrum.<sup>24</sup> The approximate alignment of Laurdan with surrounding phospholipids<sup>9</sup> and the Laurdan head group exposure to solvent based on lipid packing is depicted in Figure 1.

Laurdan has been employed extensively to study the impact of membrane composition<sup>9,17,19,21,22,25,26</sup>, incubation temperature<sup>17,19,22,25</sup>, and exposure to membrane-interacting species such as Ca<sup>2+</sup> and Na<sup>+</sup> on lipid packing in vesicles.<sup>26</sup> Studies on model membranes often employ a generalized polarization (GP) equation to compare membrane packing between samples. Generalized polarization (GP) is a measure of Laurdan emission peak characteristics and is typically defined as follows<sup>17</sup>, although some systems may use different wavelength regions<sup>23,27</sup>:

$$\text{Generalized Polarization (GP)} = \frac{I_{440} - I_{490}}{I_{440} + I_{490}} \quad \text{Equation 1}$$

Where  $I_{440}$  and  $I_{490}$  represent the fluorescence intensity at 440 and 490 nm, respectively. An increase in membrane water penetration resulting from decreased lipid packing is associated with a red shift in the Laurdan fluorescence peak.<sup>17</sup> The GP would then increase with lipid packing, such that a more positive GP indicates increased lipid packing.

The Laurdan and GP system has been previously applied to study the impact of nanoparticles on model membrane systems. Charged polystyrene nanoparticles (NPs) can induce changes in lipid packing in zwitterionic vesicles, with cationic NPs inducing fluidization of gel-phase membranes and anionic NPs causing gelation of fluid-phase membranes.<sup>16</sup> Moreover, a combined Laurdan fluorescence and atomic force microscopy (AFM) membrane study indicated that anionic gold nanoparticles may induce effects similar to those observed previously<sup>15</sup> – local stiffening of the bilayer which causes membrane softening in areas extending past the NP.<sup>28</sup>

Previous studies provide motivation for further characterization of anionic nanoparticle-induced

alteration to lipid packing.<sup>15</sup> The Laurdan GP system provides a simpler and faster measure (than the electrophysiology previously characterized<sup>15</sup>) of alterations in membrane mechanical properties that may impact the function of embedded ion channels. For this reason, Laurdan GP measurements can be easily and quickly extended to study vesicle systems of varying lipid composition and solution ionic strength to study the impact of these factors on the extent of NP-induced lipid packing changes.

Here, we employ the membrane-segregating dye Laurdan to study changes in lipid packing of zwitterionic vesicles in response to exposure to two anionic gold NP types bearing different ligands. Moreover, we assess the impact of nanoparticle aggregation and charge, as well as degree of bilayer rigidity on the extent of the anionic NP effect. We found that degree of anionic charge and aggregation state of NPs may both impact the extent of impact on lipid packing. Moreover, we found that anionic NPs demonstrate more impact on lipid packing in fluid than rigid vesicles. These results support computational studies which suggested that anionic NP exposure may alter the function of embedded ion channel function by increasing local lipid packing<sup>15</sup> and provide further insight into the effect of lipid rigidity, salt concentration, and NP ligand type on anionic-NP induced effects on lipid packing.

## **4.2 Materials and Methods**

### **4.2.1 Materials**

We procured 3-mercaptopropionic acid (MPA), gold (III) chloride trihydrate (HAuCl<sub>4</sub>·3H<sub>2</sub>O), sodium hydroxide, Laurdan dye (6-Dodecanoyl-N,N-dimethyl-2-naphthylamine), and gramicidin A (gA) from Sigma Aldrich. Sodium borohydrate was acquired from Fluka. Buffers were made using potassium chloride and 4-(2-hydroxyethyl)-1-piperazineethanesulfonic acid (HEPES) from Dot Scientific. We obtained 1,2-diphytanoyl-sn-glycero-3-phosphocholine (DPhPC: 4ME 16:0

PC) and 1,2-dioleoyl-sn-glycero-3-phosphocholine (18:1 ( $\Delta^9$ -Cis) PC) in chloroform from Avanti Polar Lipids (Alabaster, AL).

#### 4.2.2 Ligand and gold nanoparticle synthesis

The production of 3-mercaptopropionic acid (MPA) AuNPs and TCOOH-AuNPs is identical to that outlined previously.<sup>15</sup> Briefly, MPA-AuNPs were synthesized using an existing protocol<sup>29</sup> where HAuCl<sub>4</sub> (3.53 mL, 0.1 M) and 450 mL ultrapure water were combined in an Erlenmeyer flask, then adding 212  $\mu$ L of 0.1 M MPA. Following adjustment of the pH to  $\sim$ 8.5 using 1 M NaOH, 6.4 mL of 0.1 M NaBH<sub>4</sub> was added and the solution was stirred for 2 h. A customized flow reactor with a 30 kDa MWCO membrane was then used to concentrate the MPA-AuNPs to a volume of  $\sim$ 30 mL.<sup>30</sup> Purification of the particles was performed using centrifugation at 13,000 g for 55 min (2x). Sample preparation for TEM imaging involved drop casting 5  $\mu$ L of MPA-AuNPs onto a TEM grid (Ted Pella) followed by measurement using a JEOL 2100 cryo TEM.

The TCOOH ligand was synthesized as described previously.<sup>15</sup> Gold nanoparticles used to form TCOOH-AuNPs were synthesized by a Brust-Schiffrin two-phase method<sup>15</sup> followed by a ligand exchange, performed by dissolving 40 mg of gold core in 4 mL of DCM under argon and adding TCOOH ligand (120 mg) in 2 mL DCM and 2 mL of MeOH. The following solution was stirred at room temperature for 72 h. Remaining solvent was then evaporated using reduced pressure, followed by three washes using hexane and hexane/DCM (1:1 v/v) rinses. This process resulted in the formation of a solid, which was then dissolved in ultrapure water and dialyzed for purification for 3 days. TEM measurements were performed as described previously.<sup>15</sup> The structure of MPA- and TCOOH- ligands are presented in Figure 2.

### 4.2.3 Characterization of gold nanoparticles

The TEM and UV-Vis characterization of gold nanoparticles is identical to that presented previously.<sup>15</sup> Electrophoretic mobility measurements of MPA- and TCOOH-AuNPs were previously collected in high salt (0.15 M KCl buffered to pH 7.4 with 0.01 M HEPES) and used to calculate apparent NP  $\zeta$ -potentials. MPA-AuNPs were characterized in low salt (1 mM KCl buffered to pH 7.4 with 0.01 M HEPES) as an average of five replicates. The  $\zeta$ -potential standard deviations represent the variation among replicates. Dynamic light scattering (DLS) measurements of AuNPs in low salt resulted in particle size distributions that were too polydisperse to apply cumulants analysis, so nanoparticle hydrodynamic diameters were additionally characterized using nanoparticle tracking analysis (NTA), as depicted in Table 1. Briefly, nanoparticles were diluted to concentrations in the  $10^7$ - $10^9$  particle  $\cdot$  mL<sup>-1</sup> range, and directly injected into the Nanosight LM10 (Nanosight, 405 nm laser) using Luer Lok syringes (BD). All measurements were performed instantly at room temperature. The NTA 3.0 software was used to analyze the number distribution of particle sizes, with a detection threshold of 4 to eliminate background noise and a camera level of 13 to avoid excess saturation. The particle hydrodynamic diameters measured using NTA are summarized in Table 1.

### 4.2.4 Preparation and characterization of small unilamellar vesicles

Vesicles (with or without incorporated Laurdan dye) were formed using the extrusion method.<sup>31</sup> First, 1 mM of lipids was prepared, to which 0.01 mM Laurdan in methanol is added for some samples. Solvent (chloroform) is then removed by evaporation under nitrogen, until visibly dry. Samples were then dried under vacuum for several hours to ensure complete removal of solvent. Buffered solutions containing low (1 mM KCl buffered to pH 7.4 with 0.01 M HEPES) or high salt (0.15 M KCl buffered to pH 7.4 with 0.01 M HEPES) were added, followed

by mixing via vortex for 4 minutes. Lipid solutions then sat in the dark for 30 minutes to ensure incorporation of lipophilic Laurdan molecules into the vesicles. Samples were then extruded through a 50 nm polycarbonate filter (Whatman) 11 times using an extrusion kit (Avanti Polar Lipids). The resulting vesicle solutions were stored at 4 °C and used within 24 hours of production. Vesicle hydrodynamic diameters and  $\zeta$ -potentials were determined using dynamic light scattering (DLS) and laser Doppler electrophoresis (Malvern Zetasizer Nano ZS). The hydrodynamic diameters and  $\zeta$ -potentials reported in Table 2 are the means of three and five replicates, respectively.

#### **4.2.5 Laurdan fluorescence generalized polarization (GP) measurements**

Laurdan fluorescence was excited at 370 nm and emission was collected between 400 and 560 nm. All fluorescence experiments were performed using an ISS K2 spectrofluorimeter equipped with a neutral density ND05 filter. In order to mitigate potential spectral interference from AuNPs, the AuNPs were added to both reference and sample vials, where the reference fluorescence intensity is subtracted from the sample intensity to obtain the spectrum depicting the impact of AuNPs on Laurdan fluorescence alone. Reference vials thus contained vesicles lacking Laurdan as well as AuNPs, while sample vials consisted of Laurdan-containing vesicles and AuNPs. This referencing system helps to eliminate artifacts from AuNPs or vesicles themselves and isolate the effects of AuNPs on Laurdan-containing vesicles. Referencing in this manner was effective at removing the contribution of AuNPs, as the change in fluorescence when AuNPs are added to Laurdan-containing vesicles exceeds that of the AuNPs alone (at the wavelengths under study, 440 and 490 nm) by a factor of over 40.

Laurdan fluorescence spectra were used to generate generalized polarization (GP) values, the magnitude of which relates to the water penetration and thus extent packing of lipids in the

membrane. Higher (or more positive) GP values are associated with increased lipid packing (less water penetration), as calculated using Equation 1. Fluorescence measurements were performed in at least triplicate (triplicate for DOPC low and high salt experiments, triplicate for DPhPC high salt + TCOOH-AuNPs, and five replicates for DPhPC high salt + MPA-AuNPs), and the GP is an average of these values with propagated error and an associated standard deviation. Statistical significance was determined using an ordinary one-way ANOVA test with multiple comparisons (GraphPad Prism).

## **4.3 Results and Discussion**

### **4.3.1 Cholesterol content or Anionic MPA-AuNP Exposure Impact Lipid Packing**

Initial experiments to study the impact of anionic AuNPs on membrane packing focused on the DPhPC vesicle system in high salt (0.15 M KCl buffered to pH 7.4 with 0.01 M HEPES) previously used to characterize the impact of anionic AuNPs on ion channel activity.<sup>15</sup> Relatively few studies have employed the Laurdan GP system to assess the lipid packing properties of DPhPC membranes (structure depicted in Figure 1), with a focus placed on the effects of membrane compositional changes<sup>25,32</sup> rather than exposure to external species. Although DPhPC remains in the fluid phase over a broad temperature range (-120 °C to 120 °C), the presence of branched methyl sidechains (Figure 1) is known to decrease chain ordering by formation of kinks and reduce lateral diffusion of lipids<sup>33</sup>, resulting in higher membrane fluidity than conventional lipids lacking methyl sidechains<sup>33</sup>.

To assess the lipid packing properties of DPhPC, cholesterol (5 wt%) was first incorporated for comparison to a previous study demonstrating that a similar cholesterol content increases packing in DPhPC membranes by interdigitating with lipids.<sup>34</sup> Incorporation of 5 wt% cholesterol into DPhPC vesicles resulted in an increase in Laurdan GP, indicating an increase in

packing. This change is in qualitative agreement with the interdigitation of cholesterol in DPhPC membranes, which would induce tighter packing and subsequent reduced Laurdan solvent exposure.

With qualitative confirmation of Laurdan to test lipid packing using cholesterol, we then assessed the impact of anionic MPA-AuNP exposure to DPhPC vesicles. The addition of 5 nM MPA-AuNPs was also found to increase lipid packing, as evidenced by the increase in Laurdan GP (Figure 3). This observation is in agreement with previous studies demonstrating the ability of anionic nanoparticles to interact with zwitterionic lipid membranes<sup>15</sup> and induce areas of tighter lipid packing in fluid phase membranes due to reorientation of PC headgroups.<sup>16</sup> Although both cholesterol and MPA-AuNPs alter Laurdan GP, it is not trivial to draw conclusions when comparing the effects of AuNP exposure to increased cholesterol content, since cholesterol segregates into the lipid bilayer whereas AuNPs may bind to the surface of the membrane.<sup>15,16</sup>

#### **4.3.2 Less rigid vesicles are affected more by NP-induced lipid packing changes**

Next, we examined the impact of MPA-AuNPs on lipid packing in DOPC vesicles, for comparison to DPhPC vesicles. The structures and approximate alignment of Laurdan<sup>9</sup> with these lipids is depicted in Figure 1. Both lipids bear a zwitterionic phosphatidylcholine headgroup. However, the synthetic DPhPC contains branched methyl groups characteristic of *Archaeal* lipids.<sup>33</sup> The branched structure of DPhPC forms highly mechanically stable bilayer structures with low ion permeability that remains in the liquid crystalline (fluid) phase from  $-120$  °C to  $120$  °C<sup>35</sup>, whereas bilayers made of DOPC will remain fluid above  $-17$ °C.<sup>36</sup> Thus, at room temperature, both DOPC and DPhPC bilayers will be in the fluid phase.

We found that under similar high salt conditions (0.15 M KCl) and at room temperature, the MPA-AuNPs impacted the Laurdan GP of DPhPC vesicles more than that of DOPC vesicles

(Figure 4). This difference between vesicle types occurred despite no statistically significant difference in vesicle  $\zeta$ -potentials. The primary measurable difference between DOPC and DPhPC vesicles is the initial bilayer rigidity – DPhPC vesicles are found to have a more negative Laurdan GP than DOPC vesicles, indicating higher DOPC lipid packing. This is consistent with the suspected looser packing of DPhPC lipids in curved vesicles due to steric hindrance imparted by backbone methyl groups, and qualitatively agrees with previous studies demonstrating that branched methyl sidechains of constituent lipids can increase membrane fluidity.<sup>33,37</sup> Upon addition of MPA-AuNPs in high salt (0.15 M KCl), the initially ‘less packed’ DPhPC vesicles demonstrate a larger increase in packing than DOPC vesicles. Thus, the initial lipid packing properties of vesicles (as reflected in Laurdan GP of vesicles) may dictate the extent of NP-induced lipid packing changes.

#### **4.3.3 Aggregation state influences MPA-AuNP impact on lipid membranes**

To probe the effects of salt screening and NP aggregation, we compared the impact of anionic MPA-AuNPs on DOPC vesicles under low (1 mM KCl) versus high (0.15 M KCl) salt conditions. The apparent  $\zeta$ -potential of MPA-AuNPs is not observed to change considerably in low (1 mM KCl) vs high salt (0.15 M KCl) conditions. Using this metric alone, DOPC vesicles in high salt may more readily bind anionic MPA-AuNPs than in low salt based on electrostatic interaction. However, the lack of change in apparent  $\zeta$ -potentials may be caused by nanoparticle aggregation in high salt which leads to invalidation of the concept of zeta potential due to fluid flow through aggregates. Table 1 shows that MPA-AuNPs in high salt (0.15 M KCl) are more aggregated than those in low salt.

With a surface-interacting mechanism like that previously proposed for MPA-AuNP interactions with zwitterionic lipid bilayers<sup>15</sup>, less aggregated particles may exert a greater

impact on lipid packing by more distributed interaction with the bilayer. Since low and high salt experiments were performed using the same AuNP concentration (5 nM), low salt conditions lead to the presence of a higher number of less aggregated particles available for membrane surface interaction. These more abundant and smaller aggregates may distribute more evenly when interacting with the bilayer surface, leading to more measurable impact on lipid packing properties. Low salt conditions are indeed found to lead to increased impact of MPA-AuNPs on the Laurdan GP of DOPC vesicles, indicating that aggregation state may be an important factor in dictating alterations in lipid packing by AuNPs.

#### **4.3.4 Anionic NP-induced packing changes may be particle-dependent**

To determine if there are variations in the extent of lipid packing changes due to NP ligand structure, we also studied another AuNP type, the anionic TCOOH-AuNPs (Figure 2). Both AuNPs have carboxylate-bearing ligands (MPA and TCOOH) but differ in aggregation state and  $\zeta$ -potential. Due to their longer ligand structure, TCOOH-AuNPs particles aggregated to a lesser extent under high ionic strength conditions than MPA-AuNPs, although their apparent  $\zeta$ -potential was much less negative. Based on aggregation state alone, we might suspect that these TCOOH-AuNPs would exert a larger impact on lipid packing than MPA-AuNPs under similar high salt (0.15 M KCl) conditions. However, we found that TCOOH-AuNPs had no measurable impact on Laurdan GP (Figure 6). This is likely due to the significantly less negative apparent  $\zeta$ -potential of TCOOH-AuNPs than MPA-AuNPs, leading to decreased electrostatic interaction between phospholipid headgroups and AuNP. These data are consistent with electrophysiology studies which found reduced impact for TCOOH than MPA-AuNPs on bilayer interaction and subsequent ion channel disruption.<sup>15</sup> Although some effect was previously measurable for TCOOH-AuNP-induced ion channel disruption, the electrophysiology method

used to quantify channel currents may be more sensitive than the GP method, leading to no observable change when probed with Laurdan. The differences observed between nanoparticle ligand types demonstrates the need for a more comprehensive screening of nanoparticle properties with respect to Laurdan GP changes.

#### **4.4 Conclusions and implications**

We demonstrate that anionic AuNPs may induce an increase in lipid packing, as evidenced by fluorescence spectral changes of embedded Laurdan dye molecules. These studies further show that the extent of lipid packing changes may be dictated by NP ligand structure and surface charge, ionic strength that can alter particle aggregation state, and lipid vesicle composition. The increase in lipid packing observed upon exposure of zwitterionic membranes to anionic AuNPs is consistent with previous work demonstrating that anionic AuNPs alter the function of embedded ion channels through a membrane-mediated mechanism.<sup>15</sup> Thus, although the DPhPC Laurdan GP has been previously characterized to investigate the effects of binary lipid mixtures<sup>32</sup> and lipopolysaccharide concentration<sup>25</sup>, the study of the mechanical response of this lipid membrane yields useful comparisons to studies performed on suspended membrane systems to study ion channel function where DPhPC is often employed. In this way, the Laurdan GP method for studying lipid packing could serve as a supplementary method to corroborate membrane-mediated mechanisms in NP-induced perturbation of ion channel or membrane protein function. Future studies focusing on the effects of nanoparticle concentration on the magnitude of Laurdan GP could reveal its sensitivity to detecting changes in membrane mechanical properties relative to the alterations in ion channel function in electrophysiology measurements.

## 4.5 Tables and Figures

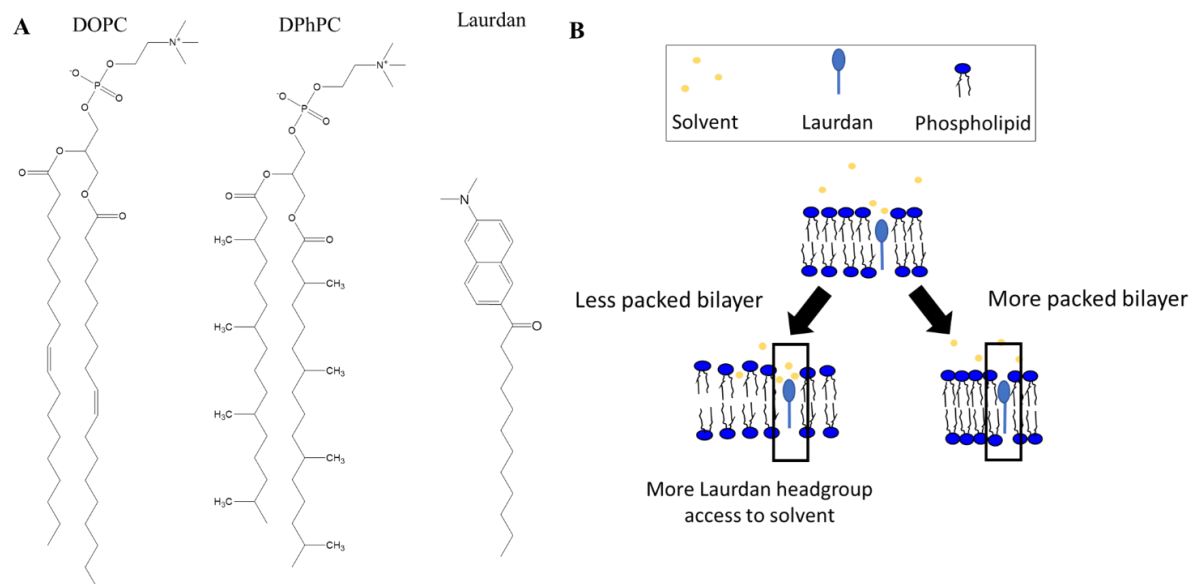


**Figure 1.** The (A) structures of DOPC, DPhPC, and Laurdan along with the approximate relative location of Laurdan when embedded beside phospholipids in a bilayer structure and (B) the alteration in Laurdan headgroup access to solvent as dictated by lipid packing.

**Table 1.** Apparent  $\zeta$ -potentials, NTA (Number average) hydrodynamic diameters, and PDI (via DLS) of MPA- and TCOOH-AuNPs in high (0.15 M KCl) and low (1 mM KCl) salt

AuNP Ligand Type	Salt Concentration	NTA Hydrodynamic Diameter (nm)	PDI (DLS)	Apparent $\zeta$ -potential (mV)
MPA	0.01 M KCl	$53 \pm 0.3$	$0.62 \pm 0.12$	$-30.1 \pm 7.8$
MPA	0.15 M KCl	$83 \pm 1.5$	$0.22 \pm 0.01$	$-25.0 \pm 1.4$
TCOOH	0.15 M KCl	$69 \pm 2.2$	$0.53 \pm 0.08$	$-8.9 \pm 0.40$

**Table 2.**  $\zeta$ -potentials and hydrodynamic diameters (via DLS) of DOPC and DPhPC vesicles with and without the inclusion of Laurdan dye in high and low salt concentrations

Vesicle Type	[KCl] (M)	Hydrodynamic Diameter		PDI	$\zeta$ -potential (mV)
		Number Average (nm)	Z-Average (nm)		
DOPC	0.01	87 $\pm$ 8.6	123 $\pm$ 1.0	0.11 $\pm$ 0.02	-6.8 $\pm$ 0.34
DOPC + Laurdan	0.01	92 $\pm$ 5.0	130 $\pm$ 0.7	0.11 $\pm$ 0.02	-5.2 $\pm$ 0.43
DOPC	0.15	92 $\pm$ 5.1	129 $\pm$ 2.2	0.11 $\pm$ 0.01	-3.7 $\pm$ 0.47
DOPC + Laurdan	0.15	96 $\pm$ 5.7	144 $\pm$ 3.7	0.14 $\pm$ 0.01	-3.5 $\pm$ 0.85
DPhPC	0.01	72 $\pm$ 1.5	147 $\pm$ 2.2	0.25 $\pm$ 0.01	14.3 $\pm$ 1.3
DPhPC + Laurdan	0.01	80 $\pm$ 10.0	148 $\pm$ 1.8	0.23 $\pm$ 0.02	11.3 $\pm$ 1.6
DPhPC	0.15	61 $\pm$ 10.0	121 $\pm$ 2.3	0.20 $\pm$ 0.04	-3.2 $\pm$ 0.40
DPhPC + Laurdan	0.01	67 $\pm$ 2.6	158 $\pm$ 1.2	0.28 $\pm$ 0.02	-2.7 $\pm$ 0.82

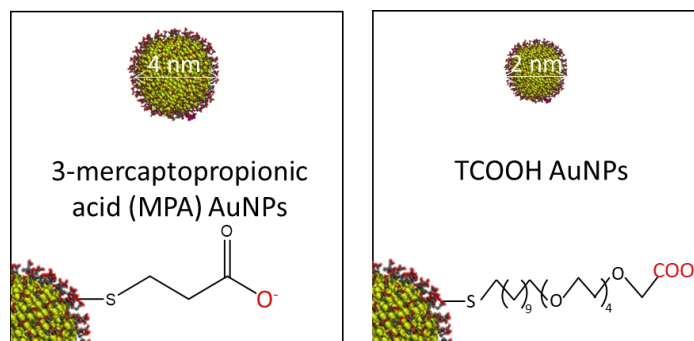


**Figure 2.** Structures and approximate core sizes of MPA- and TCOOH- ligands used for AuNP systems under study.

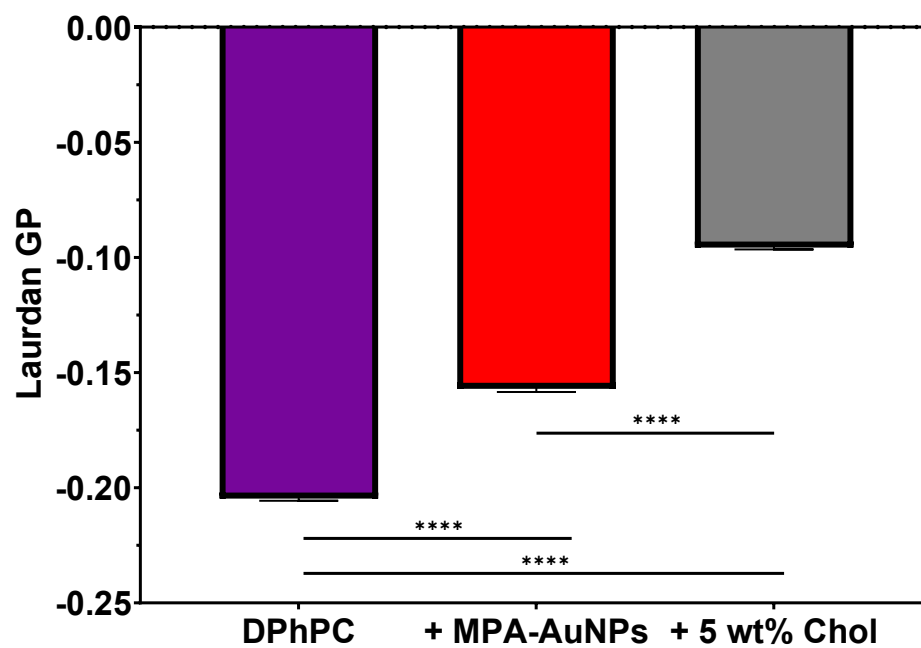


**Figure 3.** Cholesterol (5 wt%) and MPA-AuNPs (5 nM) impact lipid packing in DPhPC vesicles in high salt (0.15 M KCl), as reflected by a change in Laurdan GP. Error bars represent the standard deviation between replicates ( $n = 5$ ). Statistical significance is denoted by asterisks:  $P < 0.0001$  (\*\*\*\*).

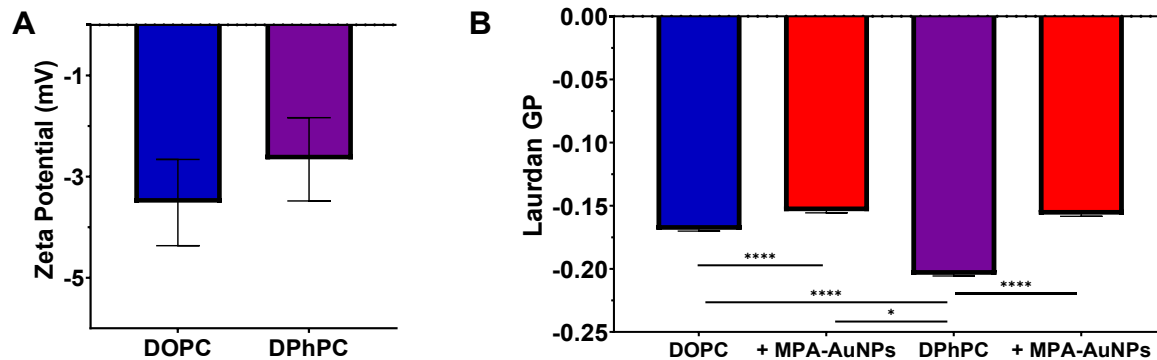


**Figure 4.** Lipid type dictates the impact of MPA-AuNPs (5 nM) on lipid packing. (A)  $\zeta$ -potentials and (B) Laurdan GP values for DOPC and DPhPC vesicles in high (0.15 M KCl), with addition of 5 nM MPA-AuNPs. Statistical significance is denoted by asterisks:  $P < 0.05$  (\*),  $P < 0.01$  (\*\*),  $P < 0.001$  (\*\*\*),  $P < 0.0001$  (\*\*\*\*).

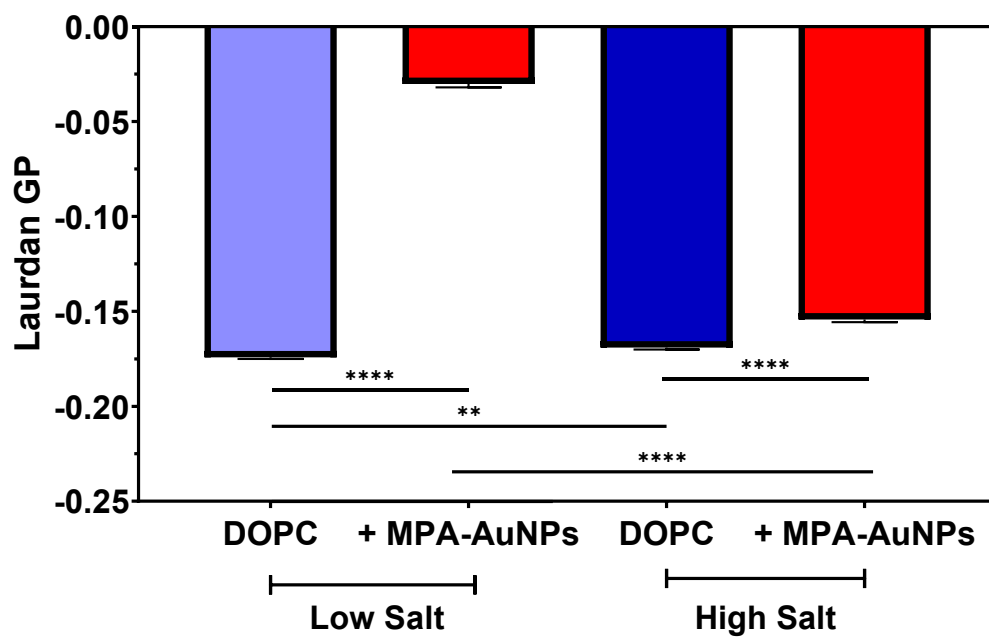


**Figure 5.** Ionic strength influences the impact of MPA-AuNPs on lipid packing rigidity in DOPC vesicles. (A)  $\zeta$ -potentials and (B) Laurdan GP values for DOPC vesicles placed in high (0.15 M KCl) or low (1 mM KCl) salt, with addition of 5 nM MPA-AuNPs. Statistical significance is denoted by asterisks:  $P < 0.05$  (\*),  $P < 0.01$  (\*\*),  $P < 0.001$  (\*\*\*),  $P < 0.0001$  (\*\*\*\*).

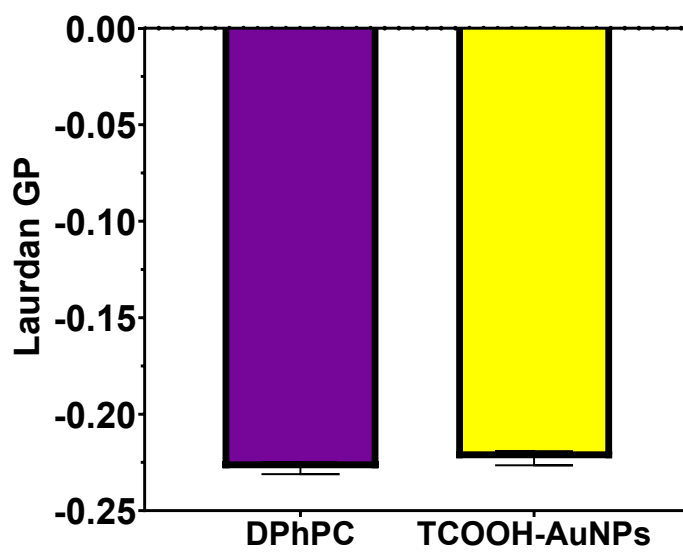


**Figure 6.** TCOOH-AuNPs (5 nM) do not alter Laurdan GP for DPhPC vesicles in high salt (0.15 M KCl).

## 4.6 References

- (1) Phillips, R.; Ursell, T.; Wiggins, P.; Sens, P. Emerging Roles for Lipids in Shaping Membrane-Protein Function. *Nature* **2009**, *459* (7245), 379–385. <https://doi.org/10.1038/nature08147>.
- (2) Jensen, M.; Mouritsen, O. G. Lipids Do Influence Protein Function - The Hydrophobic Matching Hypothesis Revisited. *Biochim. Biophys. Acta - Biomembr.* **2004**, *1666* (1–2), 205–226. <https://doi.org/10.1016/j.bbamem.2004.06.009>.
- (3) Lundbaek, J. A.; Collingwood, S. A.; Ingolfsson, H. I.; Kapoor, R.; Andersen, O. S. Lipid Bilayer Regulation of Membrane Protein Function: Gramicidin Channels as Molecular Force Probes. *J. R. Soc. Interface* **2010**, *7* (44), 373–395. <https://doi.org/10.1098/rsif.2009.0443>.
- (4) Lundbæk, J. A.; Birn, P.; Hansen, A. J.; Søgaard, R.; Nielsen, C.; Girshman, J.; Bruno, M. J.; Tape, S. E.; Egebjerg, J.; Greathouse, D. V.; Mattice, G. L.; Koeppe, R. E.; Andersen, O. S. Regulation of Sodium Channel Function by Bilayer Elasticity. *J. Gen. Physiol.* **2004**, *123* (5), 599–621. <https://doi.org/10.1085/jgp.200308996>.
- (5) Lundbæk, J. A.; Andersen, O. S. Spring Constants for Channel-Induced Lipid Bilayer Deformations: Estimates Using Gramicidin Channels. *Biophys. J.* **1999**, *76* (2), 889–895. [https://doi.org/10.1016/S0006-3495\(99\)77252-8](https://doi.org/10.1016/S0006-3495(99)77252-8).
- (6) Rawicz, W.; Olbrich, K. C.; McIntosh, T.; Needham, D.; Evans, E. Effect of Chain Length and Unsaturation on Elasticity of Lipid Bilayers. *Biophys. J.* **2000**, *79* (October 1999), 328–339.
- (7) Niemelä, P. S.; Hyvönen, M. T.; Vattulainen, I. Influence of Chain Length and Unsaturation on Sphingomyelin Bilayers. *Biophys. J.* **2006**, *90* (3), 851–863. <https://doi.org/10.1529/biophysj.105.067371>.
- (8) Zhang, X.; Barraza, K. M.; Beauchamp, J. L. Cholesterol Provides Nonsacrificial Protection of Membrane Lipids from Chemical Damage at Air–Water Interface. *Proc. Natl. Acad. Sci. U. S. A.* **2018**, *115* (13), 3255–3260. <https://doi.org/10.1073/pnas.1722323115>.
- (9) Jay, A. G.; Hamilton, J. A. Disorder Amidst Membrane Order: Standardizing Laurdan Generalized Polarization and Membrane Fluidity Terms. *J. Fluoresc.* **2017**, *27* (1), 243–249. <https://doi.org/10.1007/s10895-016-1951-8>.
- (10) Filippov, A.; Orädd, G.; Lindblom, G. Influence of Cholesterol and Water Content on Phospholipid Lateral Diffusion in Bilayers. *Langmuir* **2003**, *19* (16), 6397–6400. <https://doi.org/10.1021/la034222x>.
- (11) Redondo-Morata, L.; Giannotti, M. I.; Sanz, F. Structural Impact of Cations on Lipid Bilayer Models: Nanomechanical Properties by AFM-Force Spectroscopy. *Mol. Membr. Biol.* **2014**, *31* (1), 17–28. <https://doi.org/10.3109/09687688.2013.868940>.
- (12) Petrache, H. I.; Zemb, T.; Belloni, L.; Parsegian, V. A. Salt Screening and Specific Ion Adsorption Determine Neutral-Lipid Membrane Interactions. *Proc. Natl. Acad. Sci. U. S. A.* **2006**, *103* (21), 7982–7987. <https://doi.org/10.1073/pnas.0509967103>.

- (13) Elson, E. L.; Fried, E.; Dolbow, J. E.; Genin, G. M. Phase Separation in Biological Membranes: Integration of Theory and Experiment. *Annu. Rev. Biophys.* **2010**, *39*, 207–226. <https://doi.org/10.1146/annurev.biophys.093008.131238.Phase>.
- (14) Shinoda, W. Permeability across Lipid Membranes. *Biochim. Biophys. Acta - Biomembr.* **2016**, *1858* (10), 2254–2265. <https://doi.org/10.1016/j.bbamem.2016.03.032>.
- (15) Foreman-Ortiz, I. U.; Liang, D.; Laudadio, E. D.; Calderin, J. D.; Wu, M.; Keshri, P.; Zhang, X.; Schwartz, M. P.; Hamers, R. J.; Rotello, V. M.; Murphy, C. J.; Cui, Q.; Pedersen, J. A. Anionic Nanoparticle-Induced Perturbation to Phospholipid Membranes Affects Ion Channel Function. *Proc. Natl. Acad. Sci. U. S. A.* **2020**, *117* (45), 27854–27861. <https://doi.org/10.1073/pnas.2004736117>.
- (16) Wang, B.; Zhang, L.; Sung, C. B.; Granick, S. Nanoparticle-Induced Surface Reconstruction of Phospholipid Membranes. *Proc. Natl. Acad. Sci. U. S. A.* **2008**, *105* (47), 18171–18175. <https://doi.org/10.1073/pnas.0807296105>.
- (17) Sanchez, S. A.; Tricerri, M. A.; Gunther, G.; Gratton, E. Laurdan Generalized Polarization: From Cuvette to Microscope. *Mod. Res. Educ. Top. Microsc.* **2007**, *2*, 1007–1014.
- (18) Sanchez, S. A.; Tricerri, M. A.; Gratton, E. Laurdan Generalized Polarization Fluctuations Measures Membrane Packing Micro-Heterogeneity in Vivo. *Proc. Natl. Acad. Sci.* **2012**, *109* (19), 7314–7319. <https://doi.org/10.1073/pnas.1118288109>.
- (19) Bagatolli, L. A.; Parasassi, T.; Fidelio, G. D.; Gratton, E. A Model for the Interaction of 6-Lauroyl-2-(N,N-Dimethylamino)Naphthalene with Lipid Environments: Implications for Spectral Properties. *Photochem. Photobiol.* **1999**, *70* (4), 557. [https://doi.org/10.1562/0031-8655\(1999\)070<0557:amftio>2.3.co;2](https://doi.org/10.1562/0031-8655(1999)070<0557:amftio>2.3.co;2).
- (20) Parasassi, T.; Gratton, E. Membrane Lipid Domains and Dynamics as Detected by Laurdan Fluorescence. *J. Fluoresc.* **1995**, *5* (1), 59–69. <https://doi.org/10.1007/BF00718783>.
- (21) Garda, H. A.; Bernasconi, A. M.; Brenner, R. R.; Aguilar, F.; Soto, M. A.; Sotomayor, C. P. Effect of Polyunsaturated Fatty Acid Deficiency on Dipole Relaxation in the Membrane Interface of Rat Liver Microsomes. *Biochim. Biophys. Acta - Biomembr.* **1997**, *1323* (1), 97–104. [https://doi.org/10.1016/S0005-2736\(96\)00180-0](https://doi.org/10.1016/S0005-2736(96)00180-0).
- (22) Harris, F. M.; Best, K. B.; Bell, J. D. Use of Laurdan Fluorescence Intensity and Polarization to Distinguish between Changes in Membrane Fluidity and Phospholipid Order. *Biochim. Biophys. Acta - Biomembr.* **2002**, *1565* (1), 123–128. [https://doi.org/10.1016/S0005-2736\(02\)00514-X](https://doi.org/10.1016/S0005-2736(02)00514-X).
- (23) Gratton, E.; Digman, M. A. Laurdan Identifies Different Lipid Membranes in Eukaryotic Cells. In *Cell Membrane Nanodomains: From Biochemistry to Nanoscopy*; 2014; pp 283–304. <https://doi.org/10.1201/b17634>.
- (24) Watanabe, N.; Goto, Y.; Suga, K.; Nyholm, T. K. M.; Slotte, J. P.; Umakoshi, H. Solvatochromic Modeling of Laurdan for Multiple Polarity Analysis of Dihydrospingomyelin Bilayer. *Biophys. J.* **2019**, *116* (5), 874–883. <https://doi.org/10.1016/j.bpj.2019.01.030>.
- (25) Startek, J. B.; Talavera, K.; Voets, T.; Alpizar, Y. A. Differential Interactions of Bacterial

- Lipopolysaccharides with Lipid Membranes: Implications for TRPA1-Mediated Chemosensation. *Sci. Rep.* **2018**, *8* (1), 1–11. <https://doi.org/10.1038/s41598-018-30534-2>.
- (26) Ramani, K.; Balasubramanian, S. V. Fluorescence Properties of Laurdan in Cochleate Phases. *Biochim. Biophys. Acta - Biomembr.* **2003**, *1618* (1), 67–78. <https://doi.org/10.1016/j.bbamem.2003.10.009>.
- (27) Golfetto, O.; Hinde, E.; Gratton, E. Laurdan Fluorescence Lifetime Discriminates Cholesterol Content from Changes in Fluidity in Living Cell Membranes. *Biophys. J.* **2013**, *104* (6), 1238–1247. <https://doi.org/10.1016/j.bpj.2012.12.057>.
- (28) Bhat, A.; Edwards, L. W.; Fu, X.; Badman, D. L.; Huo, S.; Jin, A. J.; Lu, Q. Effects of Gold Nanoparticles on Lipid Packing and Membrane Pore Formation. *Appl. Phys. Lett.* **2016**, *109* (26). <https://doi.org/10.1063/1.4972868>.
- (29) Bozich, J. S.; Lohse, S. E.; Torelli, M. D.; Murphy, C. J.; Hamers, R. J.; Klaper, R. D. Surface Chemistry, Charge and Ligand Type Impact the Toxicity of Gold Nanoparticles to *Daphnia Magna*. *Environ. Sci. Nano* **2014**, *1* (3), 260–270. <https://doi.org/10.1039/C4EN00006D>.
- (30) Lohse, S. E.; Eller, J. R.; Sivapalan, S. T.; Plews, M. R.; Murphy, C. J. A Simple Millifluidic Benchtop Reactor System for the High-Throughput Synthesis and Functionalization of Gold Nanoparticles with Different Sizes and Shapes. *ACS Nano* **2013**, *7* (5), 4135–4150. <https://doi.org/10.1021/nm4005022>.
- (31) Mayer, L. D.; Hope, M. J.; Cullis, P. R. Vesicles of Variable Sizes Produced by a Rapid Extrusion Procedure. *BBA - Biomembr.* **1986**, *858* (1), 161–168. [https://doi.org/10.1016/0005-2736\(86\)90302-0](https://doi.org/10.1016/0005-2736(86)90302-0).
- (32) Balleza, D.; Garcia-Arribas, A. B.; Sot, J.; Ruiz-Mirazo, K.; Goñi, F. M. Ether- Versus Ester-Linked Phospholipid Bilayers Containing Either Linear or Branched Apolar Chains. *Biophys. J.* **2014**, *107* (6), 1364–1374. <https://doi.org/10.1016/j.bpj.2014.07.036>.
- (33) Polak, A.; Tarek, M.; Tomšič, M.; Valant, J.; Poklar Ulrih, N.; Jamnik, A.; Kramar, P.; Miklavčič, D. Structural Properties of Archaeal Lipid Bilayers: Small-Angle X-Ray Scattering and Molecular Dynamics Simulation Study. *Langmuir* **2014**, *30* (28), 8308–8315. <https://doi.org/10.1021/la5014208>.
- (34) El-Beyrouthy, J.; Makhoul-Mansour, M. M.; Taylor, G.; Sarles, S. A.; Freeman, E. C. A New Approach for Investigating the Response of Lipid Membranes to Electrocompression by Coupling Droplet Mechanics and Membrane Biophysics. *J. R. Soc. Interface* **2019**, *16* (161). <https://doi.org/10.1098/rsif.2019.0652>.
- (35) Kara, S.; Afonin, S.; Babii, O.; Tkachenko, A. N.; Komarov, I. V.; Ulrich, A. S. Diphytanoyl Lipids as Model Systems for Studying Membrane-Active Peptides. *BBA - Biomembr.* **2017**, *1859* (10), 1828–1837. <https://doi.org/10.1016/j.bbamem.2017.06.003>.
- (36) Chen, D.; Santore, M. M. Large Effect of Membrane Tension on the Fluid-Solid Phase Transitions of Two-Component Phosphatidylcholine Vesicles. *Proc. Natl. Acad. Sci. U. S. A.* **2014**, *111* (1), 179–184. <https://doi.org/10.1073/pnas.1314993111>.

(37) Poger, D.; Caron, B.; Mark, A. E. Effect of Methyl-Branched Fatty Acids on the Structure of Lipid Bilayers. *J. Phys. Chem. B* **2014**, *118* (48), 13838–13848. <https://doi.org/10.1021/jp503910r>.

## Chapter 5: Conclusions and Future Directions

The rise of nanomaterials in industrial and consumer applications necessitates the study of their interactions with biological species upon disposal to mitigate potential negative effects. Moreover, characterizing the interaction of nanomaterials with cellular components can provide design rules that improve pharmaceutical or biomedical applications of nanomaterials. Thus, it is important to characterize nano-bio interactions in order to both mitigate potential negative outcomes and to reveal design rules that may improve intentional biological use of nanomaterials. Model lipid bilayer systems are often used in studying nano-bio interactions because they simplify living systems to focus on individual membrane components, revealing mechanistic insight that would otherwise be obscured by the functional complexity of the cell. Here, we demonstrate a model membrane system consisting of phospholipids and an embedded model ion channel (gA). Employing this model membrane system allowed us to study the impact of anionic AuNPs on functional gA ion channels, assess the effect of the presence of gA on AuNP binding, and reveal the mechanism by which AuNPs can exert effects on embedded ion channels.

First, we examined the impact of anionic AuNPs on the function of membrane-embedded gA ion channels and found that the AuNPs decreased the number of channels but increased their duration. Further study by both FTIR spectroscopy and computational modeling indicated that the AuNPs do not bind directly to the ion channels, but instead disrupt channel function through a membrane-mediated mechanism. Computational studies suggested that anionic AuNPs weakly adsorb to zwitterionic phospholipids, altering their headgroup orientation and lipid packing in a way that reduces the energetic penalty for channel formation and resulting in the increased

channel durations observed experimentally. These studies are among the first to experimentally link changes in ion channel function to alterations in membrane mechanical properties.

We employed a similar model membrane system in examining the influence of the presence of gA on the binding of anionic AuNPs. A unique combination of NTA and statistical mixture distributions revealed that the presence of gA increases the frequency and amount of binding to anionic AuNPs. This combination of methods can also be expanded to study particle binding or aggregation in other nano-sized systems and thus has wide potential use in pharmaceutical, biomedical, or biophysics research.

Finally, a dye sensitive to lipid order was used to examine the impact of anionic AuNPs on lipid packing. Anionic MPA AuNPs were found to increase lipid packing, as is consistent with previous ion channel studies suggesting that a local increase in lipid packing ultimately leads to extended membrane softening and a resulting increase in gA channel duration in much larger membrane systems. Lipid packing changes were also found to be sensitive to ionic strength of the solution, lipid type, and anionic AuNP ligand type. These studies corroborate the proposed membrane-mediated and lipid packing-based mechanism for ion channel disruption, although further study is necessary to better characterize the impact of AuNP concentration and ligand type.

Ultimately, the inclusion of embedded ion channels in model membranes allowed the study of a functional component while retaining enough simplicity to reveal the underlying mechanism of disruption by anionic AuNPs. This model system should serve as a starting point for further work. Studies on ion channel function and lipid packing suggested that nanomaterial aggregation and surface charge may play a role in the extent of membrane interaction and subsequent ion channel disruption. Thus, future studies employing nanomaterials with greater

control over aggregation state and surface charge may reveal additional, more detailed information.